Computational Investigation of Chemical Reactions: Exploring the Reactivity of Nickel Enoate and Fumarate Complexes and Radical Assistance in the Force-Enabled Bond Scission of Poly(Acrylic Acid)

by

Michael T. Robo

A dissertation submitted in partial fulfillment
of the requirements for the degree of
Doctor of Philosophy
(Chemistry)
in the University of Michigan
2020

Doctoral Committee:

Professor John Montgomery, Co-Chair
Associate Professor Paul M. Zimmerman, Co-Chair
Professor Brian J. Love
Professor Melanie S. Sanford
Professor John P. Wolfe

Michael T. Robo

mrobo@umich.edu

ORCID iD: 0000-0003-1356-246X

Dedication

To the brave and tireless healthcare workers involved in the ongoing COVID-19 pandemic.

Acknowledgements

First, I would like to thank my parents, Jim Robo and Meredith Trim. They have provided me with unending love and support for the entirety of my existence. My father pushed me early on to intern at The Scripps Research Institute, and later encouraged me to take organic chemistry freshman year of college. My mother has been similarly supportive, and helped me make my move to Ann Arbor. I would also like to thank the many chemistry mentors that I have encountered over the years, as they have guided me to where I am today. Early mentors include my high school chemistry teacher Barbara Murphy, Roy Periana and the Periana lab, as well as Dan Weix, Michael Prinsell, and the rest of the Weix lab. Pursuing a Ph.D. in chemistry can sometimes be a difficult enterprise, and the positive experiences that they provided gave me the strength to pursue my degree to completion.

I've had the pleasure of working with many collaborators over the years. Graduate students who I've worked directly with include Alex Nett, Ellen Butler, Santiago Cañellas, Amie Frank on the air-stable Ni(0) project, and Takunda Chazovachii, Danielle Fagnani, and Jessica Tami with depolymerization. PIs I've worked with include Anne McNeil, Mark Banaszak Holl, and Neil Marsh. The collaborations in the work reported here are enabled in part by the bounty of capable students and PIs eager to collaborate that this department has to offer. Takunda Chazovachii in particular has maintained a strong working relationship with me for a number of years.

The Procter and Gamble company has provided much of my financial support, and Dimitris Collias

has worked with me on the P&G side of the poly(acrylic acid) project. P&G has also gifted me with the opportunity to work there for a summer in 2017. Bruce Murch and Bill Laidig provided me with a life-changing opportunity, and gave me the sense what industrial research is like.

The chemistry department has at the University of Michigan has been amazingly supportive over the past 6 years, and I'm lucky to have the opportunity to work with two wonderful PIs. John Montgomery was originally the sole chair of my committee, and he provided the support and funding I needed for my first two years in the program. He was also more than accommodating when it became clear that I was more suited for computational work. The investment in me from him, Paul, and the department cannot be overstated. Paul Zimmerman, who became co-chair of my committee in 2016, has been an excellent mentor. He has repeatedly amazed me with his deep knowledge of disparate fields, and has been more than happy to provide valuable career advice. Like John, Paul has shown a genuine care for his students, which has fostered in me a deep trust in him. He was also instrumental in directing me towards my 2017 internship at Procter and Gamble, as he recommended me for it based on confidence in me that I did not yet have in myself.

Finally, I would like to thank all of the friends that I've made in Ann Arbor over the years. My coevals Aaron Proctor, Alonso Arguelles, and Grayson Ritch formed a core friend group that stood the test of time. We put the effort in to regularly eat lunch and play games together, and it paid off in the form of deep, lasting friendships. It seems unlikely to me that I'll ever be able to forge similar personal bonds like the ones formed among coevals in grad school. In addition to our group, I've made many other friends, including Jacob Geri, Isaac Roles, Zach O'Keefe, and Cody Aldaz.

My experiences in grad school have been truly wonderful, and I'm forever grateful for the rich social and intellectual life that Ann Arbor and the University of Michigan Department of Chemistry have given me.

Table of Contents

List of Figures

List of Tables

Abstract

Computational chemistry has emerged as a powerful tool in identifying the key chemical states that define the kinetics, thermodynamics, and the various selectivities of a chemical reaction. It allows for a greater understanding of chemical processes by providing insights that would be difficult to achieve through direct experimentation alone. Herein are described three examples where computational analysis is used to provide insight into chemical reactions.

In Chapter 1, some fundamentals of computational research in chemistry is described. Topics include the potential energy surface, the computational methods used for energy calculation, and transition state finding using the growing string method. The tools described in this chapter are used in the subsequent chapters.

Chapter 2 investigates the mechanism of a nickel-catalyzed [3+2] alkylative cycloaddition. Prior experimental work has suggested multiple possible mechanisms, which are interrogated here computationally. Two distinct mechanisms are found to be in a precarious balance with each other, and small perturbations in the substrates used in the reaction are found to tilt the balance towards one mechanism over the other. The findings from this chapter have implications for the mechanism of [3+2] alkylative cycloadditions as a whole, including the activation process detailed in Chapter 3.

In Chapter 3, the activation process of air-stable nickel fumarate catalysts is studied. The original hypothesis of fumarate dissociation as a mechanism of activation was overturned after

computational analysis determined a fumarate consumption event must occur instead. These findings inspired subsequent experimental work that isolated the products of fumarate dissociation, and found that catalyst activation goes through a similar [3+2] alkylative cycloaddition detailed in Chapter 2. Through this lens, the mechanisms of activation of active IMes catalyst and inactive BAC catalyst are evaluated computationally, to provide a rationale for why one catalyst works and the other does not. Using these insights, preliminary investigations towards improving the BAC catalyst are performed.

Chapter 4 details the effect of radical attack on the tensile strength of poly(acrylic acid) (PAA). Two different methods are used to determine how radical attack weakens the tensile strength of the polymer backbone. Additionally, the effect of force in the radical-free and radical-abstracted cases on the geometry of the starting structures and transition state of the species involved in bond scission is observed. The different behaviors between the two regimes are attributed to the differences in the curvature of their potential energy surfaces. The findings of this chapter carry implications for the development of new depolymerization reactions.

Finally, Chapter 5 summarizes the work, and provides final thoughts on future directions. Elements of this work are compared to the Gettier problem, and the symbiotic relationship between theorists and experimentalists is discussed.

Chapter 1: Introduction

1.1 Using Computational Chemistry to Evaluate Chemical Reactions

In considering the development of a new chemical reaction, two conditions must hold true. Firstly, the reaction must be thermodynamically feasible. This condition is satisfied if the entire chemical process is exergonic, which means that the free energy of the final product is lower than the free energy of the starting material. Secondly, the reaction must be kinetically feasible. While any exergonic reaction is guaranteed to happen eventually, a kinetically feasible reaction will occur at a rate that is useful to humans, and will also outcompete other potential pathways. The rate at which a chemical reaction occurs is controlled by the energy of its highest energy state that occurs during the chemical transformation.

To evaluate the kinetics and thermodynamics of a chemical reaction, therefore, all that is needed to be done is to evaluate the energy of a few certain states. The challenge in computational chemistry, then, is identifying the states that are relevant over the course of the reaction, and accurately evaluating them. Fortunately, quantum chemical techniques such as density functional theory (DFT) have emerged as a powerful tool to evaluate the energies of chemical structures.[1] Additionally, recent development of transition-state finding and conformer-generating tools has given computational chemists the ability to identify relevant chemical states at an unprecedented pace.[2]

By leveraging these advancements, computational chemists are now in a position to provide useful predictions, at a pace fast enough to keep up with experimental advancements. Chemical reactions can often be challenging to characterize experimentally, and computational chemistry has the advantage of being able to directly study the putative intermediates of a reaction. This contrasts with the majority of experimental research in reaction development, which often focuses on the inputs and outputs of a reaction, and can sometimes struggle to identify key intermediates.

This work describes a number of cases where computational chemistry is used to explain and predict experimental results. Chapter 2 details the mechanism of a nickel-catalyzed three-component coupling reaction. Previous work on related [3+2] reductive cycloadditions gave conflicting evidence on what the active mechanism of the transformation could be, and the addition of computational analysis provides clarity to the murky experimental picture. In Chapter 3, the activation sequence of air-stable nickel(0) catalysts are examined. This chapter showcases the ability of computational chemistry to provide useful predictions for the experimentalist, and uses the knowledge gained from Chapter 2 as a framework for understanding catalyst activation. And finally, in Chapter 4, the effects of hydrogen atom abstraction in the mechanochemical degradation of poly(acrylic acid) are explored. Here, recently developed tools for transition state finding under force are used, which allow for analysis of the differences in structure between bond scission under force in the presence and absence of a radical on the polymer backbone.

The remainder of this chapter will provide a useful background for understanding the computational analysis of chemical reactions. Topics to discuss include: defining the potential energy surface, identifying and utilizing the key chemical states necessary to describe the thermodynamics and kinetics of a reaction, computational methods to evaluate chemical states, and modern transition state finding methods.

1.2 The Potential Energy Surface

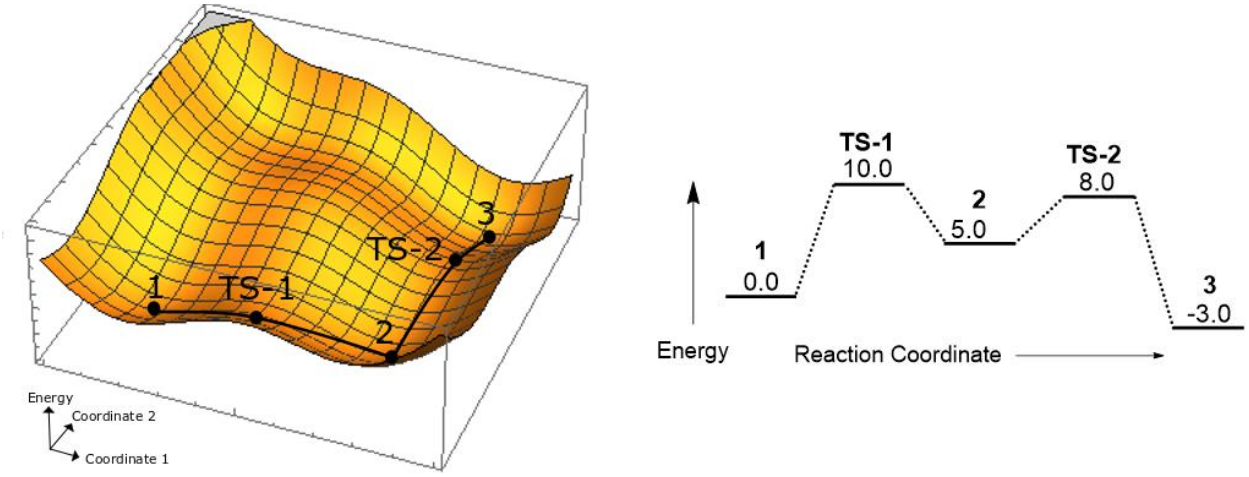

Figure 1-1. *(Left) A 3-dimensional potential energy surface. (Right) The same PES, represented using a single reaction coordinate. The energies of the individual states are listed on the right-hand side.*

For a given chemical system, there exists a multitude of possible arrangements of the atoms involved in the system. If we imagine all of the arrangements, we can construct a hypersurface existing in approximately 3N dimensions, with N being the number of atoms in the system. This hypersurface is generally referred to as the "potential energy surface" (PES), and its contours are what determines the mechanisms of chemical transformations. A simplified multi-dimensional representation of such a surface is given on the left-hand side of Figure 1-1. In Figure 1-1, points **1**, **2**, and **3** are local minima on the surface, and which means they also represent chemical intermediates. Intermediate **1** is capable of transitioning to **2** through the path containing **TS-1**, and intermediate **2** can then transform into **3** through the path containing **TS-2**. Points **TS-1** and **TS-2** are notable, as they are at saddle-points on the PES. The technical definition of a saddle point is a point where the gradient equals zero, but is neither a local maximum or minimum. In the context of analyzing the PES of a chemical system, saddle points are the highest energy point in the lowest energy path between two local minima. The most probable path between two

intermediates will go through the saddle point, which in chemical terms is referred to as a transition state, abbreviated as "TS" in this text.

While the PES provides a complete description of all possible atomic arrangements for a given system, in practice, it is more useful to pictorially describe the PES along a single axis, as represented on the right-hand side of Figure 1-1. This representation makes it easier to see the energies of the different states involves, and simplifies the interpretation of the PES. By focusing only on the critical states (intermediates and transition states), we can more easily determine the kinetics and thermodynamics of a given chemical reaction.

1.3 Using the Critical States of the PES to Derive Reaction Thermodynamics and Kinetics

Determining the thermodynamics of a chemical reaction is a straightforward exercise. In looking at the equilibrium between two states, the equilibrium constant is given by equation 1 (Figure 1-2). Notably, as the difference in free energy (ΔG) grows larger, the equilibrium constant (K_{eq}) changes at an exponential rate. In looking a unimolecular transformation, where species A transforms into species B, the equilibrium constant is the expected ratio between the two states. Using the relationship in equation 1, we can evaluate the thermodynamics of an entire chemical reaction using equation 2 (Figure 1-2), where multiple reactants (R_1, R_2,…) are converted into multiple products (P_1, P_2, …). Based off of equation 2, we can see that when a reaction is exergonic ($\Delta G < 0$), K_{eq} becomes larger than 1, indicating that if the reaction mixture were allowed to equilibrate, the majority of the material would transform into the set of products. Additionally, given the exponential nature of the equilibrium constant, a ΔG value of merely -10 kcal/mol would be expected to equilibrate until the ratio of products to reactants exceeds 1,000,000 to 1.

Equation 1

$$K_{eq} = e^{\frac{-\Delta G_{AB}}{RT}} = \frac{[B]}{[A]}$$

$$A \underset{}{\overset{\Delta G_{AB}}{\rightleftharpoons}} B$$

Equation 2

$$K_{eq} = e^{\frac{-\Delta G_{rxn}}{RT}} = \frac{[P_1] * [P_2] * \cdots}{[R_1] * [R_2] * \cdots}$$

$$R_1 + R_2 + \cdots \xrightarrow{\Delta G_{rxn}} P_1 + P_2 + \cdots$$

Figure 1-2. *Equilibrium constants (1) between states A and B and (2) for a chemical reaction. Where: K_{eq} is the equilibrium constant, ΔG is the change in free energy, R is the gas constant, and T is the absolute temperature of the reaction.*

While evaluating the thermodynamics a reaction requires the analysis of only the start and end states, the kinetics of reaction is more difficult to compute. The rate at which a chemical reaction progresses is given by the Eyring equation, shown in Figure 1-3. Under transition-state theory, the transition state is considered to be in quasi-equilibrium with the reactants. Thus, as the Eyring equation is based off of the equations for thermodynamic equilibrium, it shares many similar features. In particular, under the Eyring equation, the difference in free energy between the reactant and the transition state ($\Delta G^{\ddagger}$) affects the rate at which the reaction can happen. As $\Delta G^{\ddagger}$ increases, the rate of transformation decreases exponentially.

Eyring Equation

$$k_{rxn} = \frac{\kappa k_b T}{h} e^{\frac{-\Delta G^{\ddagger}}{RT}}$$

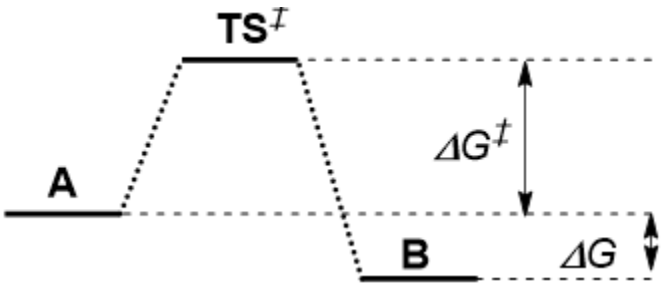

Figure 1-3. *The Eyring equation gives the rate of a chemical reaction, such as the transformation of A to B. Where: k_{rxn} is the rate of the reaction, κ is the transmission coefficient, k_b is Boltzmann's constant, T is the absolute temperature of the system, h is Planck's constant, and R is the gas constant. κ is traditionally considered to be set to 1.*

However, a typical chemical reaction tends to involve multiple intermediates, with multiple transition states where one intermediate transforms into another. In the multistep case, the time

that it takes for a unit of reactant to transform into a unit of product would be expected to be a combination of the total time that it takes for all steps in the reaction to occur.[3] However, this picture can be greatly simplified by taking advantage of the exponential nature of the Eyring equation. At room temperature, for every additional 1 kcal/mol increase in $\Delta G^{\ddagger}$, the corresponding reaction takes about 5.4 times longer to occur. Thus, the largest overall $\Delta G^{\ddagger}$ ends up accounting for the vast majority of the time needed for a chemical transformation to happen.[3]

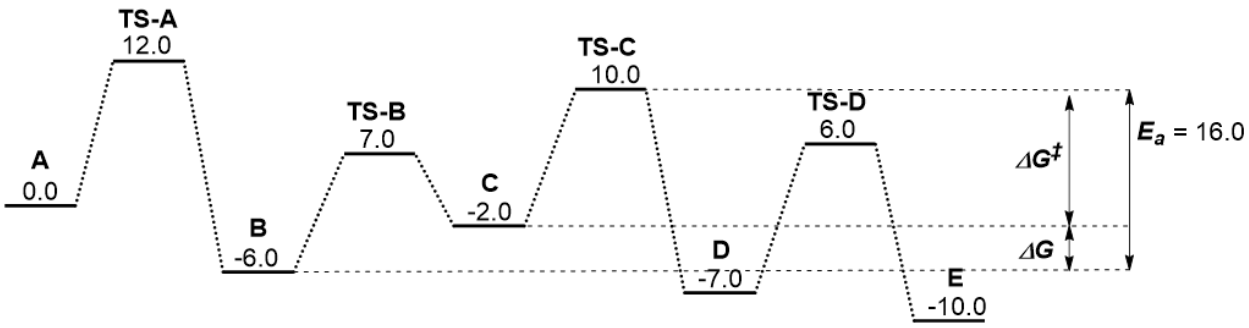

$$k_{rxn} = e^{\frac{-\Delta G}{RT}} * A e^{\frac{-\Delta G^{\ddagger}}{RT}} = A e^{\frac{-E_a}{RT}}$$

$$A = \frac{\kappa k_b T}{h} \qquad E_a = \Delta G + \Delta G^{\ddagger}$$

Figure 1-4. *A potential energy surface for the transformation of A to E. The largest barrier process involves* ***B*** *transforming into* ***D*** *via* ***TS-C****.*

Searching for the largest overall barrier is not a simple case of evaluating the energy of a transition state relative to its prior intermediate. For instance, in Figure 1-4, in the transformation of **A** to **E**, the largest barrier for the reaction is 16.0 units, measured between intermediate **B** and transition state **TS-C**. The overall barrier is calculated to be 16.0 units as intermediate **C** is higher in energy than **B**. That means, thermodynamically, only a small fraction of **B** will convert to **C**, and then, of that small fraction, some of that material will convert to **D** through transition state **TS-C**. By measuring the barrier from **B** to **TS-C**, we take into account the fact that conversion to **C** is a thermodynamically unfavorable process. And as the Eyring equation is derived from the equations

in Figure 1-2, we can simply add the difference in energy between **B** and **C** to the barrier from **C** to **TS-C** to derive an overall barrier for the transformation.[3]

A similar analysis can be performed on catalytic reactions.[4–6] But, since catalytic reactions are by nature cyclical, it's possible that the catalytic cycle can initially form a very stable complex, and then subsequently fail to "turn over". The largest barrier can be found by looking at two contiguous catalytic cycles, with the second cycle offset by the difference in energy between the reactants and the products. With the new potential energy surface in hand, searching for the highest barrier can proceed as normal. An example of this process is shown in Figure 1-5. In this example, the highest barrier process involves intermediate **B** turning over the catalyst via **TS-A'**. Without considering a second catalytic cycle, it would appear that the highest barrier process would be intermediate **A** transforming into intermediate **B**, leading to an erroneous lower barrier, and a mistaken belief about which states in the catalytic cycle have the greatest effect on catalyst turnover.

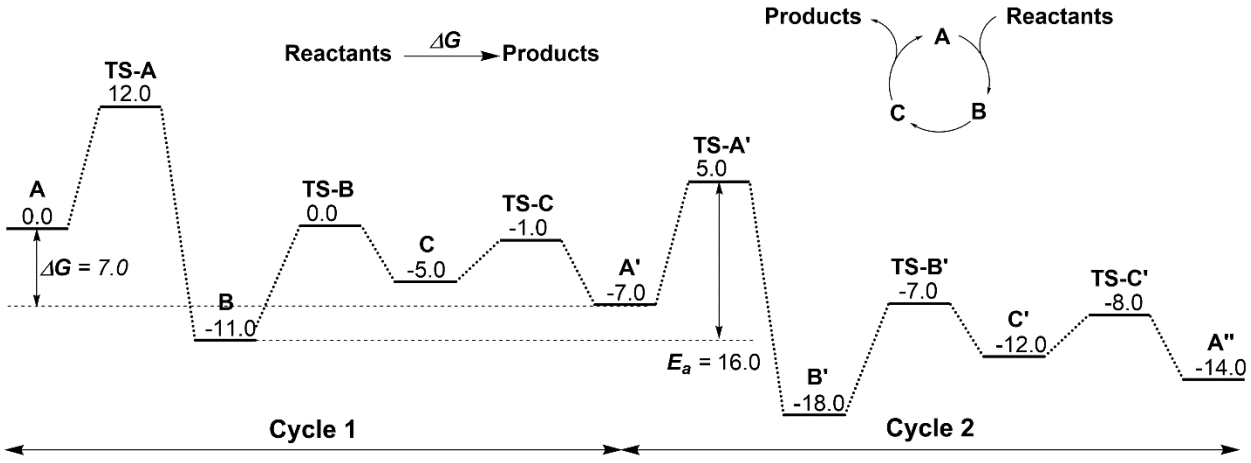

Figure 1-5. *An example catalytic transformation of reactants to products. Two cycles of the process are shown, with the intermediates of the second cycle denoted with an apostrophe.*

1.4 The Computational Evaluation of Chemical States

Energy evaluation is a necessary component in the construction of a potential energy surface. The main method used in this work is density functional theory (DFT). DFT is considered to have been developed in 1964,[1] when Hohenberg and Kohn proved that kinetic and potential energies of any N-electron system can be described by a function of electron density (a so-called "density functional"), implying that one could perfectly predict the properties of a system, if a perfect density functional was in hand.[7] The following year, Kohn and Sham demonstrated that a density functional that treats all of the electrons as non-interacting accounts for the bulk of the total energy, meaning that only the small effect of electron interaction, termed the "exchange-correlation energy" needs to be determined to obtain an exact result.[8]

By avoiding the direct computation of electron-electron interactions, DFT scales at a relatively low cost (N^3, where N is the number of electrons), which compares favorably with wavefunction based methods ($N^{4\text{-}10}$).[9] While in principle, DFT can deliver perfect accuracy with a perfect functional that describes the exchange-correlation energy, in practice, no such functional exists, and the exchange-correlation energy is approximated. The approaches towards approximating the exchange-correlation energy are diverse and numerous, and this had led to the development of a large menagerie DFT functionals, with differing accuracies and computational costs.[10] In this work the ωB97X-D3[11] functional is used in Chapters 2 and 3, and the B3LYP[12] functional is used in Chapter 4. While the errors calculated DFT functionals are dependent on the benchmarking set used, they provide a useful sense of the accuracy of the functional. In interpreting the computational results of this work, an error of approximately 2 kcal/mol for ωB97X-D3, and approximately 5 kcal/mol for B3LYP, should be considered.[13]

Another consideration in the accuracy of DFT is the choice of basis set for the calculation. While a DFT functional ultimately defines the density of electrons a given chemical system, the basis set describes the orbitals within which the electrons reside. The choice of which orbitals to define, and how to define them, is another factor that can influence the cost and accuracy of a calculation. In general, "double zeta" basis sets (where two functions are used to describe each atomic orbital) are used for processes such as geometry optimization or transition-state finding, where many iterative energy and gradient calculations are performed, and the more computationally expensive "triple zeta" basis sets (three functions per atomic orbital) are used for accurate energy calculations on an optimized structure.[14]

Ab initio methods such as DFT only require the choice of basis set, functional, and the cartesian coordinates for the atoms in the chemical system to be studied. Their simplicity makes them well suited to investigate structures where features such as bond lengths, angles, and torsions are ambiguous, such as in most transition states or metal complexes. However, arriving at those features from first principles is computationally taxing, and in our hands, DFT calculations on systems larger than 200 atoms are too slow to be of use. In molecular mechanics (MM), the parameters that can define features such as bond lengths, angles, and torsions are determined beforehand, often fit to quantum chemical calculations. Using these parameters to calculate the energy of the system results in a speed up of multiple orders of magnitude. In general, molecular mechanics is attractive for lager systems, and is often used to simulate proteins or molecules in the condensed phase.[15]

As molecular mechanics is a good choice for the simulation of large condensed phases, and quantum methods such as DFT is a good choice for the simulation of transition states, a method that uses both quantum and molecular mechanical techniques may be best suited for the study of

transition states within a large system. In QM/MM, a portion of a chemical system is treated using a quantum method such as DFT, MP2, or semi-empirical methods, and the remainder of the system is treated using molecular mechanics.[16] In Chapter 4 of this work, a QM/MM system is used with CHARMM27[17,18] molecular mechanics parameters, in conjunction with DFT using the B3LYP functional with the 6-31G* basis, using an electronic embedding system.[19]

1.5 Identifying Transition States Using the Growing-String Method

While the structure of chemical intermediates only requires following the analytic first derivative to find a local minimum,[20] transition state finding is more difficult, as it is neither a local maximum or minimum on the PES, so a strategy of only following the gradient cannot be used. Fortunately, a number of tools have been developed for transition state searching. These include the linear synchronous transit method,[21] the nudged elastic band method,[22,23] and many others. In the Zimmerman group, a growing string method (GSM) using an internal coordinate system has been developed,[24–26] and is the method of choice in this work for the purposes of identifying transition states. The chief advantages of using GSM is that it allows for the user to be ignorant of the potential structure of the transition state, and, in the case of single-ended GSM, also be ignorant of the potential structure of the product.

The process for single-ended GSM[26] is detailed in Figure 1-6. In the example reaction, the S_N2 addition of thiolate to methyl bromide, the user defines the bonds that they would like to add and break (Top Left). The add and break moves are then interpreted to define the R-P (reactant-product) tangent, a vector on the potential energy surface that dictates the general direction to find a transition state (Top Right). In the direction of the R-P tangent, a new structure (referred to as a node) can be generated (Figure 1-6, 1). This node can then be optimized in all directions except along the R-P tangent (2). From the optimized node, a second node can be generated along the

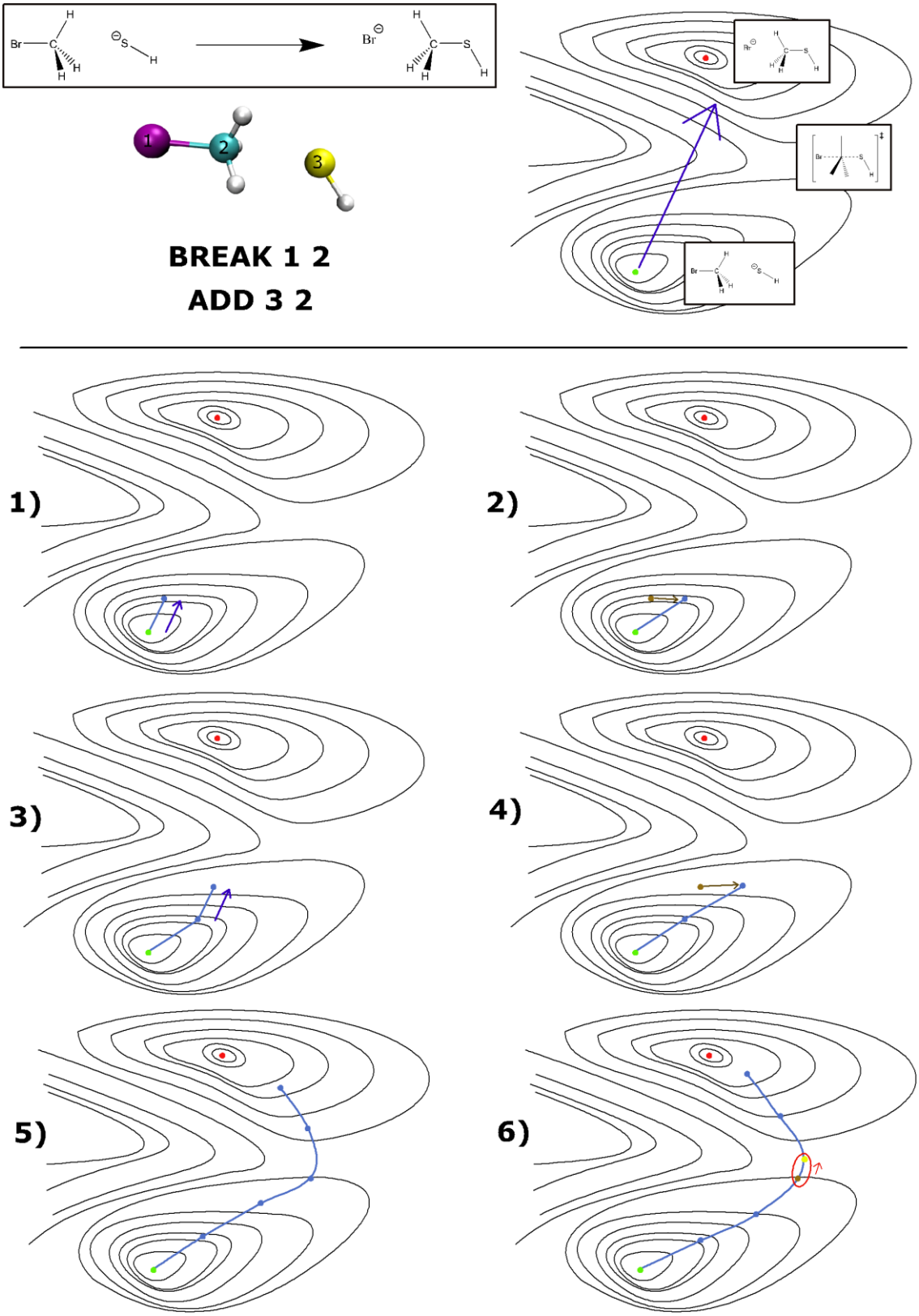

Figure 1-6. *The process of finding a transition state using the single-ended growing string method.*

R-P tangent (3), and then optimized again (4), creating a string of nodes. This process can be repeated, until the nodes begin to decrease in energy, indicating that a saddle point has been crossed (5). Finally, to identify the transition state, the nodes along the growing string are optimized again, and then the highest-energy node is optimized to a transition state using a climbing image search (6).[25]

1.6 Outlook

Despite rough complexity and high dimensionality of the PES, a reaction can be evaluated using only a handful of points on the hypersurface. The thermodynamics of the entire process can be determined by comparing the free energy of all of the reactants compared to all of the products. The kinetics of a reaction can be determined by the observing the largest possible climb in energy between an intermediate and a transition state that occurs in the reaction. Even though in theory, the energetics of only four states need to be evaluated to have an understanding of the kinetics and thermodynamics of a reaction, in practice, more states are typically evaluated, if only to be certain that those processes are possible. These techniques and concepts will be used in the coming chapters to evaluate the chemical process of a three-component coupling reaction, the activation sequence of an air-stable nickel(0) catalyst, and the depolymerization of poly(acrylic acid)

Chapter 2: Computational Investigation of a Nickel-Catalyzed Three-Component Coupling Reaction

The content in this chapter has been published in the *Journal of Organic Chemistry*.[27]

2.1 Background

Five-membered carbocycles are a common structural motif in biology, which has resulted in the development of a rich body of literature on their synthesis.[28–33] Within that body of research, countless strategies for 5-membered ring formation have been developed, including the Nazarov cyclization,[32] ring-expansion reactions,[34] ring-closing metathesis,[35] radical cyclizations,[36] intramolecular nucleophilic attack,[33] cross-couplings,[37] or cycloisomerization reactions.[33] In addition to these listed methods, cycloaddition reactions, in which a ring is formed from multiple separate components, have also been developed. These can include [3+2] cycloadditions, [2+2+1] cycloadditions, and [4+1] cycloadditions.[33]

[3+2] cycloadditions in particular have developed into a powerful synthetic method, due to their potential for chemo-, regio-, diasterio- and enantioselectivity.[28] These transformations can be accomplished through the use of donor-acceptor cyclopropanes,[38] vinyl carbenoid additions,[28] allyl- or allenylsilane additions,[39] or ylide additions.[40] Reductive metal-promoted [3+2] cycloadditions have also represented a viable strategy towards cyclopentane formation. A number of processes have been developed to couple readily available reagents such as alkynes and α,β-unsaturated carbonyl compounds. In such processes, stoichiometric amounts of nickel,[41]

titanium,[42,43] iron,[44,45] or cobalt[46] metallacycles are formed, which can then then collapse into a 5-membered ring after protonation or alkylation (Figure 2-1).

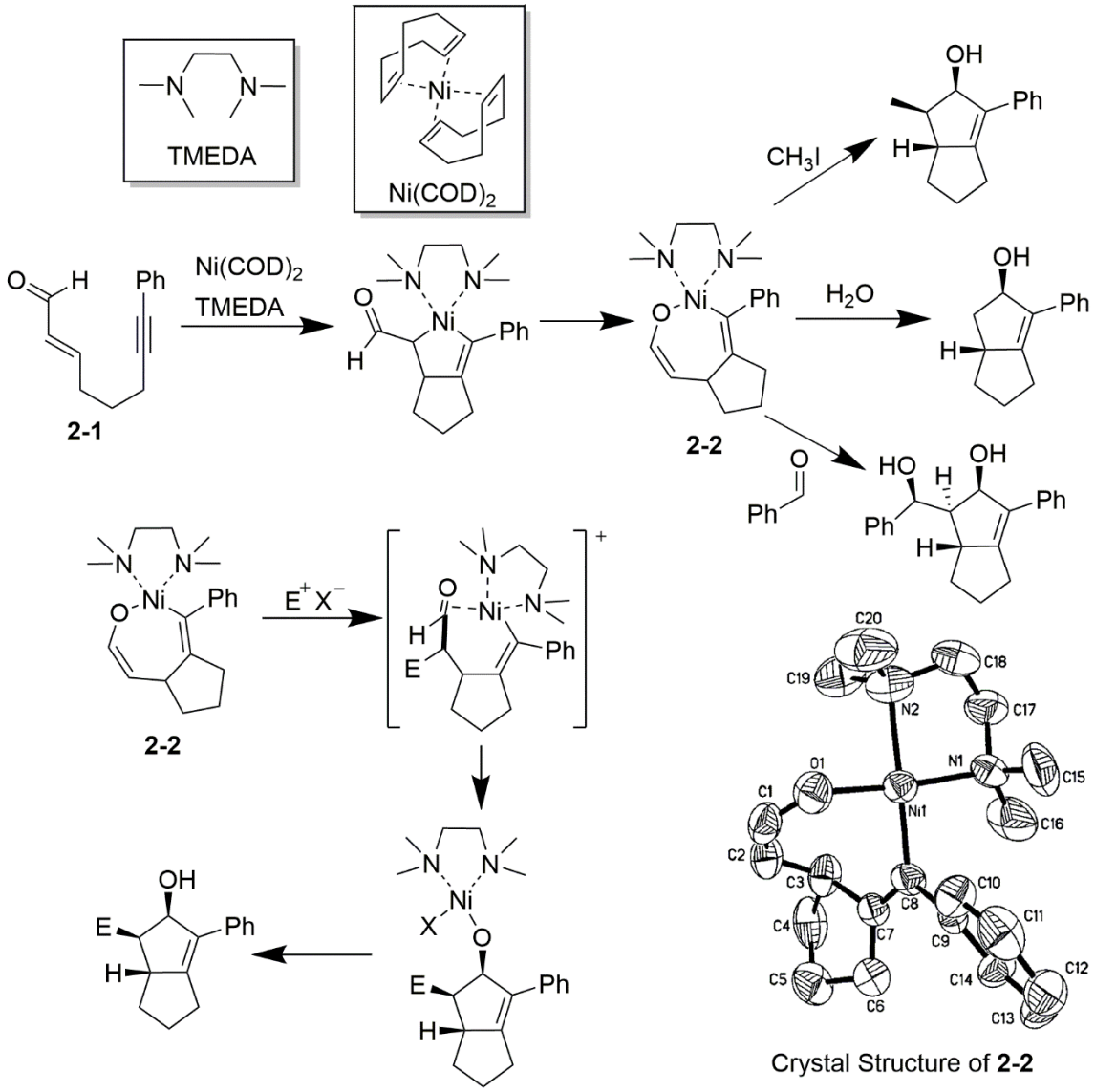

Figure 2-1. *(Top) The Ni-mediated [3+2] cycloaddition of alkynyl enal* ***2-1****. (Bottom Left) Proposed mechanism of cyclization. (Bottom Right) Reported crystal structure of metallacycle* ***2-2****, taken from ref. 49.*

The Montgomery group has a long history of using nickel metallacycles in cycloaddition reactions.[41,47] The group first reported a nickel-mediated [3+2] reductive cyclization in 2000,[48] combining alkynyl enal **2-1** with stochiometric $Ni(COD)_2$ and TMEDA, to create 7-membered metallacycle **2-2**, which can then be quenched with water, methyl iodide, or benzaldehyde to create

a cyclopentenone (Figure 2-1). This transformation was though to occur via initial nucleophilic attack by the enolate moiety in **2-2**, followed by subsequent nucleophilic attack on the resulting aldehyde by the nickel-vinyl species. Metallacycle **2-2** was later directly isolated, and its structure confirmed by X-ray crystallography.[49]

2.2 Mechanistic Ambiguity in the Reductive [3+2] Cycloaddition of Enoates and Alkynes

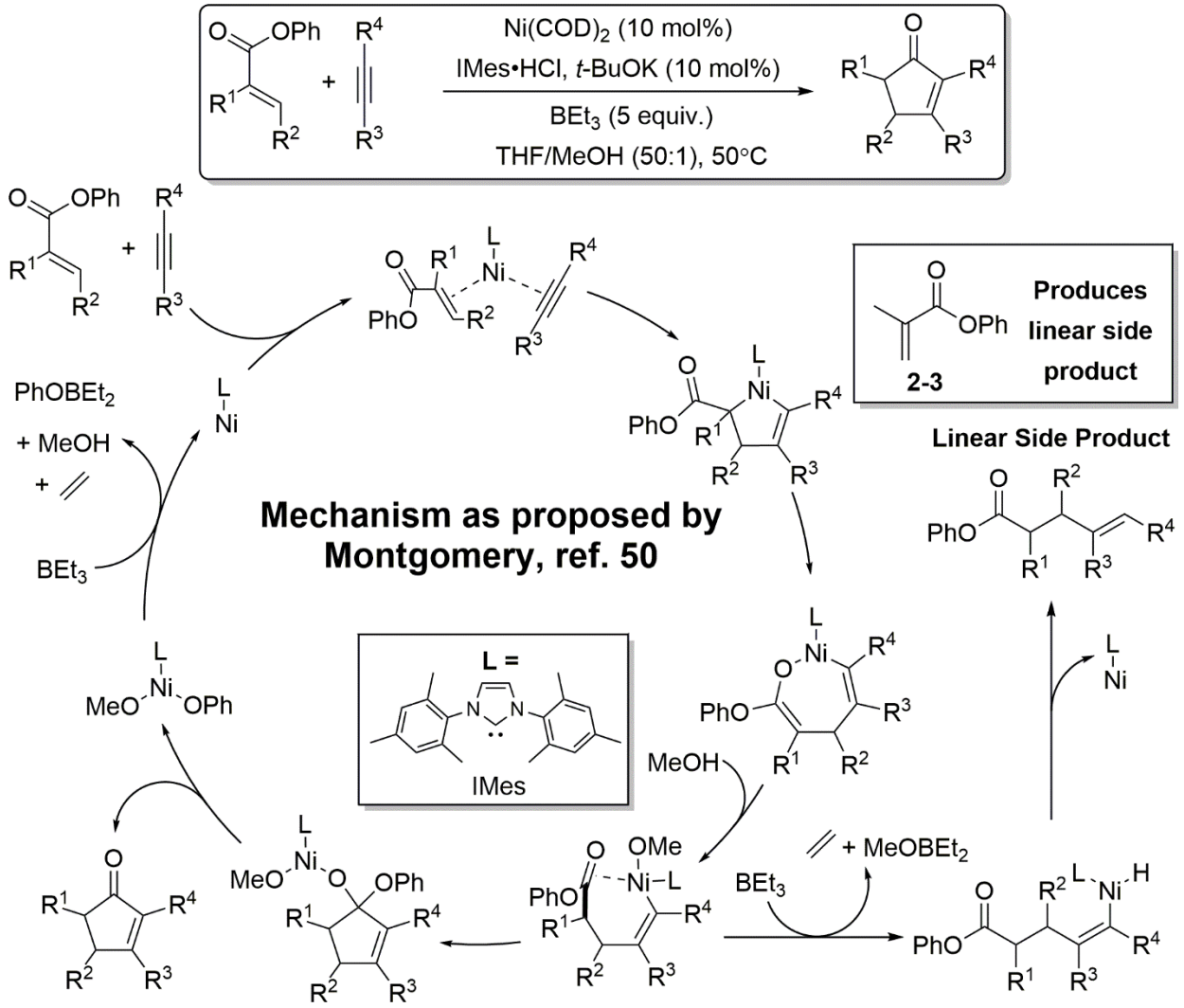

Figure 2-2*. The mechanism of [3+2] cyclization of enoates and alkynes, as proposed by Montgomery (ref. 50). The formation of a linear side product when* ***2-3*** *is used suggests that formation of a 7-membered metallacycle is part of the catalytic cycle.*

The stoichiometric reactions detailed in Figure 2-1 paved the way for methods catalytic in nickel to be developed. In 2011, Montgomery[50] reported catalytic, intramolecular [3+2] cycloaddition reactions of enals with alkynes and of enoates with alkynes. In a separate, concurrent report, Ogoshi[51] also detailed the cycloaddition of enoates and alkynes, using isopropanol as a reductant. Remarkably, even though both reports detail similar transformation, and both use a nickel catalyst with a strong σ-donor ligand, Montgomery and Ogoshi attribute the formation of the [3+2] cycloadduct to separate mechanisms, and both authors provide compelling evidence to support their mechanistic proposals.

In Montgomery's publication, the proposed mechanism of cyclopentenone formation involves the cyclization of the enoate and alkyne, and then subsequent isomerization to a 7-membered metallacycle (Figure 2-2).[50] The resulting metallacycle can be protonated to form a nickel species with a π-bound carbonyl, and then undergo carbocyclization, followed by subsequent alkoxide extrusion to yield the desired cyclopentenone product. Support for this mechanism stems from the observation of linear side products from the attempted cycloadditions of enoate **2-3**, where the ester moiety is kept intact. These observed side products are comparable to previous work[52,53] from the group in which enals and enones are reductively coupled with alkynes to create similar products. Their formation is attributed to the intermediacy of a 7-membered metallacycle, similar to the previously reported **2-2**.

However, in Ogoshi's report, a different mechanistic picture is painted (Figure 2-3).[51] In that report, it was posited that after the enoate and alkyne cyclize, rather than isomerize to a 7-membered metallacycle, the complex instead undergoes phenoxide elimination to form a ketene complex. The ketene complex can then undergo carbocyclization to yield a nickel enolate species that can then be protonated off. Catalyst regeneration occurs via β-hydride elimination of the

resulting nickel-isopropoxide complex. To support this mechanistic proposal, Ogoshi also reports the NMR characterization of the nickel enolate species with an IPr ligand, which is formed quickly from starting materials in the absence of isopropanol, and quickly decays into product once isopropanol is added.

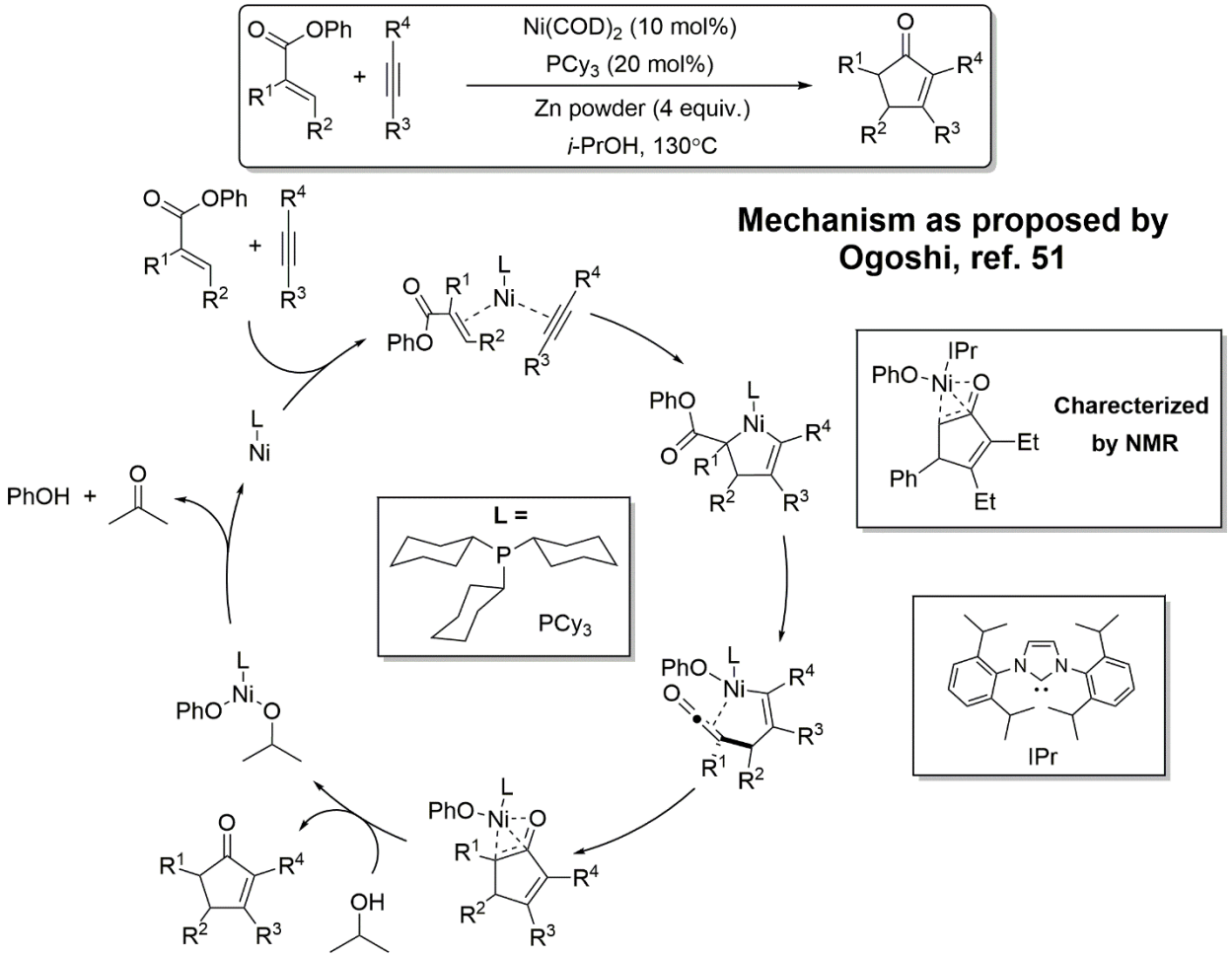

Figure 2-3 *The mechanism of [3+2] cyclization of enoates and alkynes, as proposed by Ogoshi (ref. 51). NMR characterization of a nickel-enolate complex suggests the intermediacy of a ketene-containing species*

2.3 Determining and Evaluating the Possible Mechanisms of the Three-Component Coupling of an Alkyne, Aldehyde, and Enoate

As both Montgomery and Ogoshi provide concrete support for their proposed mechanisms, it seems unlikely that only one mechanism is active in the [3+2] cycloaddition between an enoate

alkyne. Rather, it is more likely that multiple mechanisms are possible, and small changes in the reactant conditions can push the reaction to favor one mechanism over another. However, despite the difference between the two proposed mechanisms, in both cases, catalyst turnover is enabled by the protonation of a nickel enolate species with an alcohol. If the alcohol was removed from the reaction conditions, and replaced by an electrophilic carbon, it could be possible to form an additional carbon-carbon bond in the process (Figure 2-4, top).

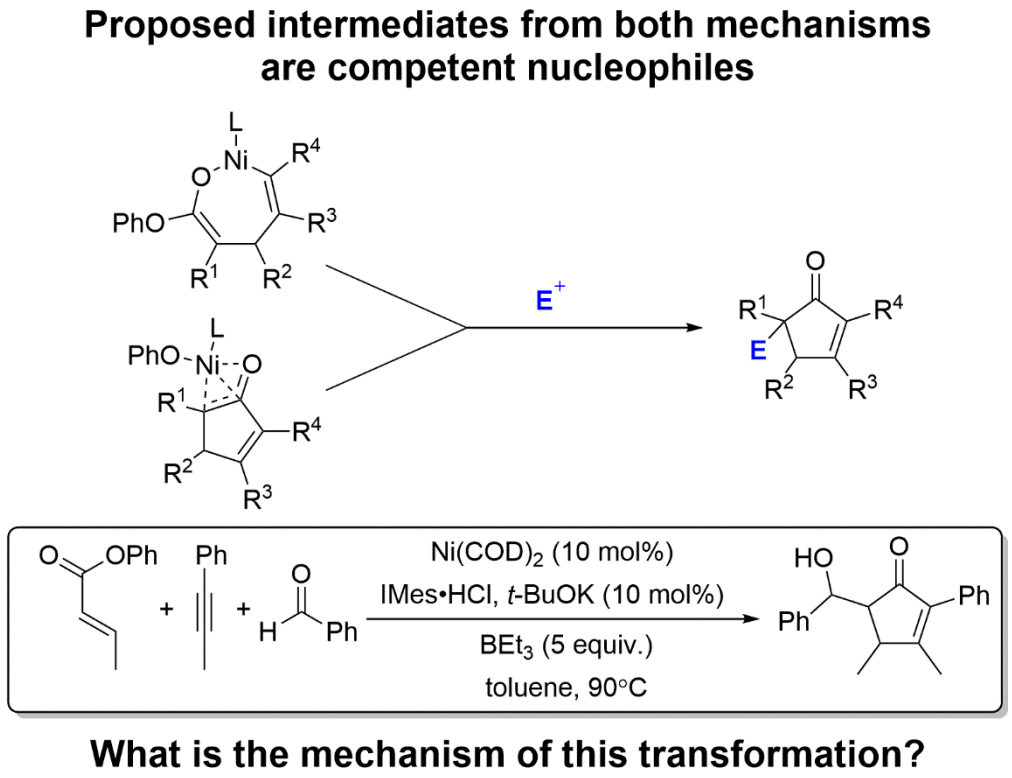

Figure 2-4. *(Top) Both Ogoshi and Montgomery propose intermediates that are vulnerable to electrophilic attack. (Bottom) The optimized conditions of the three-component coupling between an alkyne, aldehyde, and enoate. These conditions are used as the basis for the computational study*

Through careful optimization of reaction conditions, Montgomery group student Aireal Jenkins was able to realize a catalytic, three-component coupling reaction by incorporating an aldol reaction in with the [3+2] reductive cycloaddition of an enoate and alkyne (Figure 2-4, bottom). With a working reaction in hand, it was at this point that computational analysis was requested.

The goals of the computational study were to clarify the mechanism through which the three-component coupling occurs. While multiple sets of conditions were developed for the reaction, including using either phosphine ligand PBu_3 or NHC (N-heterocyclic carbene) ligand IMes, the conditions listed in Figure 2-4 were chosen for computational study due to the popularity of NHC ligands in the more recent reductive coupling work by the Montgomery group.[54]

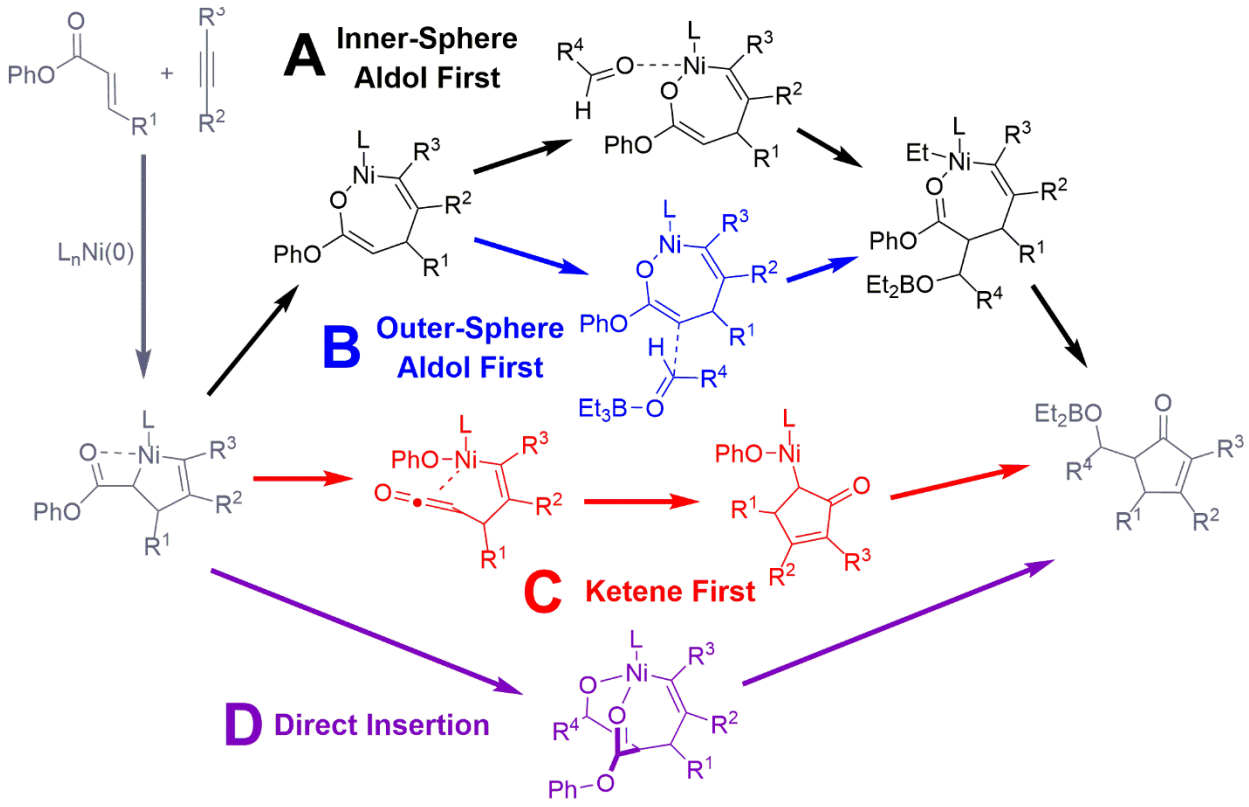

Figure 2-5. *The four possible mechanisms investigated in the studied reaction.*

Based on the mechanisms proposed by Montgomery[50] and Ogoshi[51] in their respective reports, as well as from reviewer input in the publication of the data in this chapter, four possible mechanisms for the three-component coupling can be envisioned (Figure 2-5). Pathways A and B are based on the mechanistic proposal of Montgomery, with the intermediacy of a 7-membered metallacycle. In these so-called "aldol-first" pathways, the aldol addition occurs prior to carbocyclization. In pathway A, the unit of aldehyde coordinates directly to the metal center, allowing for an inner-

sphere aldol addition. In pathway B, the aldol addition occurs in an outer-sphere process without any prior aldehyde coordination. Pathway C is a "ketene first" mechanism based off of the mechanistic proposal of Ogoshi, where carbocyclization occurs prior to aldol addition. And in the lass possible mechanism, pathway D, a coordinated aldehyde inserts directly into the 5-membered metallacycle, based off of reviewer comments during publication review.

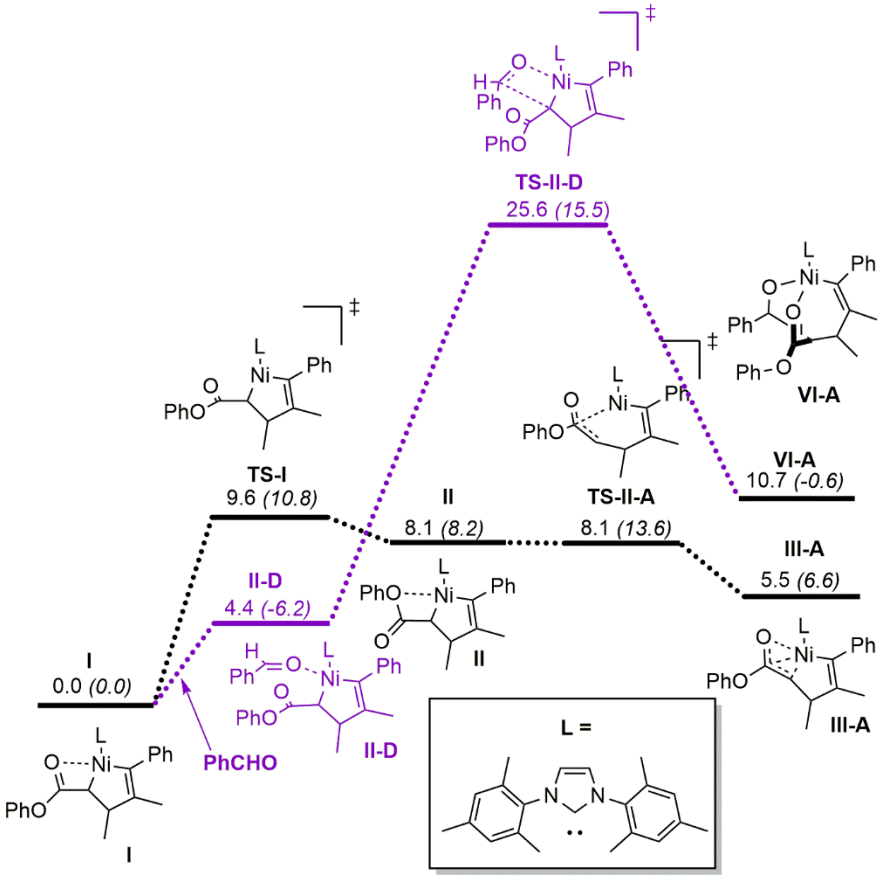

Figure 2-6. *Isomerization of metallacycle* ***I*** *to* η^3*-bound* ***III-A****, and direct insertion through pathway D. Pathway D is denoted in purple. Energies are given in kcal/mol, with enthalpies listed in parentheses. Energies are given in kcal/mol, with enthalpies listed in parentheses.*

As all four investigated mechanisms begin with the oxidative cyclization of the enoate and alkyne, metallacycle **I** (Figure 2-6) is used as the reference structure. In order to isomerize to the 7-membered metallacycle, **I** must first isomerize to η^3 intermediate **III-A**, via rotation (**TS-I**) to isomer **II**, followed by carbonyl binding (**TS-II-A**) to yield **III-A**. Additionally, it is also possible

for benzaldehyde to coordinate to metallacycle **I** to yield complex **II-D**, which can then directly insert (**TS-II-D**), to create tetracoordinate species **VI-A**.

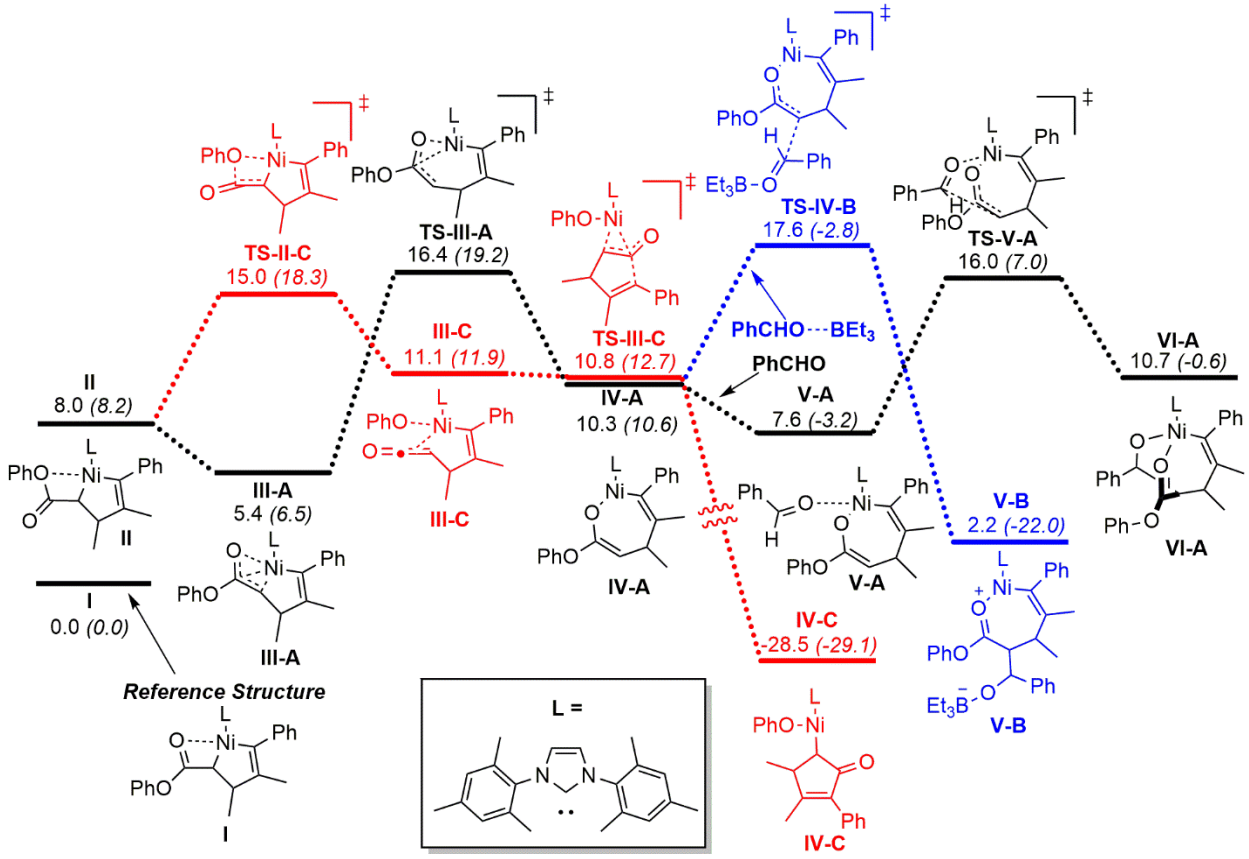

Figure 2-7. *Comparison of the aldol-first (paths A, B) and ketene-first (path C) mechanisms. Path A (black): inner-sphere aldol-first mechanism; Path B (blue): outer-sphere aldol-first mechanism; Path C (red): ketene-first mechanism. Energies are given in kcal/mol, with enthalpies listed in parentheses.*

Using structure **I** as an energy reference, the remaining pathways (A, B, and C) are also examined (Figure 2-7). Complex **II** acts as the branching point between aldol-first mechanisms A and B, and ketene-first mechanism C. Species **II** can isomerize to **III-A** (Figure 2-6), and then isomerize again to 7-membered metallacycle **IV-A** (**TS-III-A**). Here paths A and B separate. In path A, benzaldehyde coordinates to **IV-A** to create **V-A**, which then undergoes inner-sphere aldol addition (**TS-V-A**) to yield tetracoordinate species **VI-A**. In path B, a benzaldehyde-BEt_3 complex adds to **IV-A** (**TS-IV-B**), to yield **V-B**.

In path C, rather than isomerize to **III-A**, species **II** instead undergoes ketene elimination (**TS-II-C**) to create ketene complex **III-C**. Complex **III-C** then undergoes carbocyclization (**TS-III-C**), to yield nickel enolate **IV-C**. As the formation of **IV-C** is highly exergonic (-28.5 kcal/mol relative to **I**), its formation is expected to be irreversible under the studied conditions. Furthermore, the relatively low barrier for the formation of **IV-C** (highest barrier process is **TS-II-C**, 15.0 kcal/mol) compared to the barrier for isomerization to a 7-membered metallacycle (**TS-III-A**, 16.4 kcal/mol), or the barrier for direct insertion of an aldehyde (**TS-II-D**, 25.6 kcal/mol), means that the formation of **IV-C** in pathway C is expected to outcompete pathways A, B, and D. Based off of the potential energy surfaces detailed in Figures 2-6, and 2-7, therefore, it was found that ketene-first pathway C is expected to be the dominant reaction pathway in the studied reaction.

2.4 Determining the Fates of Complexes VI-A, V-B, and IV-C

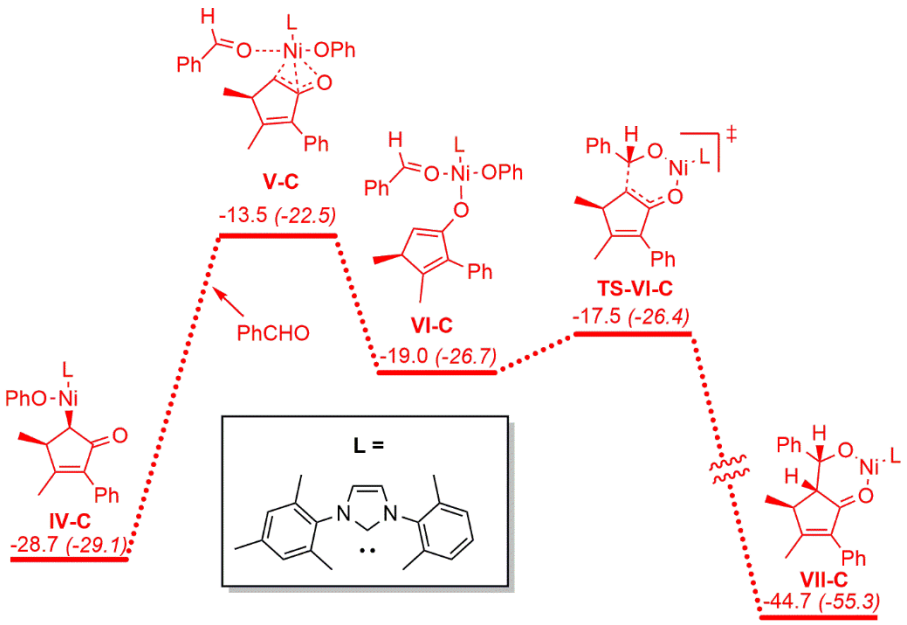

Figure 2-8. *Aldol addition in pathway C. Energies are given in kcal/mol, with enthalpies listed in parentheses.*

After carbocyclization to form intermediate **IV-C**, the aldol addition in pathway C is expected to occur through an inner-sphere pathway (Figure 2-8). Coordination of benzaldehyde to **IV-C** yields

complex **V-C**, which can then isomerize to O-bound enolate species **VI-C**. The O-bound enolate can then engage in rapid aldol addition (**TS-VI-C**), to yield aldol adduct **VII-C**. After aldol addition, catalyst turnover can then be accomplished by reaction of **VII-C** with triethylboron.

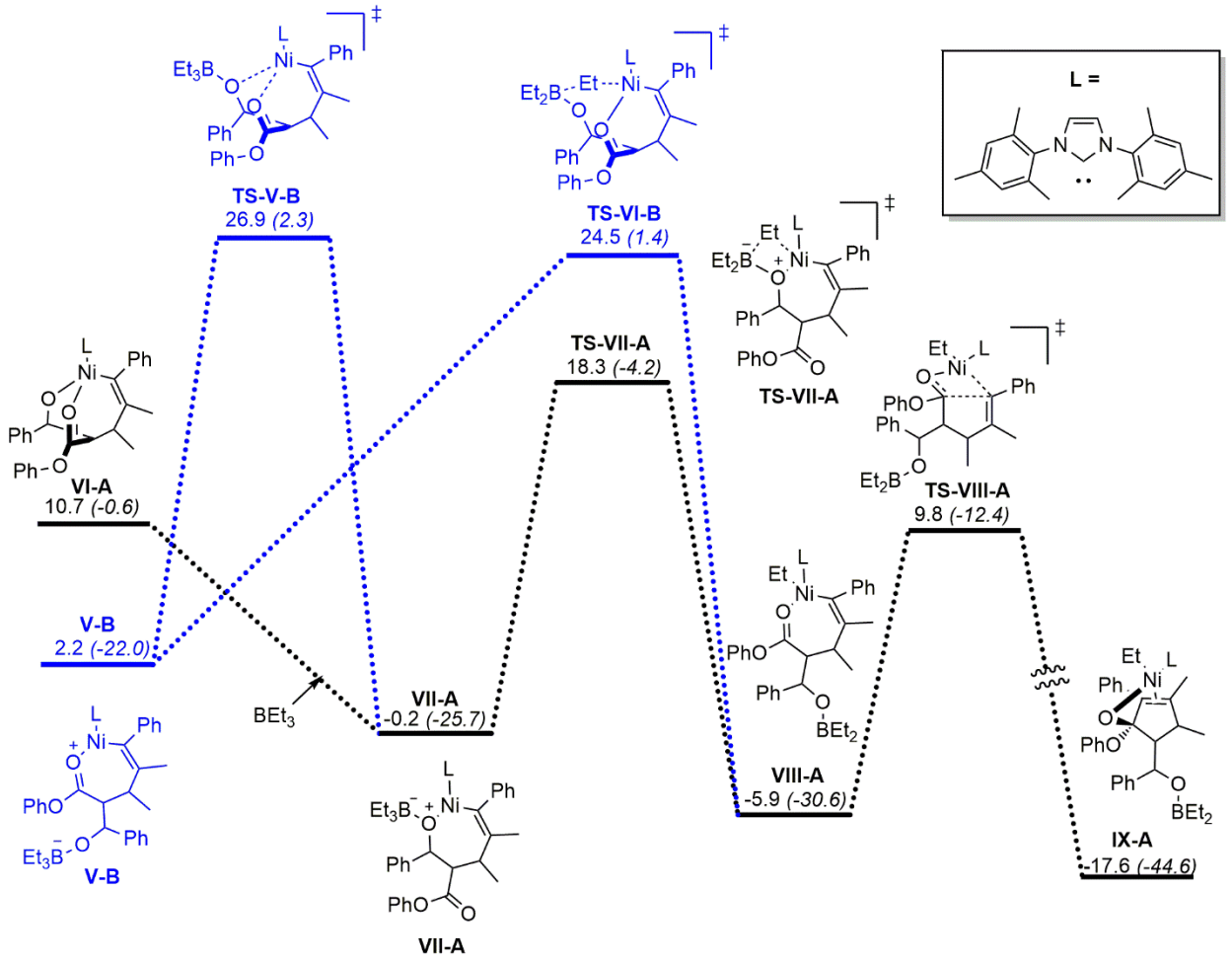

Figure 2-9. *Carbocyclization in paths A and B. Energies are given in kcal/mol, with enthalpies listed in parentheses.*

Though Figure 2-7 shows that ketene-first pathway C is expected to be the major pathway in the three-component coupling of an alkyne, aldehyde, and enoate, the evaluation of pathways A, and B is still beneficial (Figure 2-9). In particular, evaluating the carbocyclization of paths A and B distinguishes between those reaction pathways being viable mechanisms that might emerge under perturbation of the reaction conditions, or being unfeasible mechanisms that should not be

considered in the future. Both intermediates **VI-A** and **V-B** eventually converge to ethyl-nickel species **VIII-A**. In path A, coordination of triethylboron to **VI-A** yields complex **VII-A**. This species can then transfer an ethyl group to the nickel center to create **VIII-A**. In pathway B, isomerization to **VII-A** (**TS-V-B**) is a higher barrier process compared to direct ethyl transfer (**TS-VI-B**) to yield complex **VIII-A**. After formation of **VIII-A**, carbocyclization (**TS-VIII-A**) can proceed, resulting in carbocycle **IX-A**, which is expected to be capable of extruding a unit of phenoxide, and ultimately turning over the nickel catalyst.

While pathway C is expected to be the dominant pathway for catalyst activation, pathway A has an overall barrier that is only slightly higher in energy. The highest overall barrier for path A is nickel ethylation (**TS-VII-A**, Figure 2-9) at 18.5 kcal/mol, 2.5 kcal/mol shy of the largest net barrier for pathway C prior to carbocyclization (**TS-II-C**, Figure 2-7). Pathways B and D both have much larger overall barriers (path B: **TS-VI-B**, 24.5 kcal/mol, path D: **TS-II-D**, 25.6 kcal/mol), and can be considered to be much less feasible reactions compared to paths A and C.

2.5 Considering the Reactivity of α-Substituted Enoates

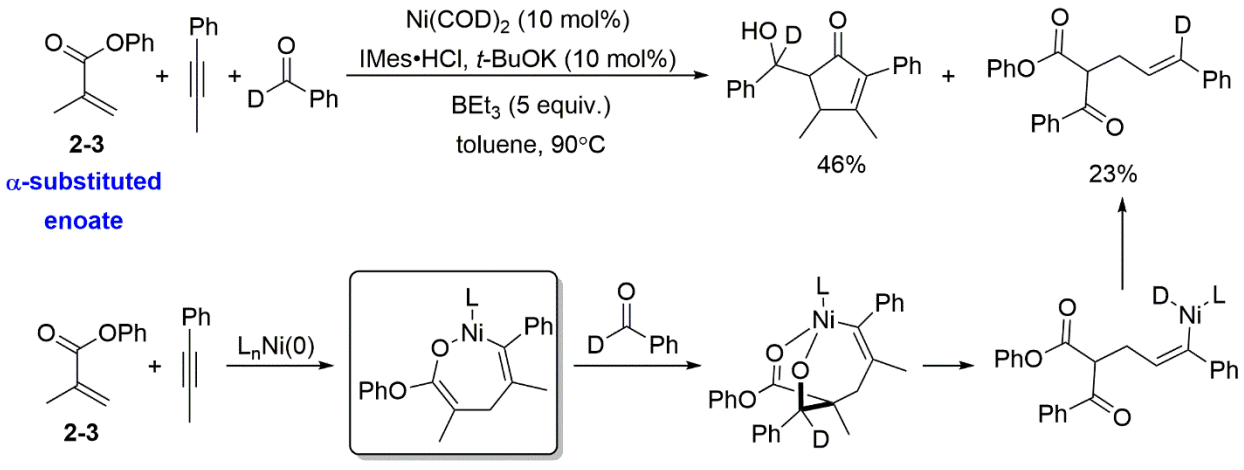

Figure 2-10. *Formation of a linear side product in the studied reaction using an α-substituted enoate. The existence of such a product implicates formation of a 7-membered metallacycle (boxed).*

The potential energy surfaces shown in Sections 2.3 and 2.4 detail a three-component coupling reaction involving a β-substituted enoate. However, it is already known that α-substituted enoate **2-3** is capable of producing a linear side product, which implicates the existence of a 7-membered metallacycle (Figure 2-2). Furthermore, in the development of the three-component coupling reaction, Aireal Jenkins was also able to identify the formation of a linear product using **2-3** (Figure 2-10). These points of evidence suggest that the mechanism of the reductive [3+2] cycloaddition between an enoate and an alkyne, and by extension, the three-component coupling reaction studied, go through different mechanisms, depending on the substitution pattern of the enoate.

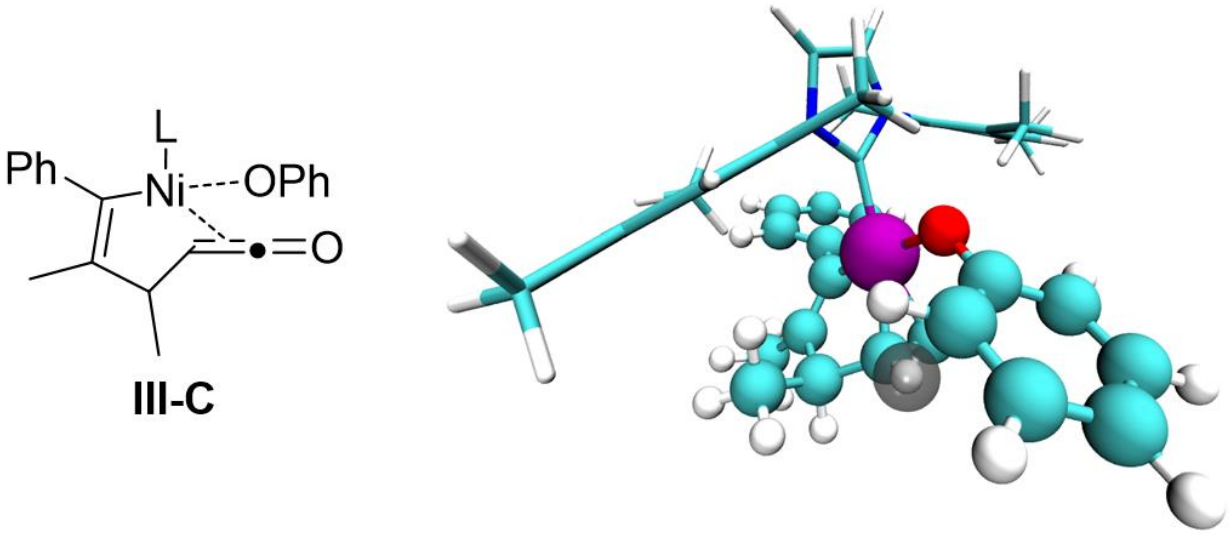

Figure 2-11. *The phenoxide moiety moves close to the α position (highlighted in gray) after ketene elimination. Increasing the steric hinderance at that position is expected to destabilize complex **III-C**.*

Closer examination of the geometry of the ketene elimination product (**III-C**, Figure 2-7) suggests a rationale for why such a perturbation in mechanism might take place. Figure 2-11 details the geometry of **III-C**. Notably, after eliminating the phenoxide moiety to form a ketene, the phenoxide in the resulting complex is oriented close (2.3 Å) to the hydrogen in the α position (highlighted in gray). If the α position were to become more sterically crowded, it could be imagined that ketene elimination would become more difficult.

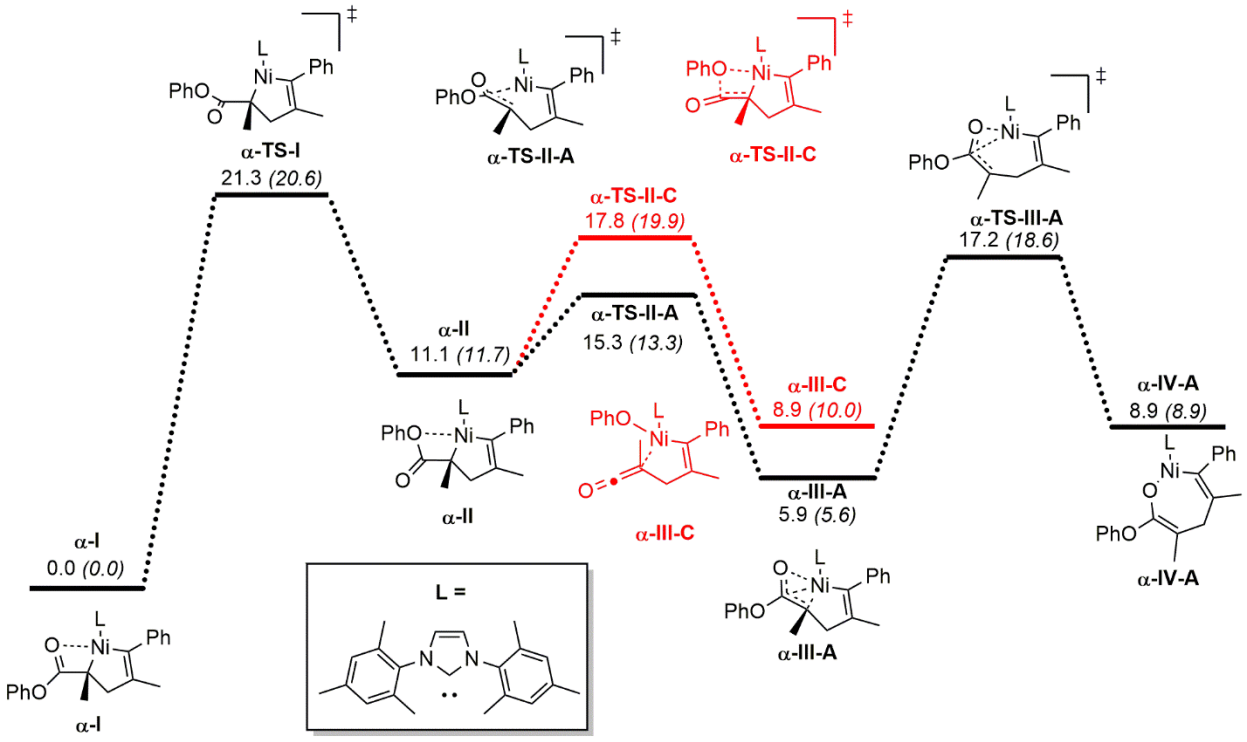

Figure 2-12. *The potential energy surface for the first few steps of the [3+2] cycloaddition between an alpha substituted enoate and an alkyne. Energies are given in kcal/mol, with enthalpies listed in parentheses.*

Based off of this observation, the early stages of metallacycle isomerization were investigated computationally for the three-component coupling reaction involving starting enoate **2-3**. The potential energy surface for these initial steps are shown in Figure 2-12. After isomerization of metallacycle **α-I** to rotamer **α-II**, the complex can either undergo ketene elimination to form complex **α-III-C**, or isomerization to yield 7-membered metallacycle **α-IV-A**. Unlike the reaction of a β-substituted enolate, metallacycle formation is expected to outcompete ketene elimination when an α-substituted enoate is used, as both the of the transition states associated with the formation of the metallacycle (**α-TS-II-A**, 15.3 kcal/mol and **α-TS-III-A**, 17.2 kcal/mol) are lower in energy than the transition state for ketene elimination (**α-TS-II-C**, 17.8 kcal/mol).

The differences between the potential energy surfaces of the α- and β-substituted enoates can be more clearly seen if the respective surfaces are lined up next to each other (Figure 2-13). While

changing from a β-substituted enoate to an α-substituted one increases the barrier for isomerization to the 7-membered metallacycle by 0.8 kcal/mol (**TS-III-A** vs **α-TS-III-A**), the barrier for ketene elimination increases by a much larger amount, 2.8 kcal/mol (**TS-II-C** vs **α-TS-II-C**). The 2.0 kcal/mol net swing in energy means that ketene elimination changes from being favored by 1.4 kcal/mol to being disfavored by 0.6 kcal/mol, relative to isomerization to the 7-membered metallacycle.

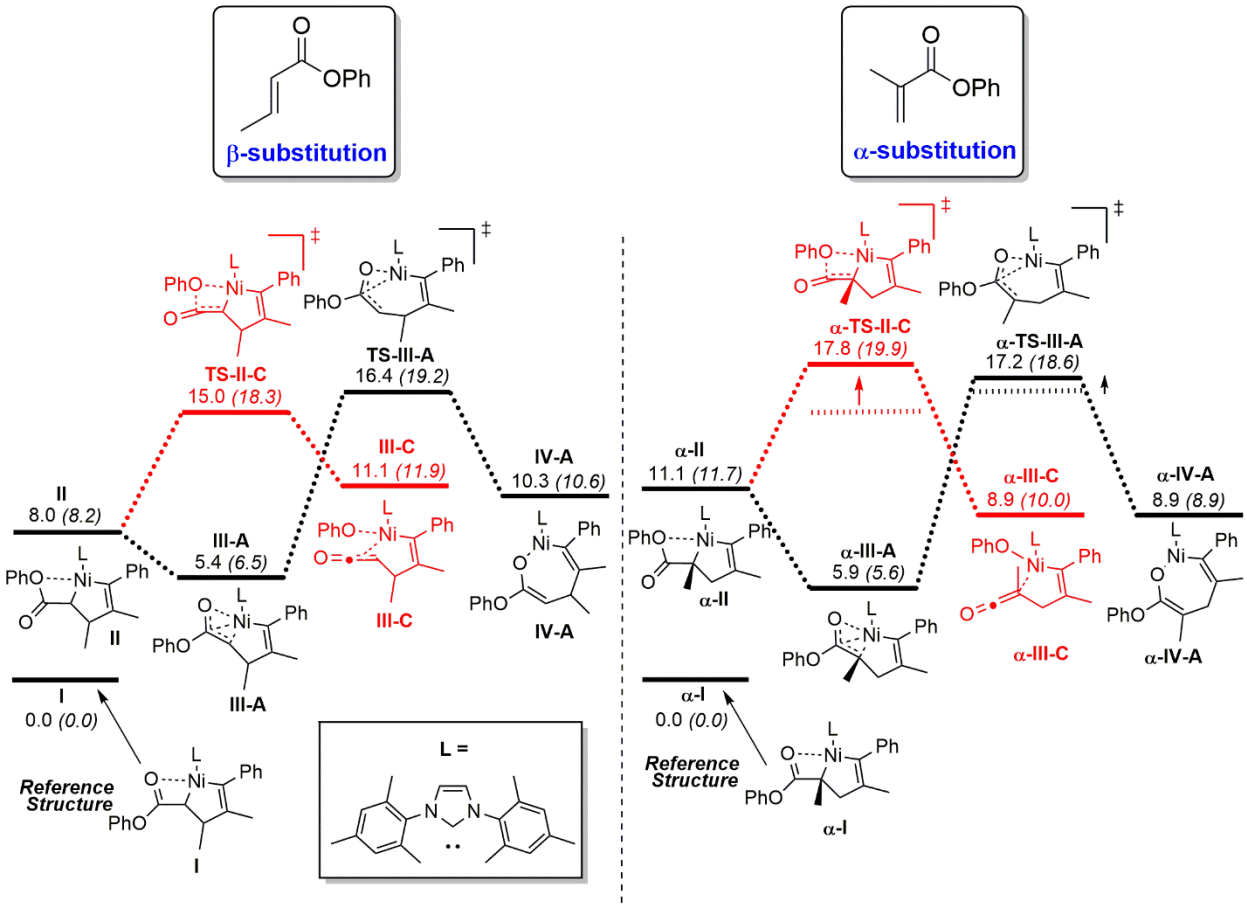

Figure 2-13. *Comparing the barrier to ketene elimination with isomerization to the 7-embered metallacycle for both the α- and β-substituted enoates.*

Even though metallacycle formation is now capable of outcompeting ketene elimination, this does not guarantee that the three-component coupling of **2-3** goes through an aldol-first type mechanism. It is possible that ketene elimination could outcompete steps further along the

potential energy surface of the aldol-first path, such as triethylboron addition. However, the change does explain how linear side products that necessitate the formation of a 7-membered intermediate can occur when **2-3** is used as an enoate, and may also explain why linear side products aren't typically seen using β-substituted enoates.[55]

2.6 Summary and Conclusions

In summary, the mechanism of a three-component coupling reaction (Figure 2-4) was studied. Prior work from both Montgomery[50] and Ogoshi[51] has shown that multiple mechanisms are possible in the reductive [3+2] cycloaddition of an enoate and alkyne, leaving the mechanism of the three-component coupling reaction developed by Jenkins as ambiguous. In evaluating the potential energy surface of the three-component coupling, it was found that both an aldol-first mechanism involving a 7-membered metallacycle, and a ketene-first mechanism involving a ketene intermediate, are feasible reaction pathways. The ketene-first mechanism (labelled pathway C) appears to be preferred, due to the ability of ketene elimination to outcompete isomerization to the 7-membered metallacycle. However, a precarious balance exists between path C and an inner-sphere aldol-first mechanism (labelled pathway A). Small perturbations in the reaction conditions, such as using an α-substituted enoate rather than a β-substituted one, appear to be capable of shifting the mechanism towards aldol-first pathway A. This carries implications for any future work with nickel-catalyzed reductive [3+2] cycloadditions, including Chapter 3 of this thesis. This study also showcases the limits of presuming a catalytic mechanism based off of similar prior work. It is possible for two slightly different substrates to react with the same catalyst to make the same corresponding product, but to do so through completely different mechanisms. Experimentalists should use this work as an example for why one should use caution when applying their untested mechanistic postulations to new reactions.

Chapter 3: Elucidation of the Activation Mechanism of Air-Stable Nickel(0) Catalysts

Some of the material presented in this chapter has been reported in *ACS Catalysis.*[56]

3.1 Motivation for the Development of Air-Stable Nickel Pre-Catalysts

Homogeneous nickel catalysis has seen considerable advancements over the past two decades.[57–59] Nickel has played a role in transformations such as C-C bond formation,[60–63] C-N bond formation,[64,65] C-O bond formation,[65] C-O activation,[61,66–68] C-H activation,[69–71] decarbonylative couplings,[72] π-component couplings,[54,73] and polymerization reactions.[74] While related group 10 metal palladium was the dominant catalyst for many of these transformations, resulting in the 2010 Nobel Prize in Chemistry,[75] nickel has seen an increase in interest, not only as it is over 5,000 times more abundant in the earth's crust,[76] but also because it is unique suited for reactions such as alkyl cross-coupling or π-component coupling.[57]

Despite the great promise of nickel catalysts, there are still many barriers to its adoption. Compared to palladium, nickel generally requires higher catalyst loadings.[77] Additionally, many of the commonly used nickel precursors, such as $Ni(COD)_2$ (bis(cyclooctadiene)nickel(0)), are air-sensitive, and require the use of a glovebox.[57] Both of these problems can potentially be addressed through the development of new, air-stable nickel pre-catalysts.

The use of pre-catalyst, with the desired ligands already bound to the metal center, is an effective strategy for lowering the amount of catalyst needed for a chemical transformation.[77] *In-situ* complex formation introduces ambiguity about the nature and quantity of active catalyst involved

in the reaction. A portion of the metal introduced may fail to ligate, or may be ligated in an unproductive manner. If only a small portion of the metal and ligand introduced form an active catalytic complex, then observed catalyst turnover number will be artificially lowered. The failure of the majority of introduced metal to form a competent catalyst artificially lowers the observed turnover number. Consequently, by using a pre-catalyst, where all of the material is already ligated, similar yields to *in-situ* procedures can be obtained using much lower catalyst loadings, or much higher yields can be obtained with the same catalyst loading.

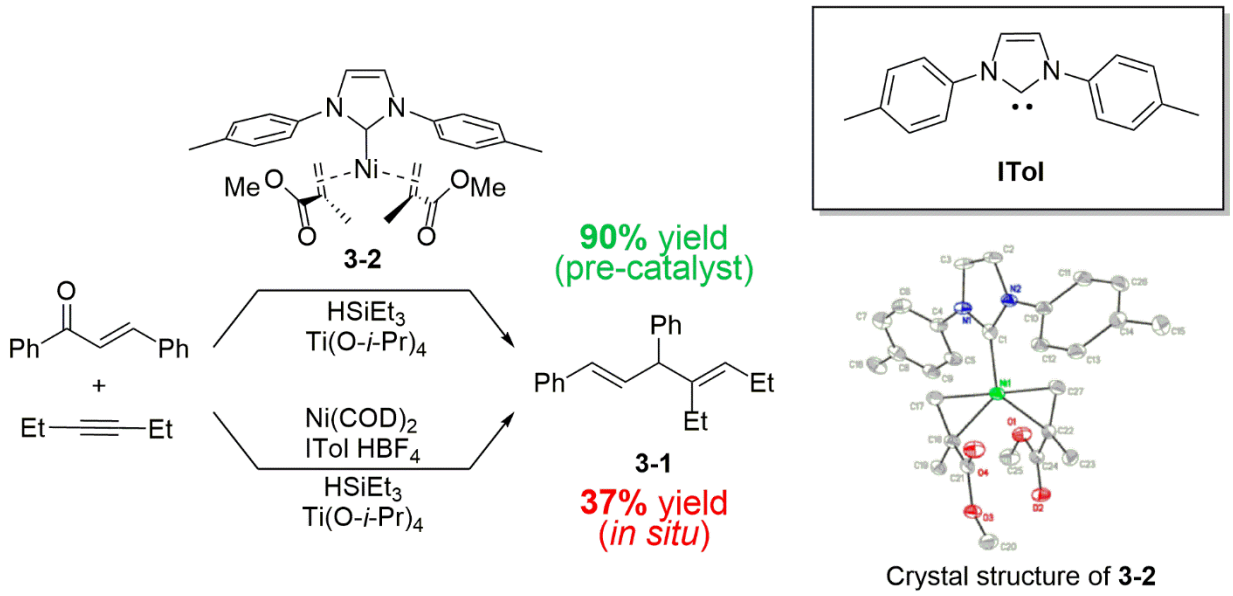

Figure 3-1. *Use of a pre-catalyst dramatically improves the yield of* ***3-1****. Crystal structure taken from reference 78.*

An example of this effect is illustrated by a publication from the Montgomery group.[78] A nickel(0) catalyst in conjunction with small NHC (N-heterocyclic carbene) ligand ITol was found to be an effective combination for the deoxygenative coupling of an unsaturated aldehyde or ketene with an alkyne, to form skipped diene species **3-1** (Figure 3-1). While the *in-situ* formation of the catalyst gave poor yields, use of pre-ligated complex **3-2** gave much improved yields. The success of **3-2** as a catalyst in this transformation demonstrates the power of using a pre-catalyst: the same

amount of metal and ligand are used, but using an isolable, pre-ligated species ensures that all of the material added is catalytically active.

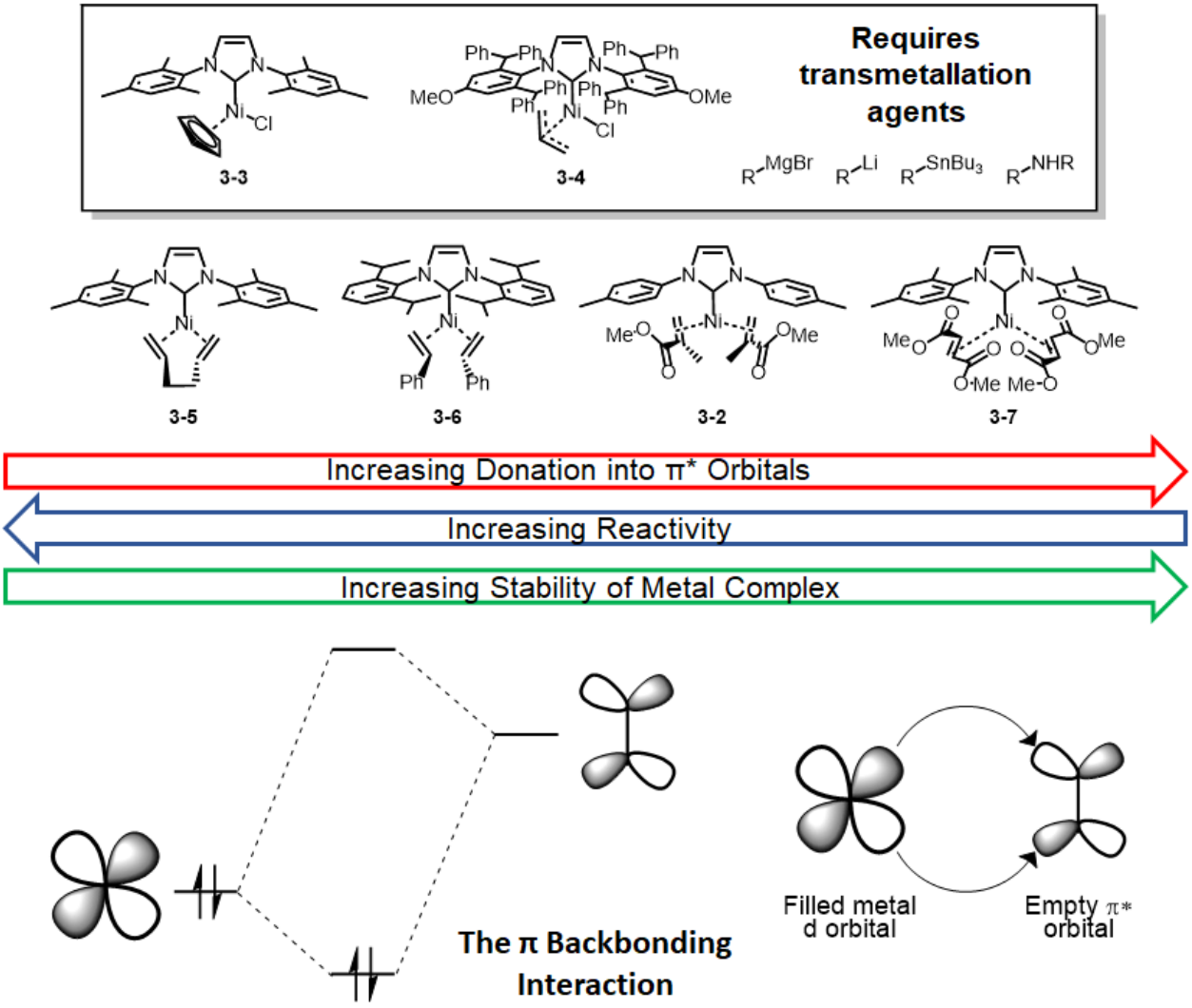

Figure 3-2. *(Top) Air-stable Ni(II) catalysts require a transmetallation reagent. (Middle) Tradeoffs in the development of Ni(0) pre-catalysts. (Bottom) Molecular orbital diagram for the π backbonding interaction.*

Many of the reactions developed by the Montgomery group have utilized a low-valent nickel complex in conjunction with an NHC ligand, largely for the purposes of coupling π-components.[54] While air-stable pre-catalysts that include a ligated NHC ligand already exist, most of them are Ni(II) species such as **3-3**[79] and **3-4**[80]. Such Ni(II) precursors are competent for reactions that involve a transmetallating reagent, and do not have a clear means of activation for reactions that

only involve π-components and silanes (Figure 3-2, Top). For this reason, Ni(0) pre-catalysts bound to π-acceptor ligands such as **3-5**,[81] **3-6**,[82] **3-2**,[78] or **3-7**[83] were considered. In the choice of olefin, a tradeoff emerges between catalyst activity and air-stability (Figure 3-2, Middle). The more electron-poor the ligand, the better it is able to engage in a π-backbonding interaction, where the d orbitals of the metal interact with the π* antibonding orbitals of the olefin (Figure 3-2, Bottom). A greater the backbonding interaction increases the stability of the complex, as it pulls electron density away from the metal center, reducing the metal's susceptibility towards oxidation. However, an increased backbonding interaction will also increase the π-acceptor's binding energy, make fumarate dissociation more difficult, and preventing the generation of an active catalyst.

3.2 Investigating a Diverse Set of Nickel Fumarate Complexes

In this context, the development of an air-stable nickel catalyst with a carbene ligand already bound was sought. Fumarate complexes such as **3-7** were chosen as a starting point in this investigation, as such complexes were reported to be air-stable,[83] but unreactive towards π-component couplings in our hands. Given the trends seen with olefin ligands, it was expected that an inverse relationship between reactivity and stability would occur. With this hypothesis in hand, the design strategy was to develop fumarate catalysts that might have greater steric clashes with the NHC ligand, weakening the fumarate-Ni interaction enough to enable ligand exchange (Figure 3-3, Top).

Visiting student Santiago Cañellas and Montgomery student Alex Nett synthesized nine different fumarate complexes using the IMes NHC, and then they tested their ability to engage in the reductive coupling reaction to produce **3-9** (Figure 3-3, Bottom). In general, all of the tested fumarate complexes were found to be more active than Cavell's originally reported complex (**I**).[83] Most of the aryl fumarate complexes gave low to moderate yields (**E**, **F**, **G**, **H**), but complexes of fumarates **A** and **C** gave high yields of **3-9**, as well as complexes of alkyl fumarates **B** and **D**.

These 4 fumarate complexes were then subsequently tested for their air stability, and all 4 (**A** through **D**) were found to be air-stable.

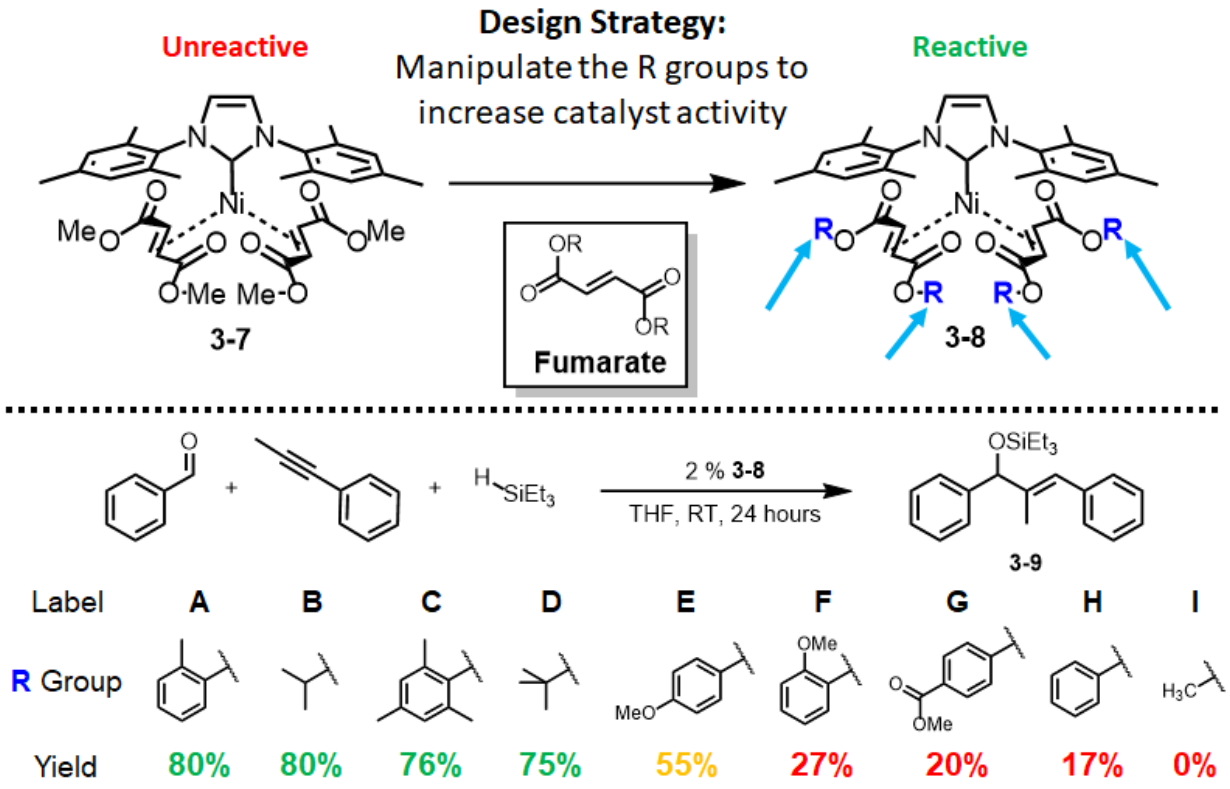

Figure 3-3. (Top) Different fumarate complexes were synthesized. (Bottom) The different complexes were tested for their ability to catalyze a reductive coupling reaction.

However, the discovery of air-stable, reactive Ni(0) IMes fumarate catalysts was not found to be easily transferred to other NHCs. For instance, Montgomery group student Amie Frank was unable to use complexes of fumarate **A** with a chiral NHC,[84] or smaller carbene ligand BAC[85] for a reductive coupling reaction, even at higher catalyst loadings compared to complex **3-8-A**. The incompetence of catalysts **3-10-A** and **3-11-A** suggested that a greater understanding of the catalyst activation process was necessary, and that the identity of the fumarate used may need to be tuned based on the NHC used in the complex.

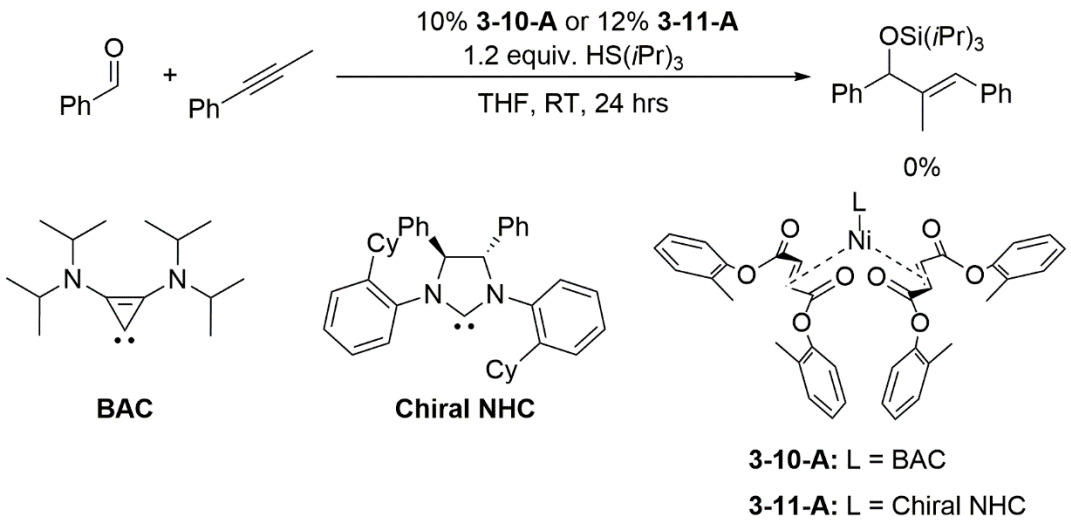

Figure 3-4. *Other complexes of fumarate A are not competent in reductive couplings.*

3.3 Overturning the Original Hypothesis that Catalyst Activation Occurs *via* Dissociation

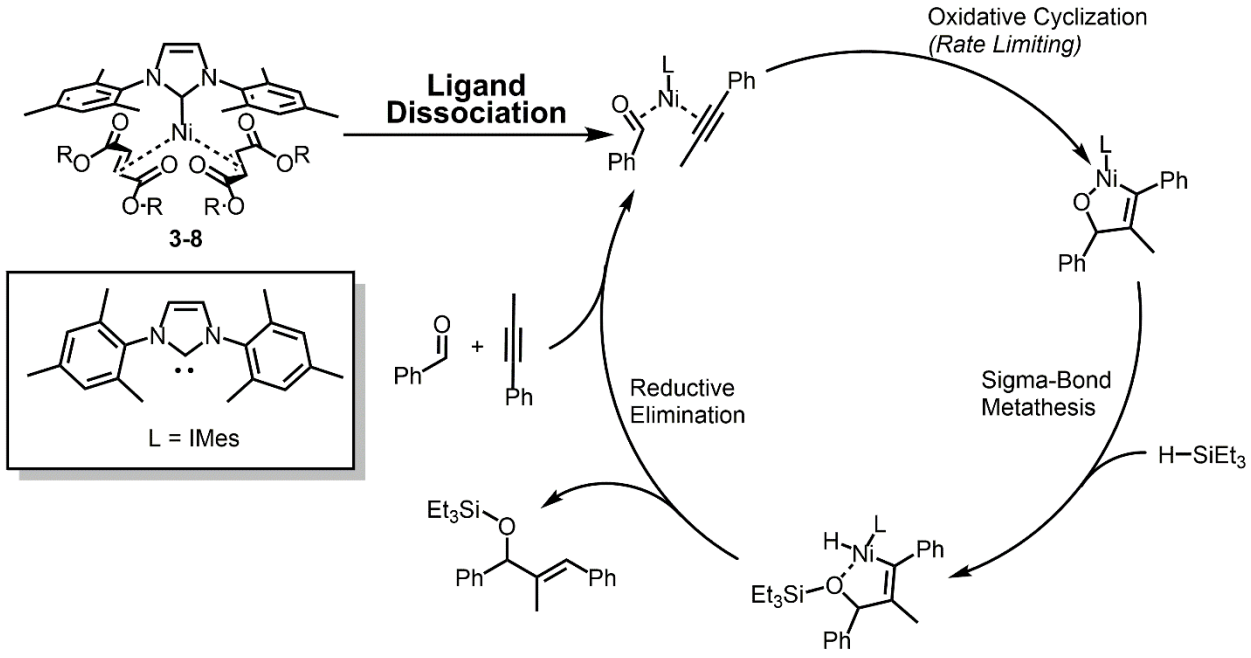

Figure 3-5. *The mechanism of the reductive coupling reaction. Originally ligand dissociation was believed to be the means of catalyst activation.*

In the synthesis of complexes **3-8**, the design strategy was to change the identity of the R group to increase steric repulsion between the fumarate and metal center. Given the mechanism of the

reductive coupling reaction (Figure 3-5), it was thought that the metal center needed to have 2 free coordination sites in order to perform catalysis. This necessitates some form of ligand dissociation to allow for binding of the alkyne and aldehyde starting material.

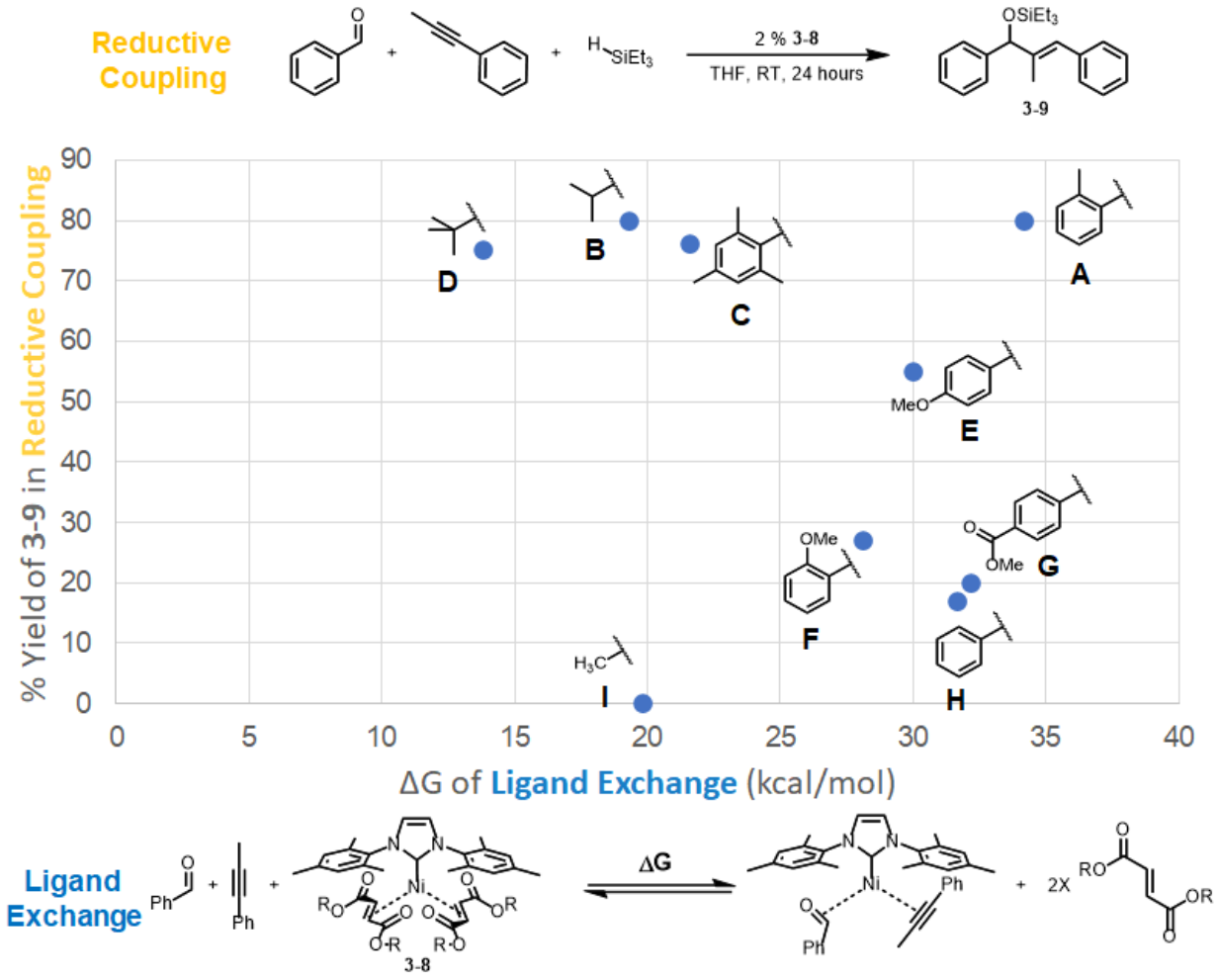

Figure 3-6. *The relationship between the free energy of ligand exchange and the yield of* ***3-9*** *in reductive coupling attempts with the corresponding catalyst. Computational details are included in the appendix.*

Notably, the hypothesis that dissociative ability of a fumarate complex determines its catalytic ability can be easily tested computationally. The free energy of ligand exchange was calculated for each fumarate complex listed in Figure 3-3, and then that energy was compared to the yield of **3-9** that was observed experimentally. If it was the case that ligand dissociation determined catalytic ability, it would be expected that some form of statistical relationship should emerge

between the free energy of dissociation and the observed yields. However, no relationship between reaction yield and computed binding affinity was found (Figure 3-6).

The lack of correlation seen in Figure 3-6, suggested that a fumarate dissociation mechanism was not the mechanism of catalyst activation, as was originally thought. As fumarate dissociation for all of the studied complexes **3-8** was found to be endergonic, it can be concluded that all of the studied fumarates can act as a catalyst poison. Even if the weakest bound fumarate, **D**, is considered, it would be expected that dissociation of **3-8-D** to form a nickel-aldehyde-alkyne complex would raise the energy of the subsequent oxidative addition step by 13.8 kcal/mol, slowing the reaction down by a factor of over 10 billion. It follows then, that since many members of catalysts **3-8** are capable of producing **3-9**, it must be the case that their corresponding fumarates are consumed prior to formation of product **3-9**. Were this hypothesis to be true, it should be possible to isolate the products of such a fumarate consumption reaction. Using this prediction, Montgomery student Ellen Butler investigated the reactivity of catalyst **3-8-A** in greater detail. Under conditions similar to the reductive coupling reaction, products **3-12** and **3-13** were isolated by reacting **3-8-A** with phenyl propyne, 4-fluorobenzaldehyde, and triethyl silane. (Figure 3-7). As **3-12** is very similar to the products formed in the three-component coupling studied in Chapter 2, we hypothesized that catalyzed activation would occur through an analogous reaction.

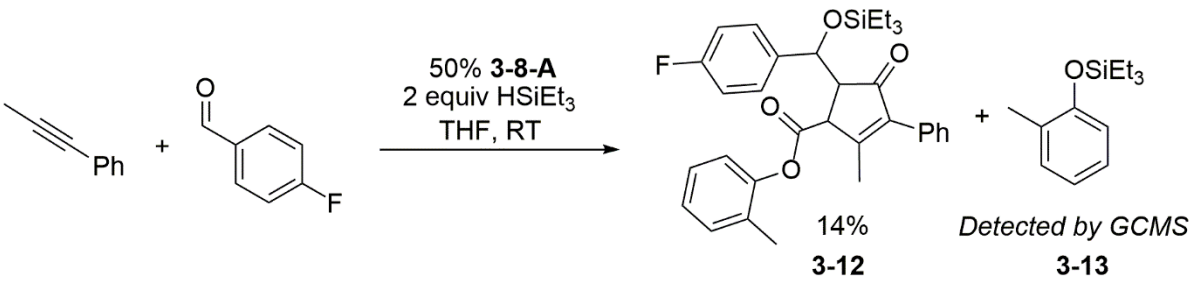

Figure 3-7. *The isolation of products **3-12** and **3-13** from catalyst **3-8-A**.*

3.4 Investigating the Activation Sequence of BAC and IMes Fumarate Complexes

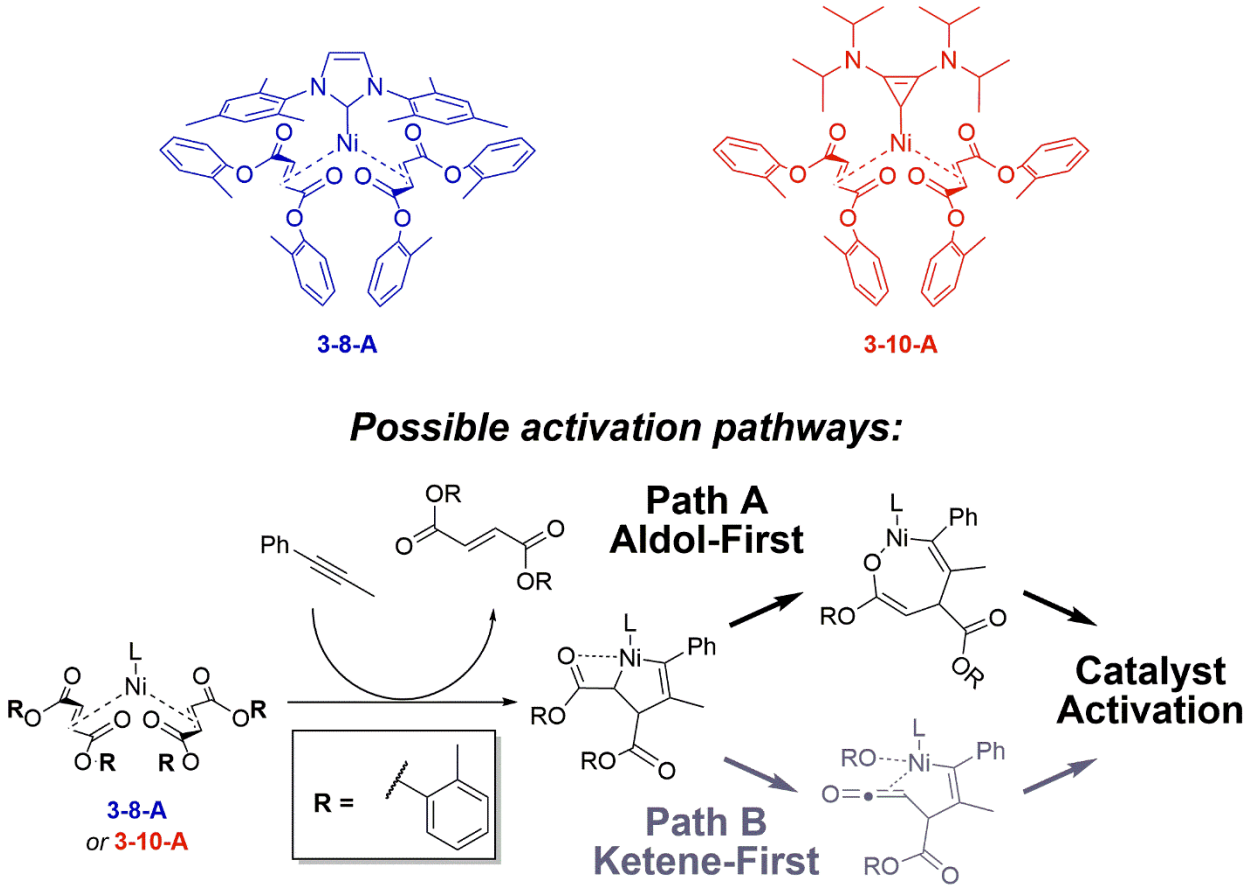

Figure 3-8. *Possible activation mechanisms for complexes of fumarate A.*

In Chapter 2, the formation of 3-component products such as **3-12** was found to occur through either an aldol-first or ketene-first type mechanism, depending on the identity of the π-component used in the transformation (Figure 3-8). To distinguish between the mechanisms of catalyst activation in **3-8-A**, as well as to investigate why catalyst **3-10-A** fails to successfully activate, the mechanism of catalyst activation of both the BAC and IMes complexes with fumarate **A** were investigated computationally.

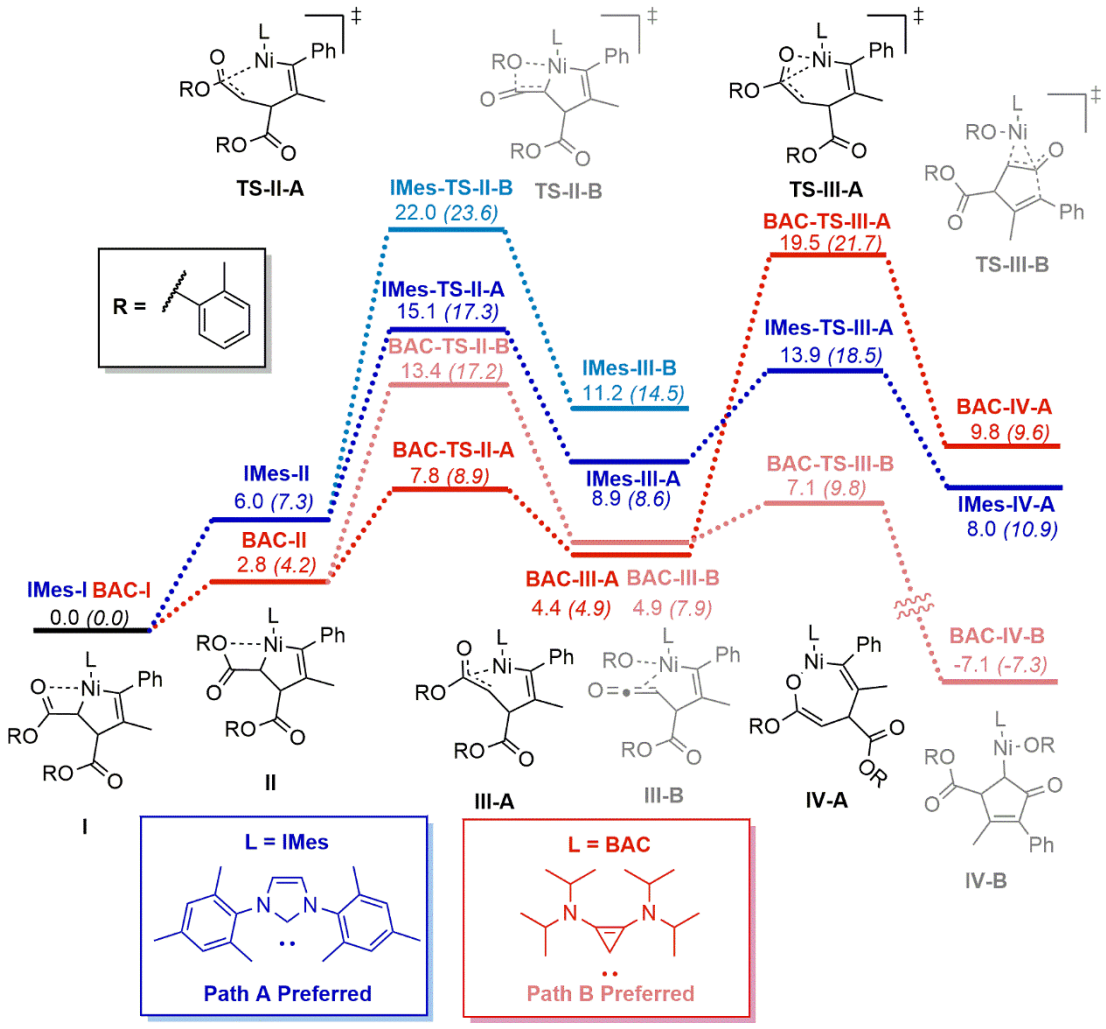

Figure 3-9. *The initial steps of activation for IMes complex* ***3-8-A*** *(blue and turquoise) and BAC complex* ***3-10-A*** *(red and pink). Dark colors (red, blue and black) represent aldol-first path A. Light colors (pink, turquoise, and gray) represent ketene-first path B. Energies are given in kcal/mol, with enthalpies listed in parentheses. Computational details are included in the appendix.*

The potential energy surfaces of the early steps of aldol-first path A and ketene-first path B for both IMes catalyst **3-8-A** (pathways shown in blue and turquoise, labelled as IMes) and BAC catalyst **3-10-A** (pathways shown in red and pink, labelled as BAC) are shown in Figure 3-9. In Chapter 2, it was demonstrated that the selectivity between an aldol-first reaction and a ketene-first reaction is dependent on the barrier of ketene elimination compared to the highest barrier step in the aldol-first process. The early steps listed in Figure 3-9, therefore, play a large role in determining the path-selectivity of catalyst activation in **3-8-A** and **3-10-A**.

In the initial steps of path A (dark colors), 5 membered metallacycle **I** rotates to isomer **II**, and then isomerizes to ξ-3 bound **III-A** (**TS-II-A**). Complex **III-A** then isomerizes again (**TS-III-A**) to 7-membered metallacycle **IV-A**. Alternatively, in path B (light colors), isomer **II** extrudes a unit of aryloxide (**TS-II-B**), to create ketene complex **III-B**. The ketene species can then cyclize (**TS-III-B**) to carbocyclic species **IV-B**.

BAC catalyst **3-10-A** and IMes catalyst **3-8-A** differ significantly in these early steps. For the BAC complex, ketene elimination (**BAC-TS-II-B**, 13.4 kcal/mol) is fast enough that it outcompetes isomerization of ξ-3 bound **BAC-III-A** to 7-membered metallacycle (**BAC-TS-III-A**, 19.5 kcal/mol). After forming ketene complex **BAC-III-B**, an irreversible carbocyclization can occur (**BAC-TS-III-B**, 7.1 kcal/mol), yielding carbocycle **BAC-IV-B**. Taken together, the larger barrier height of **BAC-TS-III-A** (19.5 kcal/mol) compared to **BAC-TS-II-B** (13.4 kcal/mol**)** indicates that BAC complex **3-10-A** prefers to undergo catalyst activation through path B.

However, IMes catalyst **3-8-A** behaves differently. For the IMes catalyst, isomerization of 5-membered **IMes-II-A** to ξ-3 bound **IMes-III-A** is the slowest step towards the formation of 7-membered **IMes-IV-A** (**IMes-TS-II-A**, 15.1 kcal/mol). Unlike the BAC complex, ketene elimination (**IMes-TS-II-B**, 22.0 kcal/mol) is too slow to outcompete isomerization to the 7-membered metallacycle. Due to the higher barrier for ketene formation, and the lower barriers for isomerization to the 7-membered metallacycle, path A is still a possible activation mechanism for the IMes catalyst, and would be expected to be the preferred mechanism of activation if it forms an intermediate that is sufficiently exergonic compared to starting metallacyle **IMes-I.**

As the preliminary steps for paths A and B suggested that IMes catalyst **3-8-A** and BAC catalyst **3-10-A** undergo activation by different mechanisms, we hypothesized that the difference in mechanism can explain why **3-8-A** is a competent catalyst, but **3-10-A** is not. In order to evaluate

this hypothesis, the progress of path A with **3-8-A** and path B with **3-10-A** was traced further down their respective potential energy surfaces.

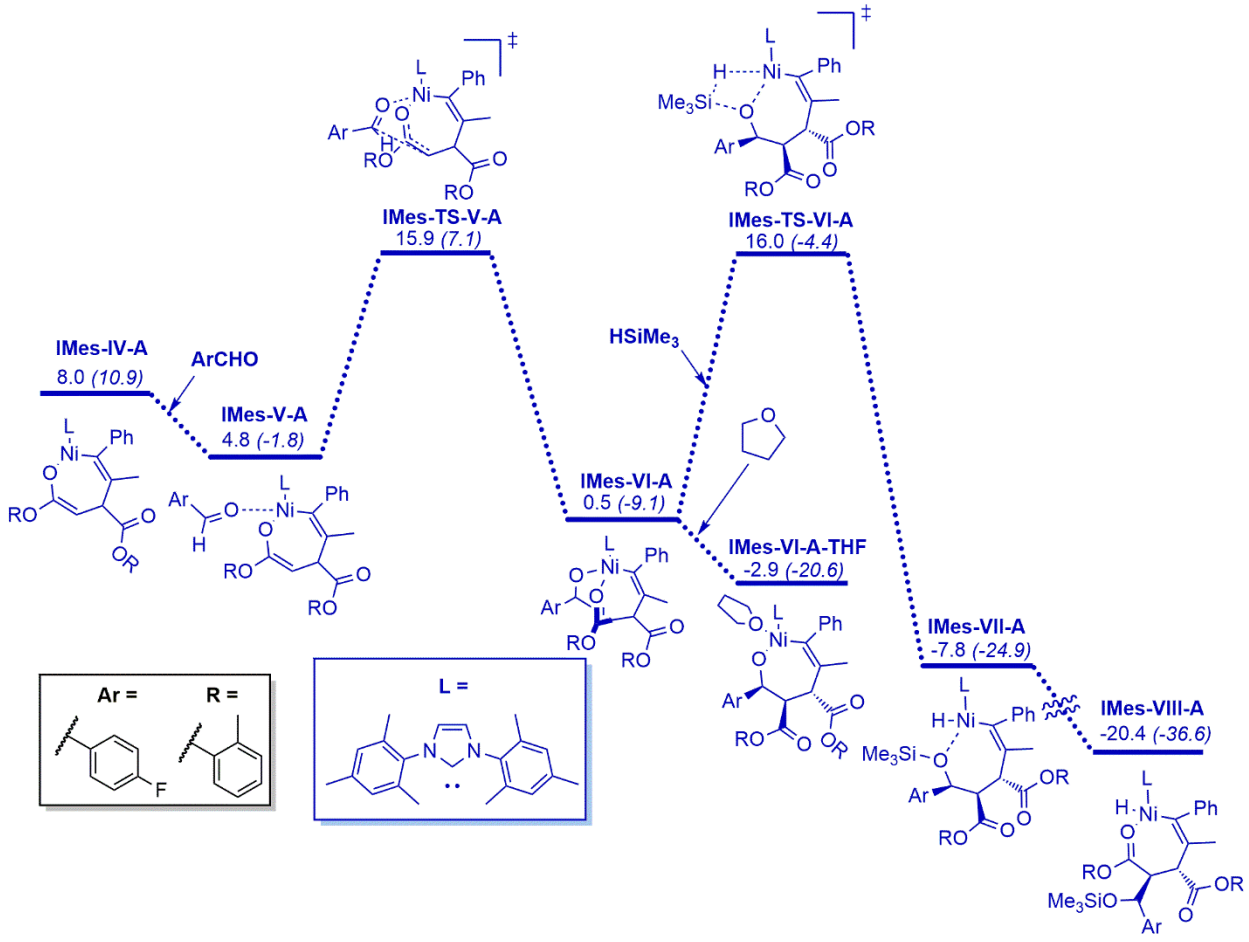

Figure 3-10. *Pathway A of the activation of IMes catalyst **3-8-A**, part 1. Energies are given in kcal/mol, with enthalpies listed in parentheses. Computational details are included in the appendix.*

In the case of catalyst **3-8-A**, path A provides a means to release a potential active catalyst. Figures 3-10 and 3-11 detail the pathway for catalyst release. Seven-membered metallacycle **IMes-IV-A** can ligate to an aldehyde (**IMes-V-A**, Figure 3-10), and can then undergo an aldol reaction (**IMes-TS-V-A**) to yield complex **IMes-VI-A**. Notably, this process has a slightly higher barrier than the isomerization process (15.9 kcal/mol), but still outcompetes ketene elimination (**IMes-TS-II-B**, 22.0 kcal/mol, Figure 3-9). After aldol addition, ligation of tetrahydrofuran to complex **IMes-VI-**

A is possible (**IMes-VI-A-THF**), but an irreversible hydrosilylation (**IMes-TS-VI-A**) can occur, yielding complex **IMes-VII-A**. Complex **IMes-VII-A** can then rearrange to nickel hydride species **IMes-VIII-A**. Subsequently, **IMes-VIII-A** could either undergo ester reduction (**IMes-TS-VIII-Z**, 7.0 kcal/mol, Figure 3-11) to form **IMes-IX-Z**, or undergo a carbocyclization event (**IMes-TS-VIII-A**, -7.8 kcal/mol). The latter process is preferred by a significant margin, and leads to nickel alkoxide species **IMes-IX-A**, which can easily extrude an alkoxide to yield compound **3-13** and an activated catalyst.

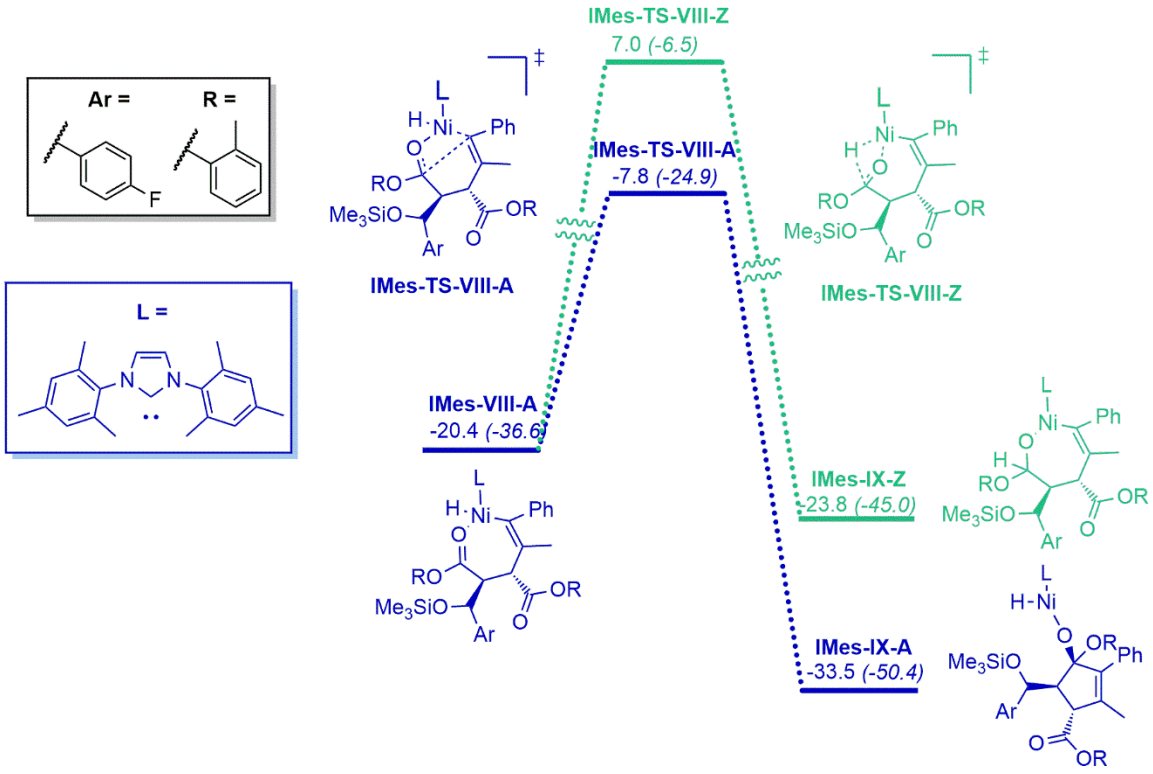

Figure 3-11. *Pathway A of the activation of IMes catalyst **3-8-A**, part 2. Path Z details the possible ester reduction reaction, and is shown in seafoam green. Energies are given in kcal/mol, with enthalpies listed in parentheses. Computational details are included in the appendix.*

While IMes catalyst **3-8-A** has been shown experimentally to be a competent catalyst in the production of **3-9** (Figure 3-3), the same cannot be said for BAC catalyst **3-10-A** (Figure 3-4). Computational investigation of path B of catalyst **3-10-A** reveals a putative reason why that might

be the case (Figure 3-12). Cyclization of ketene complex **BAC-III-B** yields carbocycle **BAC-IV-B** (Figure 3-9). Notably, the presence of a proximal ester moiety in **BAC-IV-B** allows for direct coordination of the ester to the nickel center (**BAC-V-B**, Figure 3-12). In effect, by occupying a coordination site, the proximal ester prevents the coordination of an aldehyde that is reported in Chapter 2. The stability of **BAC-V-B**, and the additional chelation that occurs in the complex, can explain why BAC catalyst **3-10-A** is ineffective.

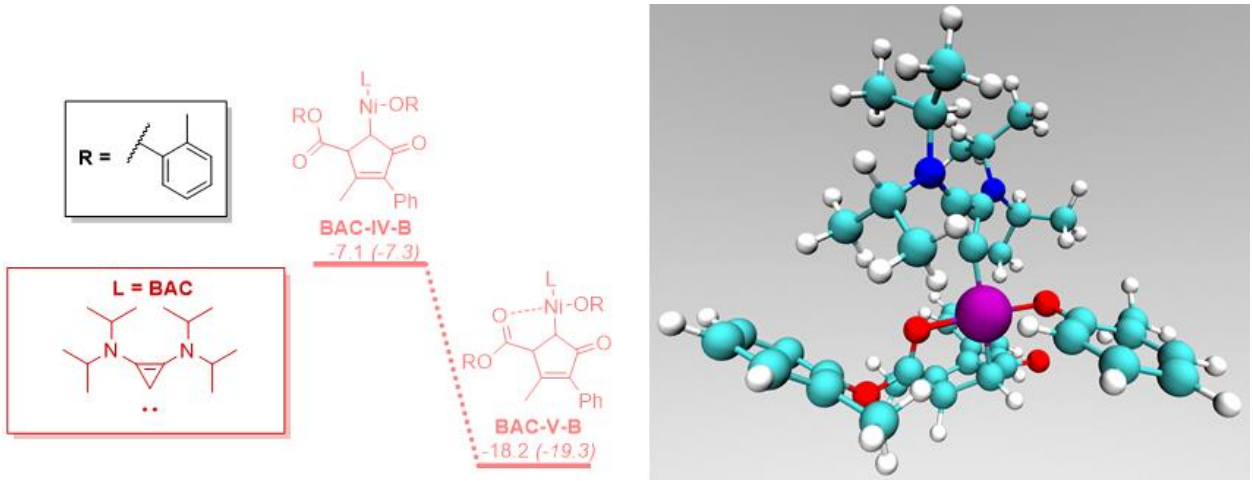

Figure 3-12. *(Left) Complex **BAC-IV-B** can rearrange into carbonyl bound complex **BAC-V-B**. (Right) A three-dimensional representation of complex **BAC-V-B**.*

3.5 Preliminary Results Towards the Development of an Air-Stable Nickel(0) BAC Catalyst

The difference in activation mechanism between BAC complex **3-10-A** and IMes complex **3-8-A** can explain why **3-8-A** is active in reductive coupling reactions, but **3-10-A** is not. With a relationship between catalyst activation mechanism and catalyst efficacy suggested, the next logical step is to develop a catalyst that goes through an "aldol-first" mechanism, so as to avoid catalyst trapping by developing a species such as **BAC-V-B** (Figure 3-12). As the fate of catalyst **3-10-A** is determined in part by the barrier of ketene elimination (**BAC-TS-II-B**, Figure 3-9) compared to isomerization (**BAC-TS-III-A**, Figure 3-9), the transition states for ketene

elimination and metallacycle isomerization were evaluated for a variety of different BAC fumarate complexes (Figure 3-13). Of the 12 fumarates tested, only 3 (**B**, **I**, **J**) were found to favor metallacycle isomerization over ketene elimination. Additionally, 3 more fumarates (**C**, **K**, **M**) had metallacycle isomerization within 1 kcal/mol of ketene elimination. In all 6 cases, the difference in energy between the two possible isomerization mechanisms is within the reported error for the functional used in the analysis, ωB97X.[13] For this reason, the 6 fumarates listed (**B**, **C**, **I**, **J**, **K**, **M**) are viable candidates for experimental study.

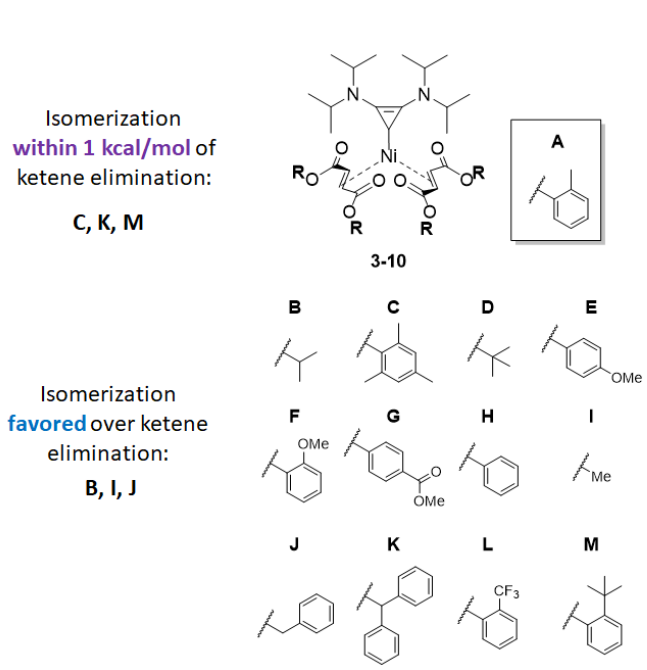

R=	Ketene Elimination	Metallacycle Isomerization	Difference
A	13.4	19.5	-6.1
B	**24.4**	**23.4**	**1**
C	**22.1**	**22.2**	**-0.1**
D	24	25.7	-1.7
E	12.7	22.5	-9.8
F	10.6	21.4	-10.8
G	12.8	20.1	-7.3
H	13.8	20.2	-6.4
I	**23.9**	**23.7**	**0.2**
J	**24.5**	**23.7**	**0.8**
K	**18.9**	**19.3**	**-0.4**
L	12.3	17.9	-5.6
M	**17.2**	**17.8**	**-0.6**

Figure 3-13. *Preliminary efforts towards developing a BAC fumarate catalyst. Fumarates that favor metallacycle isomerization over ketene elimination are shown in blue. Fumarates where metallacycle isomerization is within 1 kcal/mol or less than ketene elimination are shown in purple. Listed energies are free energies in kcal/mol, and are relative to* ***BAC-I*** *(Figure 3-9). Computational details are included in the appendix.*

The fumarate R groups where metallacycle isomerization is competitive with ketene elimination have a diverse steric and electronic profile, ranging from small substrates (**I**, **J**) to bulky substrates (**K**, **M**), and including both aryl (**C, M**) and alkyl (**B**, **I**, **J**, **K**) groups. A clearer pattern exists for the fumarates that clearly favor ketene elimination (**D**, **E**, **F**, **G**, **H**, **L**). Almost all of these fumarate

R groups are aryl species, and are generally non-bulk aryl groups. For instance, in all of the tested aryl substrates that lacked an ortho substituent (**E**, **G**, **H**), ketene elimination is favored over metallacycle isomerization by at least 6 kcal/mol.

Additionally, the competitiveness of metallacycle formation appears to be driven more by destabilizing the ketene elimination step, rather than stabilizing the isomerization process. The lowest barrier ketene elimination step (10.6 kcal/mol, **F**) is much lower in energy than the lowest barrier isomerization step (17.8 kcal/mol, **M**). This presents a problem in catalyst development, as if metallacycle isomerization needs to be fast enough to enable catalyst release. Interestingly, all of the aryl fumarates tested have lower barriers for metallacycle isomerization than any of the alkyl fumarates tested.

While the data presented here represent only a preliminary study into the factors that affect selectivity for path A over path B, some key insights into the factors that affect path selectivity can be gleaned. Alkyl groups appear to generally favor isomerization over elimination, but the barriers for both processes appear to be higher compared to aryl groups. Aryl groups, in turn, appear to generally favor elimination over isomerization, but both processes are lower in energy. Steric bulk also appears to have a positive effect in making the isomerization process more competitive than elimination, which is consistent with what was observed in Chapter 2 with α-substituted enoates. Taken together, the most promising fumarate tested in Figure **3-13** appears to be fumarate **M**. This fumarate has the lowest barrier for metallacycle isomerization among the tested set, and while ketene elimination is favored, it is only favored by an amount within the error of the calculation (0.6 kcal/mol). Future developments in creating a bulkier version of **M** may allow for the development of an air-stable Ni(0) BAC complex.

3.6 Summary, Conclusions, and Outlook

In summary, the mechanism of activation of nickel NHC fumarate complexes has been identified. The original hypothesis of ligand displacement was disproven by comparing the binding energies of the fumarate to the yield of product observed experimentally. Based on these initial computational results, a new hypothesis of fumarate consumption during catalyst activation was crafted, ultimately leading to the experimentalists identifying products of the associated fumarate consumption reaction. The isolation of fumarate consumption species **3-12** and **3-13** determined that catalyst activation occurs through a reaction analogous to the three-component coupling reaction detailed in Chapter 2. Using the three-component coupling as a guide, catalyst activation through both an aldol-first and ketene-first pathway was examined computationally. It was found that active IMes catalyst **3-8-A** undergoes an aldol-first catalyst activation mechanism, but inactive BAC catalyst **3-10-A** undergoes a ketene-first activation mechanism, where it becomes trapped as ester-bound complex **BAC-V-B**. Preliminary work has been done to find a fumarate that can be paired with BAC that would ensure that the BAC catalyst is activated through an aldol-first mechanism, and avoid catalyst trapping.

Chapter 4: Synergistic Effects Between Radical Attack and Applied Force in the Depolymerization of Poly(Acrylic Acid)

4.1 The Potential Energy Surface Under Applied Force

Chemists have used tools such as photoexcitation, applied electric potentials, or simply the manipulation of temperature to alter the kinetics and thermodynamics of chemical reactions. The application of an external mechanical force represents another avenue to introduce energy into a chemical system.[86] Through the introduction of a force bias, chemical reactions that are endergonic, or are too high in barrier to proceed at a reasonable rate, become accessible to chemists.

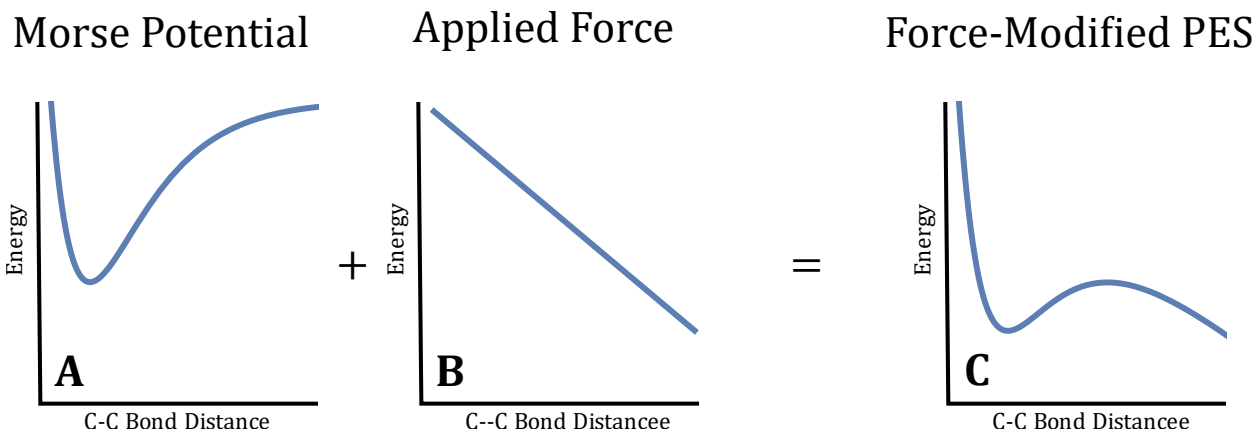

Figure 4-1. *The additive effect of applied force on the Morse potential. The distortion due to applied force is greater at larger C-C bond distances.*

Bond scission events are a classic example of how an applied mechanical force can change the nature of chemical reaction. A carbon-carbon (C-C) bond has a homolytic bond dissociation energy of approximately 90 kcal/mol,[87] and due to this high endothermicity, C-C bond scission is

not expected to occur spontaneously. However, if an external force is applied, the energy of a chemical system decreases as the two carbons move further and further apart. This means that eventually, at a large enough distance, C-C bond scission becomes exothermic, and thermodynamically favorable. Figure 4-1 details the effect that applied force has on a potential energy surface. If we consider the C-C bond as adopting a Morse potential (A), we can then combine that potential with an external force (B) to create a force-modified potential (C). In potential C, bond scission is exothermic, but there a barrier associated with the bond scission event, that is dependent on the amount of force required.

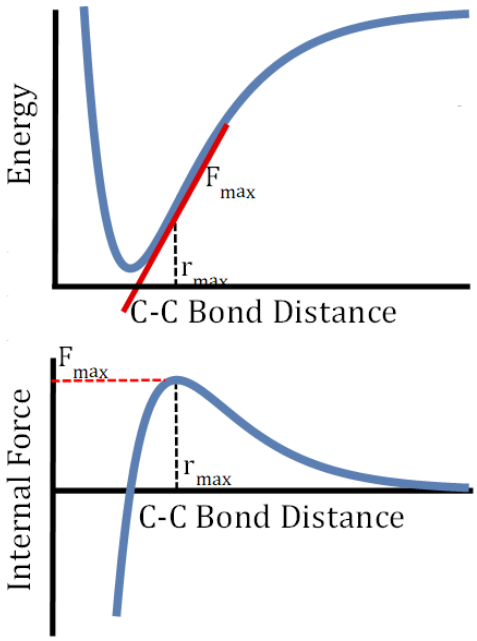

r_0 = Equilibrium bond length

E_0 = Bond dissociation energy

k = Bond force constant

$$a = \sqrt{\frac{k}{2E_0}}$$

Morse Potential: $E = E_0 e^{-2a(r-r_0)} - 2E_0 e^{-a(r-r_0)}$

$$F = \frac{\partial E}{\partial r} = -2aE_0 e^{-2a(r-r_0)} + 2aE_0 e^{-a(r-r_0)}$$

At the maximum force value F_{max}, $r = r_{max}$ and $\frac{\partial F}{\partial r} = 0$

$$r_{max} = \frac{ar_0 + \ln(2)}{a}$$

$$\frac{\partial F}{\partial r} = 0 = 4a^2 E_0 e^{-2a(r_{max}-r_0)} - 2a^2 E_0 e^{-a(r_{max}-r_0)}$$

$$F_{max} = -2aE_0 e^{-2a(r_{max}-r_0)} + 2aE_0 e^{-a(r_{max}-r_0)}$$

$$F_T = F_{max} = \sqrt{\frac{E_0 k}{8}}$$

Figure 4-2. *Estimating the tensile of a C-C bond using the Morse method.*

Considering a chemical bond as a Morse oscillator has the additional advantage of allowing for an estimation of the tensile strength of the bond (F_T, the force required to break the bond). The first derivative of the Morse potential is the force that the potential exerts on the chemical bond (internal

force). Applying an external force, then, can be seen as counteracting the internal forces of the bond. If it is assumed that a bond breaks when the no barrier for scission exists, it can then be inferred that the tensile strength of a bond is simply the maximum of the first derivative of the Morse potential. Using the functional form of the Morse potential, the tensile strength can be derived, yielding a dependence only on the bond dissociation energy (E_0), and bond force constant (k) (Figure 4-2).[88]

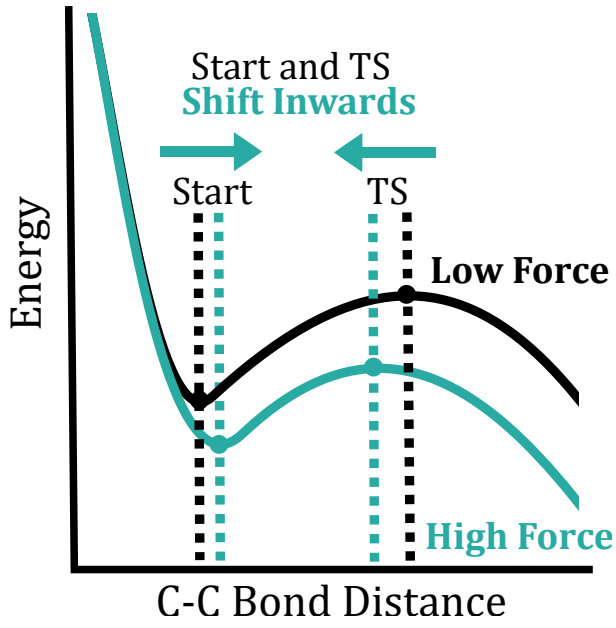

Figure 4-3. *The expected effects of force according to the tilted potential energy surface model.*

Of course, in reality, bond scission events can occur even if a kinetic barrier exists. Preliminary work by Zhurkov has shown that applied force has a linear effect on such a kinetic barrier, enabling a low barrier for reaction (and thus faster rate of reaction) with an increase in applied force.[89] Force is also expected to change the geometries of the intermediates involved. This is adequately described by the tilted potential energy surface model (TPES) (Figure 4-3). In general, with increasing external force, it is expected that the starting geometry (Start) of the material becomes more product-like with increasing force, and the transition state (TS) becomes more reactant-like.

The net effect of this process is that the starting structure and the transition state become more similar with increasing applied force.

Computational methods offer an avenue to investigate mechanochemical processes.[90,91] A common method of computational investigation is the COGEF (constrained geometries simulate external force) method. In COGEF, the potential energy surface of stretching a molecule is mapped using a series of geometry optimizations with an increasing distance constraint. In the seminal paper of the method, Beyer uses the information derived from this potential map to estimate the tensile strengths of various bonds, including C-C, C-N, and Si-O at various timescales.[92] Notably, the method cannot identify the transition state of the bond scission event, as it infers activation energies from a theoretical force-modified potential that is based off of the curvature of the potential energy surface under no force (similar to the Morse model described in Figure 4-2). Despite this limitation, COGEF still finds use in exploring mechanochemical processes; for instance, in comparing the COGEF potential of unprotonated vs protonated dimethyl ether, Beyer finds that proton affinity of an ether increases with applied force,[93] supporting a previous Carr-Parinello dynamics study that demonstrated the role of aqueous solvation in the depolymerization of poly(ethylene glycol).[94] In complicated systems such as lignin, ab initio steered molecular dynamics (AISMD) have been used to identify the bonds most susceptible to scission during depolymerization.[90] AISMD has also been used to identify the heterolytic character of poly(*o*-phthalaldehyde) depolymerization.[95]

While popular tools such as COGEF are unable to provide a transition-state geometry,[92] recent developments in the growing string method allow for the identification of transition states in the presence of an applied force (F-GSM).[96] In this chapter, F-GSM is the method of choice for interrogating bond scission events, allowing for detailed analysis on the transition state geometries

of the processes. The tool works in a similar fashion to GSM (see Section 1.5), with the addition that the energy of a given state is modified by the term $-F * \Delta x$, where F is the applied force, and Δx is the change in distance between the atoms upon which force is applied.

4.2 Plastic Recycling Using Ultrasonic Depolymerization

Plastic waste accumulation in the environment occurs on a massive scale, where it is predicted that the mass of plastics in the ocean will exceed the total biomass of fish by the year 2050.[97] This problem might be somewhat alleviated by recycling, but the United States only recycles roughly 9.1% of plastic waste, a low figure compared to recycling rates for paper (66.6%), glass (26.4%), and metals (34.3%).[98] The recycling rate of plastics is limited[99] by methods that mechanically repurpose certain plastics for new applications, usually resulting in lower quality materials which reduces economic incentives to recycle. For this reason, chemical methods of recycling such as depolymerization attract interest due to their potential to reach a greater scope of materials and create more valuable recycled products. By developing and expanding recycling technologies such as depolymerization, the recycling rate for plastics could be greatly improved, ultimately having a great positive impact on the environment.

A promising depolymerization strategy is to use the mechanochemical technique of ultrasonic irradiation. (Figure 4-4, A).[100] In ultrasonic depolymerization, an acoustic field with frequencies of greater than ~20 kHz is applied to a solution of polymer.[88,91,101–105] The pressure variations imparted by the high frequency sound waves form cavitation bubbles in solution that ultimately collapse (Figure 4-4, B), producing a shear force that is capable of tearing polymer chains apart (Figure 4-4, C). Additionally, pyrolytic reactions in the cavitation bubbles are known to produce free radicals (Figure 4-4, D). These radicals are believed to accelerate the process of polymer

degradation,[106] as introduction of an external radical source has been shown to increase the breakdown rate.[107–114]

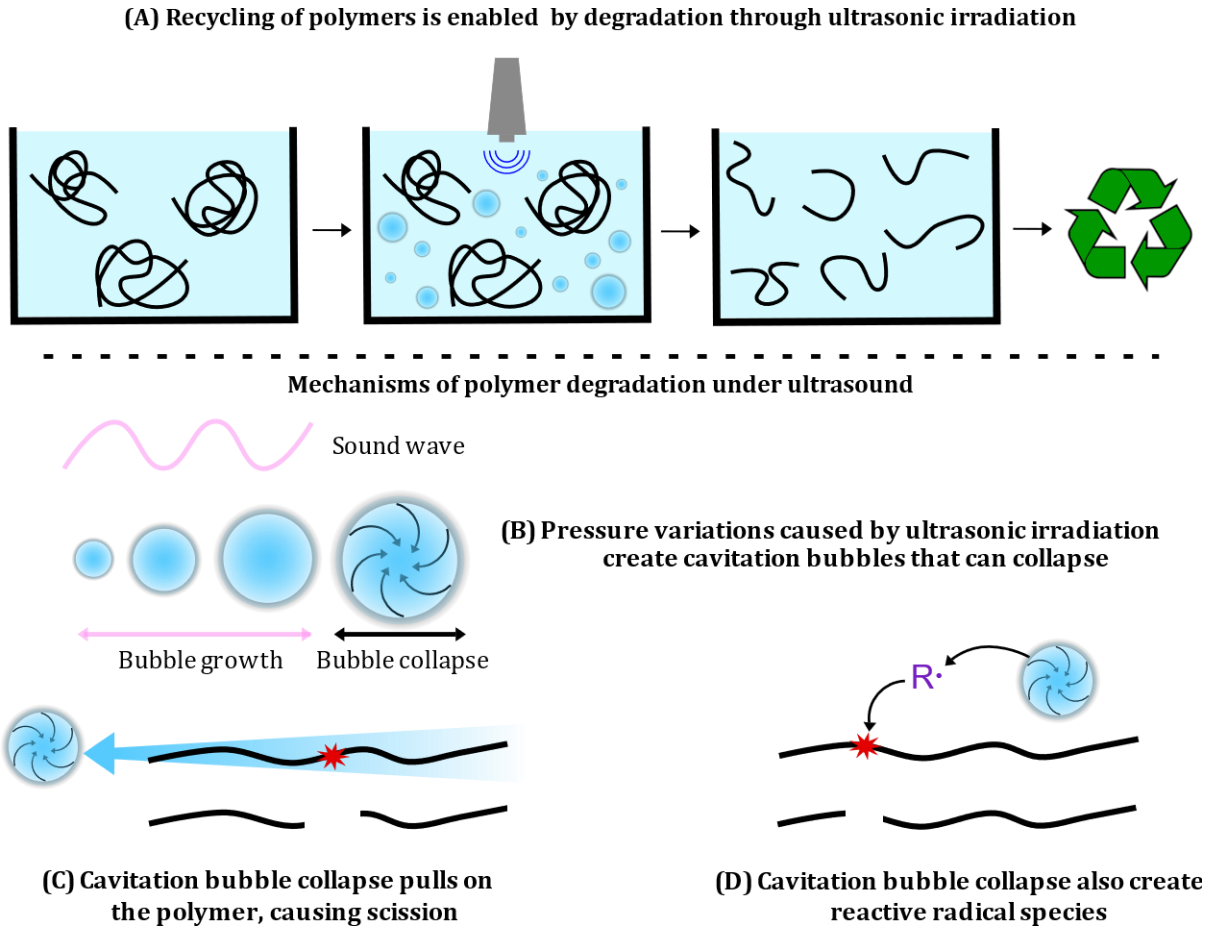

Figure 4-4. *Recycling of polymers is enabled by ultrasonic depolymerization.*

Prior studies have considered the roles of mechanical force and radical species—each separately—in the process of ultrasonic irradiation. Based on studies with degassed solvent,[115] and the observed propensity for midpoint scission to occur,[116] the mechanical forces generated though cavitation bubble collapse are thought to be the dominant source of bond scission.[88,90,101] Mechanical scission generally occurs through a homolytic pathway,[88,101,102] resulting in the formation of two free macroradicals. These homolytic cleavage events have been observed by monitoring the

stoichiometric consumption of a radical trap.[117] Macroradicals have also been directly observed through EPR studies during the sonication process.[118]

As a consequence of the depolymerization mechanism largely being mechanical scission, depolymerization is expected to occur until the molecular weight of the polymer converges to a limiting value. The origin of this effect is best explained by a model developed by Okkuama and Hirose.[119] In their model, the force that a polymer experiences is due to the friction of the monomer units with the surrounding solvent. Consequently, the overall force that a given polymer strand feels is proportional to the number of monomers in a given strand. While the force experienced by each polymer strand shrinks as the strand gets shorter, the tensile strength of the polymer remains constant. The limiting length of a given polymer, then, is simply the length at which the forces experienced by the polymer strand are insufficient to cause further chain scission. Simon has used this model to accurately simulate the time evolution of polymer degradation.[120]

Separate from the formation of polymer macroradicals during ultrasonic polymerization, small radical species are also known to form during the cavitation process.[121] As cavitation bubbles grow, the frequency of their vibration increases, heating the interior of the bubble to several thousand degrees Kelvin. At such high temperatures, volatile compounds in the bubble, such as solvent molecules, can pyrolytically disproportionate to small radicals. These radicals are known to escape from the cavitation bubble and enter solution, where they can react with dissolved materials.[122–125] The free radicals that are generated are also known to initiate radical polymerization in solutions of monomer.[126]

Quenching studies have shown that free radicals can play a role in the depolymerization process as well. Koda[106] has shown that the addition of radical scavenger tert-butanol inhibits the ultrasonic degradation of various polymers. Likewise, the introduction of radical-generating species is known

to accelerate ultrasonic degradation processes. The Chen group, as well as others, have reported depolymerization processes that combine Fenton chemistry with ultrasound.[107–111] Yao has reported a synergistic effect of bubbling ozone during the ultrasonic irradiation of chitosan solutions.[113] Gogate has shown that addition of oxidant potassium persulfate is beneficial in the degradation of guar gum using hydrodynamic cavitation.[112] This group also found that addition of H_2O_2 or ozone aids in the ultrasonic depolymerization of poly(acrylic acid).[114]

The interplay between radical and ultrasonic degradation plays an important role in breaking down polymers, but the specific mechanism(s) involved in this synergy is not fully explicated. Koda,[106] for instance, proposes random chain scission events as an explanation for why free radicals affect ultrasonic polymer degradation. In Koda's report, however, it was also observed that the limiting molecular weights of the degraded polymers change in the presence or absence of a radical scavenger. The implication of this observation is that in the presence of radicals, there is a change in how the polymer responds to mechanical force, as the limiting length effect is due exclusively to mechanochemical degradation. Based on this implication, it appears that the radical species formed during ultrasonic degradation play a role beyond that of enabling simple random chain scission events.

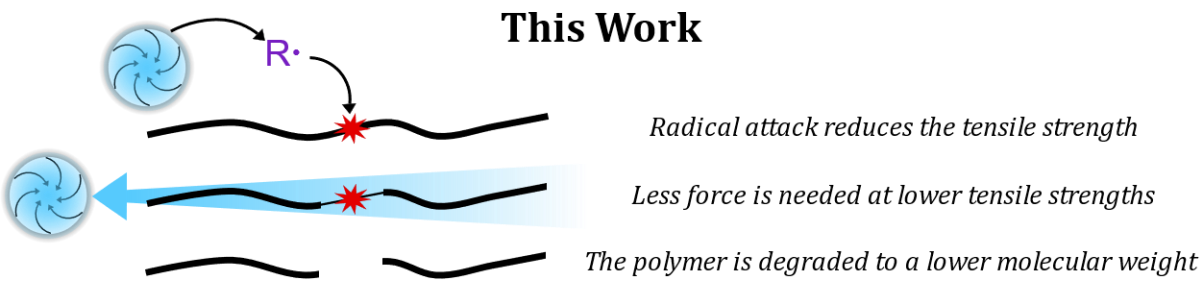

Figure 4-5. *This chapter explores the synergistic interplay between radical attack and tensile force.*

This chapter seeks to provide a clear, atomistic picture of how radical species affect the sonochemical depolymerization process (Figure 4-5). The synergistic effect of radical attack and

tensile force in the ultrasonic depolymerization of poly(acrylic acid) (PAA) will be described. PAA was chosen as it is broadly used as a super-absorbent polymer, as well as in paints, dentistry, and other applications.[114] The origin of the change in limiting length observed during depolymerization can be explained though the interplay of radical attack and application of mechanical force. Radical attack will be shown to have a weakening effect on the tensile strength of the polymer, which will affect the limiting length. The effects of force on the transition state energy of bond scission will be quantified, allowing for the inclusion of thermal effects. Finally, it will be shown that radical attack causes the polymer to respond to force in a manner distinct from what is normally seen in mechanochemistry.

4.3 Evaluating the Impact of the Weak Bond Effect Using a Morse Potential

Incorporation of a weak bond into a polymer backbone is expected to accelerate the rate of chain scission.[91] For example, when Encina and coworkers added peroxide linkages in poly(vinylpyrrolidone), the rate of ultrasonic degradation increased by a factor of 10.[127] Using diazo-linked polymers, Moore and coworkers provided evidence that cleavage is mostly localized at weak bonds.[128] This "weak bond effect" suggests that radical activation of PAA might synergize with tensile force to break down this polymer. While the homolytic bond dissociation energy of a carbon-carbon bond is generally in the vicinity of 90 kcal/mol,[87] the heat of (radical) polymerization for polyolefins is much lower, in the range of 10-30 kcal/mol.[129] Acrylate polymerizations are in the vicinity of 19 kcal/mol,[129] suggesting that lower forces will break the weakened C-C bond in activated PAA.

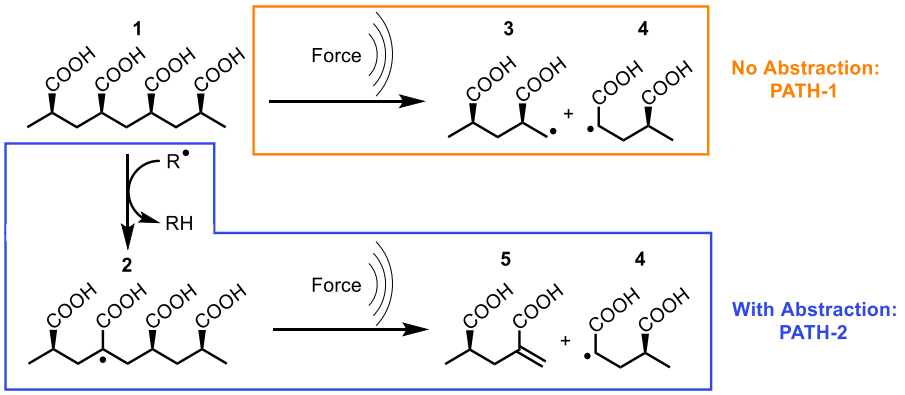

Figure 4-6. *Model systems used in this study: Degradation of PAA through force alone (**PATH-1**), and force in conjunction with radical attack (**PATH-2**).*

Two model systems of PAA were used to quantify the bond-weakening effect of radicals (Figure 4-6). The first is a tetramer of AA with inactivated C-C bonds (**1**), which can be fragmented via tensile force into a biradical (**3**+**4**). This degradation pathway is called **PATH-1**. The second (**2**) is similar to **1**, except one hydrogen atom from the backbone has been removed, for example by radical abstraction via a sonication-generated hydroxyl. C-C bond breaking for the radical-activated species is denoted **PATH-2**.

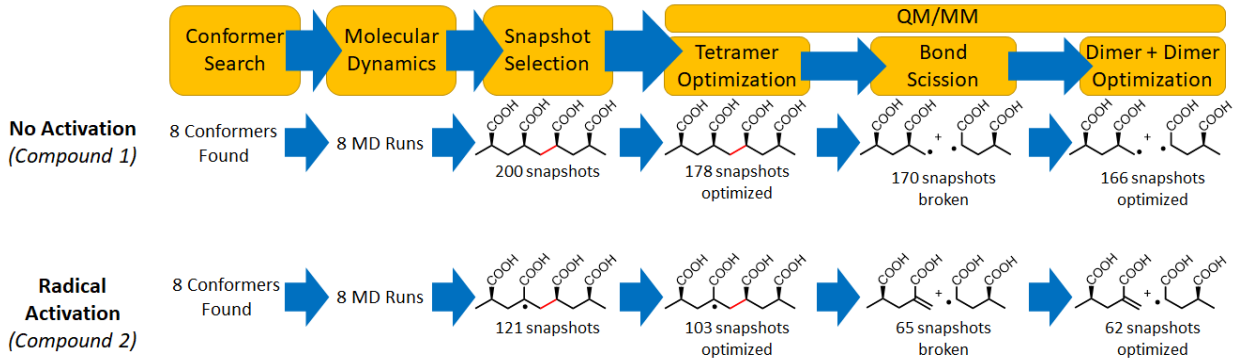

Figure 4-7. *Flowchart for evaluating tensile strength using the Morse method. The complete procedure is described in the appendix.*

These pathways were first examined by treating the polymer scission as a purely mechanical event using the Morse method. A flowchart detailing this process is shown in Figure 4-7. A library of conformations of **1** and **2** were first generated. Conformers of **1** were generated using the Confab

tool[130] in Open Babel,[131] which resulted in 8 unique conformers. Conformers for **2** were generated by abstracting an α-hydrogen from each of the conformers of **1**. As hydrogen bonding is known to affect the heat of polymerization of protic polymers such as PAA,[132] and to ensure that the conformers used in this study are consistent with aqueous solvation, explicit water solvation was modeled. For each conformer of **1** and **2**, the system was surrounded by a 6 Å water shell containing 260 water molecules. Molecular dynamics (MD) simulations were then used to create a series of snapshots of the tetramer in an aqueous environment.

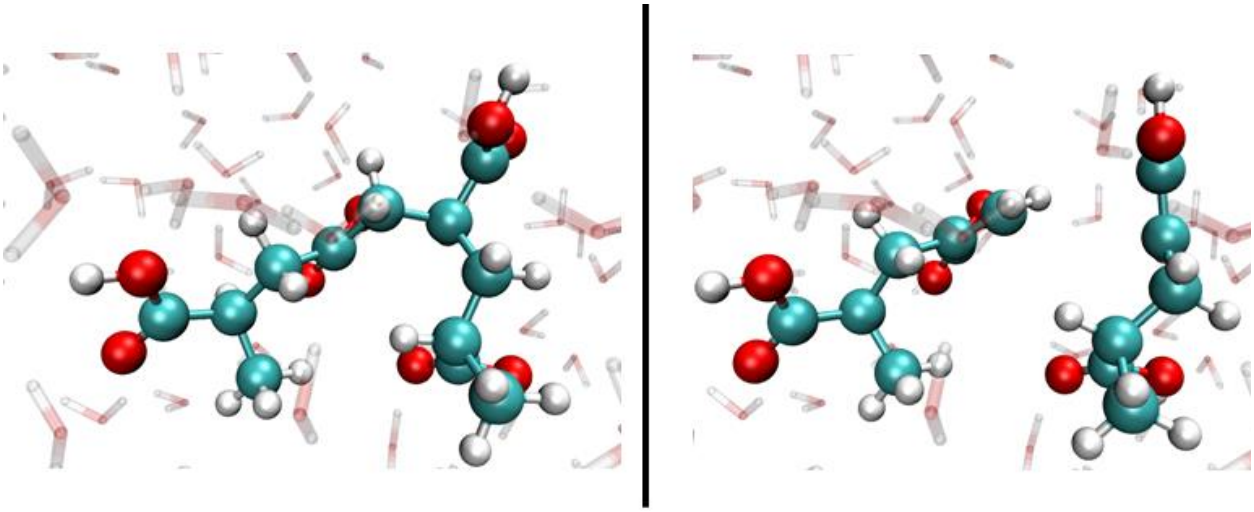

Figure 4-8. *Example three-dimensional representations of the tetramer (Right) and dimer+dimer (Left) systems used for this study. These represent two of many snapshots used for this study.*

The geometry of selected snapshots was then re-optimized using a non-periodic quantum mechanical/molecular mechanical (QM/MM) method. After optimizing the geometry of the snapshots (Figure 4-8, Left) the scissile bond (shown in red, Figure 4-7) was cleaved by applying a stretching force of 10 nN between the two atoms of the scissile bond using the EFEI (external force explicitly included) method.[133] After bond scission, subsequent re-optimization yielded two

PAA dimers (referred to as dimer+dimer snapshots, seen in Figure 4-8, Right). A complete description of the entire procedure can be found in the appendix.

As denoted in Figure 4-2, the tensile strength of a bond can be determined from its bond dissociation energy (E_0) and the bond's force constant (k). The bond dissociation energy was determined by comparing the total energy of each dimer+dimer snapshot to the tetramer from which it came. By averaging the difference in energy for each set of snapshots, a value for the enthalpy of bond scission is obtained. To determine the force constant of the scissile bond, a vibrational constant was determined from each optimized tetramer absent any explicit water using partial hessian vibrational analysis.[134] The calculated force constant values were averaged to yield the force constant of the scissile bond.

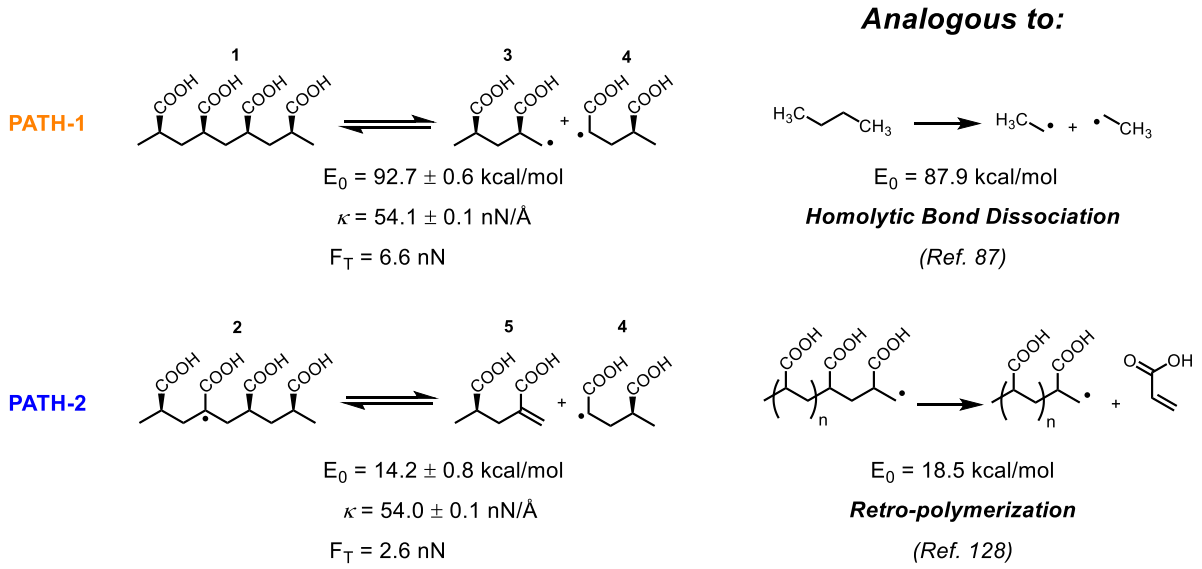

Figure 4-9. *The effect of hydrogen atom abstraction on the tensile strength poly(acrylic acid). Computational details are included in the appendix.*

These values were used in the final equation for tensile strength (F_T) (Figure 4-2). The tensile strengths of **1** and **2** were calculated as 6.6 nN and 2.6 nN, respectively (Figure 4-9), both within the range of forces available for sonication.[88] Hydrogen atom abstraction, therefore, is calculated

to reduce the tensile strength of PAA by approximately 4 nN. As the limiting length of polymer during sonication is proportional to the square root of the polymer's tensile strength,[119] the results in Figure 4-9 predict that the limiting length of a polymer weakened by radicals should be ~37% lower than a polymer free of radical defects. These results are on the order of the changes in limiting length observed by Koda upon suppression of radical formation during the sonication of poly(ethylene oxide) and polysaccharides.[106]

The predicted tensile strength of **1** of 6.6 nN using the simple Morse method is outside the range of modern estimates of C-C bond strength, such as the thermally activation barrier to scission (5-6 nN),[135] or COGEF (4.5-5 nN) models. This discrepancy likely stems from the assumption that scission only occurs in the absence of a thermal barrier.[92] In reality, it is expected that bond scission would occur once a thermally accessible barrier is attained. Analysis of the bond scission reaction using F-GSM will identify the nature of this barrier, and allow for a more accurate determination of the effect of radical abstraction on the transition state of bond scission and tensile strength.

4.4 Determining the Effect of Radical Abstraction on the Transition State of Bond Scission

Polymer degradation by sonication is better described by treating cleavage events as a chemical reaction. Using this model, the reactant and transition state geometries—as well as the activation barrier—depend on the amount of force applied to the polymer chain. Using the sets of tetramers from the previous section, the transition states of bond scission for **PATH-1** and **PATH-2** were found using the force-biased growing string method (F-GSM, see appendix for the full process)

for a range of applied tensile forces.[96] The activation enthalpies as a function of force from F-GSM are given in Figure 4-10.

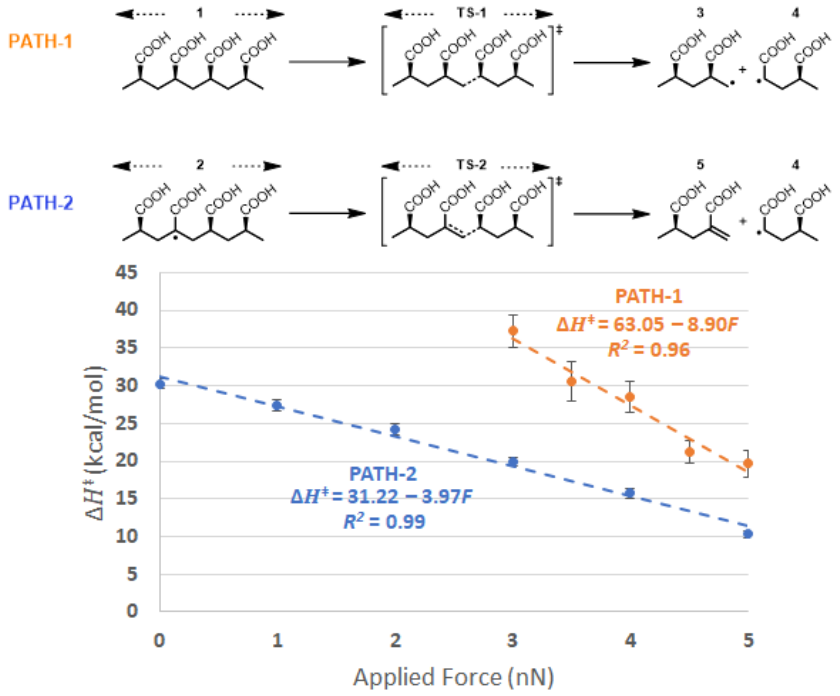

Figure 4-10. *The relationship between enthalpy of activation and applied force on the polymer chain. Computational details are included in the appendix.*

Given that hydrogen atom abstraction by a hydroxyl radical is fast ($\Delta H^{\ddagger}$ of ~3 kcal/mol) and irreversible,[136] the selectivity between **PATH-1** and **PATH-2** is expected to be largely determined by the availability of hydroxyl radicals in solution. However, the rate of bond scission for **PATH-1** and **PATH-2** will still be relevant if hydrogen atom abstraction occurs, as the relative rate between **PATH-1** and **PATH-2** will determine whether scission will occur at the point of hydrogen atom abstraction. Essentially, hydrogen atom abstraction can only possibly be beneficial if it provides a lower barrier pathway for bond scission to occur.

At low levels of applied force, it is expected that the barrier for bond scission in **PATH-1** would be insurmountably high. For this reason, only the activation energies for forces in the range of 3 to 5 nN are shown for **PATH-1**. A negative linear relationship between the enthalpy of **TS-1** ($\boldsymbol{\Delta H^{\ddagger}}$)

is observed (R^2 = 0.96), consistent with the Bell model of force-activated chemistry.[102] Similarly to **TS-1**, the activation enthalpies of **TS-2** decrease linearly with applied force (R^2 = 0.99), but slope of only about one-half that of **TS-1**. Based on this difference in slopes, we can extrapolate that at forces greater than 6.45 nN, bond scission is expected occur via **PATH-1** over **PATH-2**.

4.5 Determining the Effective Tensile Strength of PAA With and Without Radical Attack

In bulk materials, the tensile strength of a material is defined as the maximum tension that a material can withstand before breaking. However, in looking at a single polymer strand, and considering the thermochemistry of bond scission, bond scission becomes inevitable as long as it is exergonic. A more informative measure of mechanical strength in bonds is describing the half-life of the scission process at a given force and temperature. Thus, we define the effective tensile strength $\boldsymbol{(E)F_T}$, as the amount of force needed to lower the half-life to small enough time that bond scission would be expected to occur. Notably, $\boldsymbol{(E)F_T}$ is a context-dependent quantity. For instance, applications that occur at longer timescales would need a lower force for bond scission to occur, as longer half-lives could be useful for that application.

For the purposes of this work, we are most concerned with timescales and temperatures that are relevant during ultrasonic depolymerization. Bubble collapse has been previously modeled as occurring within a 1 μs timescale.[137] While acoustic bubbles are known to form local hot spots,[138] we will focus on the temperature of the bulk solution, and assume a room-temperature reaction. Local hot-spots are known to reach up to 2,000K, and it would be expected that both **1** and **2** would break apart instantaneously under those conditions. Additionally, while the enthalpy of polymerization of PAA is known to be 18.5 kcal/mol,[139] the ceiling temperature of polymerization has not been directly measured. However, based on high-pressure polymerizations of acrylic acid, it is estimated that the ceiling temperature is somewhere around 200°C.[140]

The half-life of a reaction is given by: $t_{\frac{1}{2}} = \frac{\ln(2)}{k}$ $\quad k = \frac{k_b T}{h} e^{\frac{-\Delta G^{\ddagger}}{RT}}$

Rearrange to get $\Delta G^{\ddagger}$ needed for a given reaction half-life: $\Delta G^{\ddagger} = RTln\left(\frac{t_{\frac{1}{2}} k_b T}{h\ln(2)}\right)$

Assume that $\Delta S^{\ddagger} = \Delta S_{polym}$: $\Delta H^{\ddagger} = \Delta G^{\ddagger} + T\Delta S_{polym}$

ΔS_{polym} can be obtained from the Dainton-Ivan equation (using an extrapolated T_c value): $\Delta S_{polm} = \frac{\Delta H_{polym}}{T_c}$

Relationship between $\Delta H^{\ddagger}$ and a given half-life

$$\Delta H^{\ddagger} = RTln\left(\frac{t_{\frac{1}{2}} k_b T}{h\ln(2)}\right) + \frac{T}{T_c}\Delta H_{polym}$$

Figure 4-11. *Derivation of a relationship between enthalpy of activation ($\Delta H^{\ddagger}$) and reaction half-life ($t_{1/2}$). Where: k_b is Boltzmann's constant, T is the reaction temperature, h is Planck's constant, R is the gas constant, $\Delta H^{\ddagger}$ and $\Delta S^{\ddagger}$ are the enthalpy and entropy of activation, ΔH_{polym} and ΔS_{polym} are the enthalpy and entropy of polymerization, and T_c is the ceiling temperature of polymerization.*

Entry	$t_{1/2}$ in μs	T in °C	T_c in °C	$\Delta H^{\ddagger}$ in kcal/mol	$(E)F_T$ of **1** in nN	$(E)F_T$ of **2** in nN	$\frac{LL_1}{LL_2}$
1	1	25	200	21.1	4.7	2.5	1.37
2	**0.1**	25	200	19.8	4.9	2.9	1.30
3	1	**100**	200	26.6	4.1	1.1	1.93
4	1	25	**300**	19.1	4.9	3.0	1.28
5	**0.1**	**100**	200	24.9	4.3	1.6	1.63

Table 4-1. *The effective tensile strength of **1** and **2** calculated under different assumptions.*

Using these 3 assumptions, in conjunction with an equation relating $\Delta H^{\ddagger}$ to a given half-life (derived in Figure 4-11) and the relationship between force and TS energy in Figure 4-10, the effective tensile strength of **1** and **2** can be estimated (Table 4-1, entry 1). How the calculated tensile strength is expected to change by changing these assumptions is shown in entries 2-5. In general, the estimated values of $(E)F_T$ are lower than those predicted by the Morse model. Changes in the timescale assumption have a logarithmic effect (Entry 2), but changes in temperature have

a dramatic effect on the tensile strength of the material (Entries 3, 5). Changes in the assumption of the ceiling temperature of PAA appear to have a relatively small effect (Entry 4).

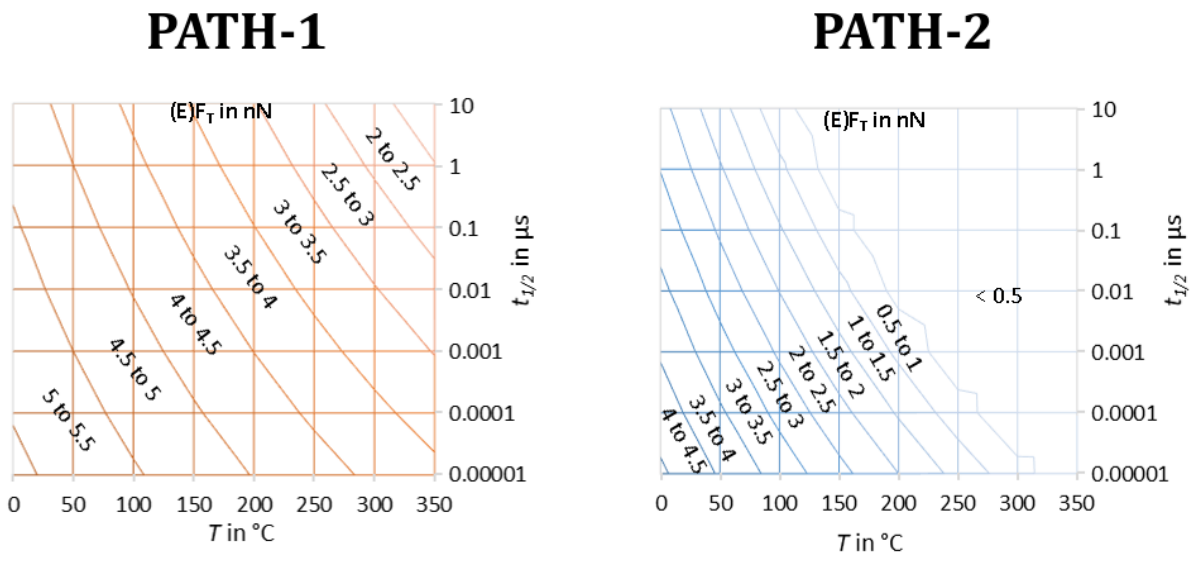

Figure 4-12. *A contour plot of the effective tensile strength (E)F_T of* ***1*** *and* ***2*** *assuming a T_c value of 200 °C.*

Based off of the relationship between tensile strength and limiting length derived by Okkuama and Hirose,[119] the expected ratio of limiting lengths should be equivalent to the square root of their ratio of tensile strengths. Using the assumptions in Table 4-1, entry 1), it is estimated that sonication of PAA in the absence of radicals (**PATH-1**) should result in a limiting length (*LL*) that is 1.37 times the length of what would be expected to be observed in the presence of radicals (**PATH-2**). This ratio is affected by the assumptions made, and the details on how the ratio of limiting lengths can change is also shown in Table 4-1.

A contour plot of effective tensile strength at various temperatures and timescales is shown in Figure 8. This plot allows for extrapolation of the effective tensile strength of **1** and **2** at temperatures and timescales beyond the assumptions made in Table 4-1. The effective tensile strength of **2** is expected to weaken to 0 nN at about 200 °C on a reaction timescale of 0.1 µs, and at temperatures higher than 400 °C, is expected to have no appreciable tensile strength on a

timescale of 10 ps. This is in contrast with **1**, which still requires some amount of force for scission to occur within 10 μs at all temperatures calculated.

4.6 Geometric Distortions Due to Applied Force on the Reactant and Transition State

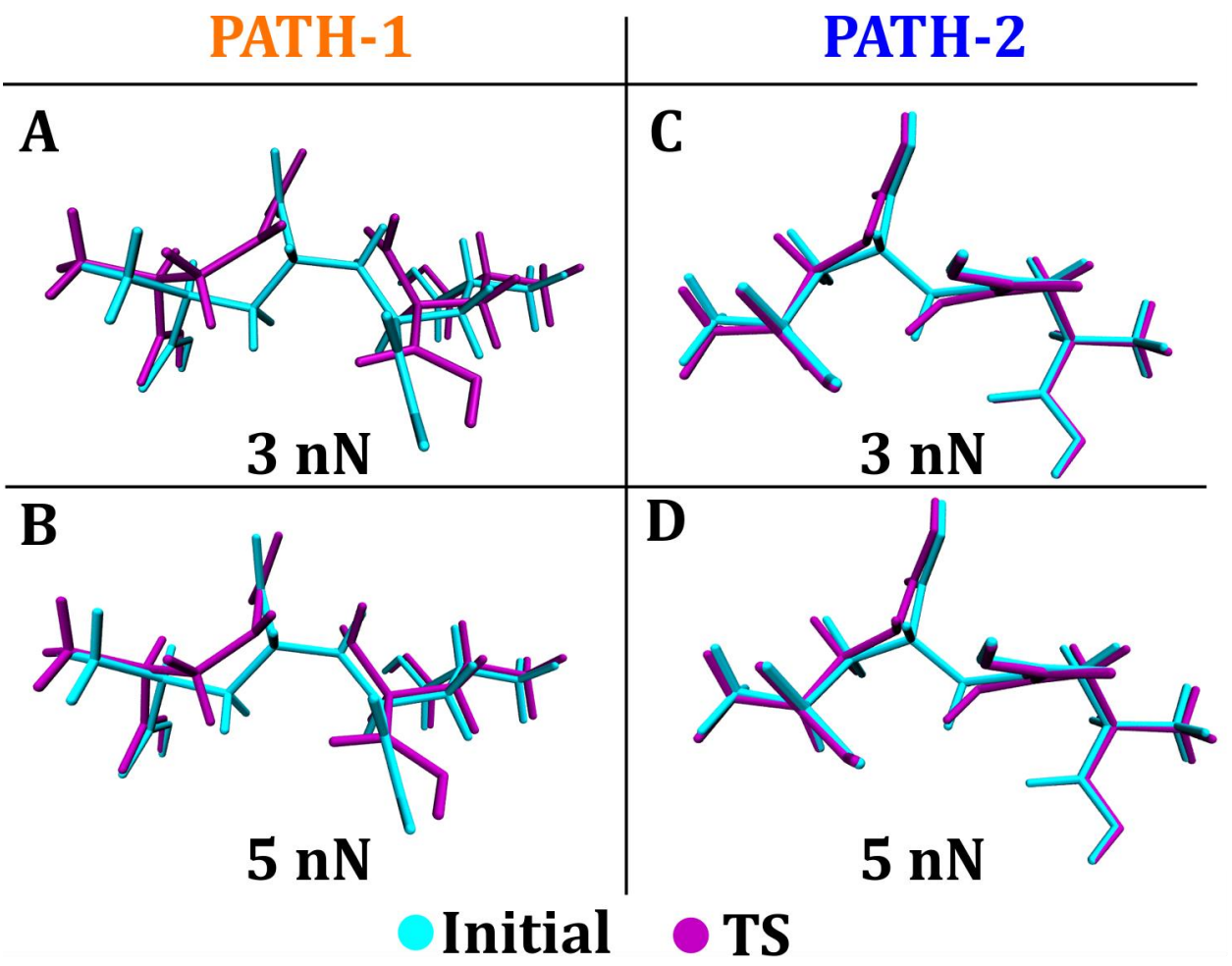

Figure 4-13. *Comparison of key geometries, which suggest that* ***PATH-1*** *initial and TS structures converge towards one another as forces increase, but* ***PATH-2*** *structures do not. Explicit water molecules are removed for clarity.*

The large difference in activation energy slope between **PATH-1** and **PATH-2** is surprising, given that the two reactions occur with similar polymer backbones (Figure 4-10). This phenomenon might be explained by the geometric distortions imposed upon the reactant and transition states for the two pathways. Figure 4-13 details the change in geometry from starting structure to transition state for selected snapshots at 3 and 5 nN of applied force. From examination of **PATH-1**, it is

clear that **TS-1** becomes more similar to **1** at 5 nN, compared to at 3 nN (Figure 4-13, A and B). In particular, this is driven by the fact that at 5 nN, the scissile bond distance of **TS-1** is shorter, and the end-to-end bond length of **1** is longer. This represents a stark difference to the changes in **PATH-2** from 3 nN to 5 nN. Comparing **2** with **TS-2** at 3 and 5 nN (Figure 4-13, C and D), the two structures track each other closely as the applied force changes, due elongation of the reactant and TS (transition state) at about the same rate.

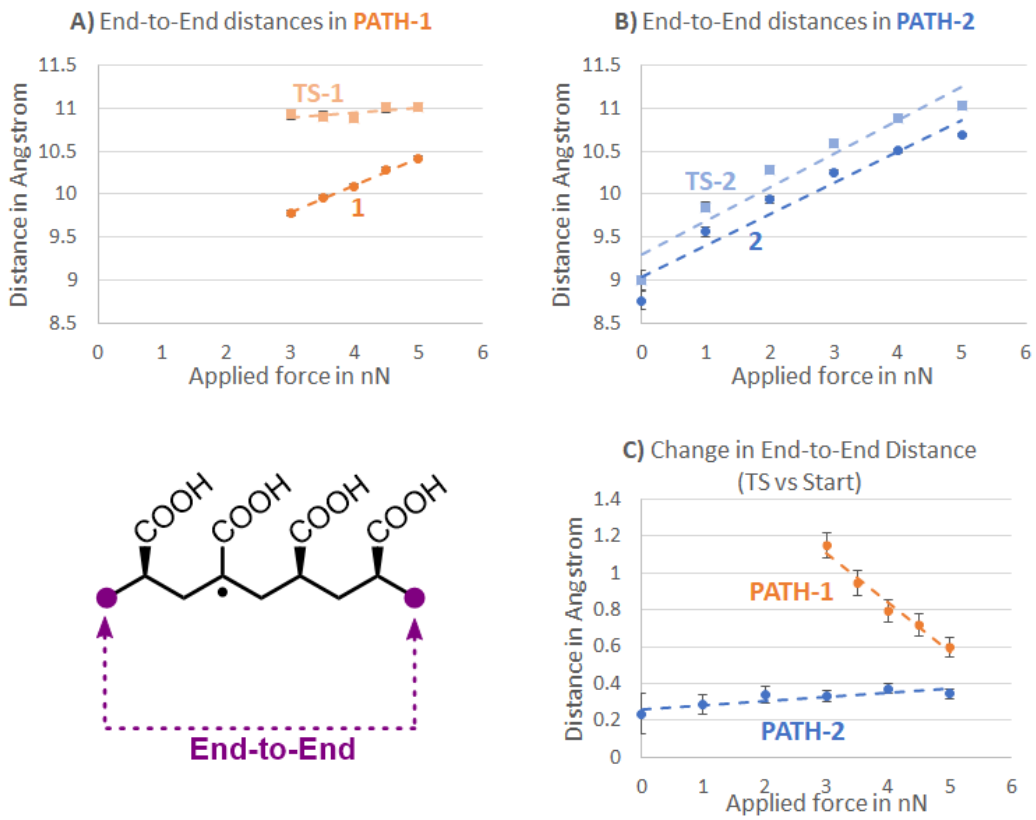

Figure 4-14. *The effects of applied force on the end-to-end lengths in* ***PATH-1*** *and* ***PATH-2.***

Quantitatively tracking the average end-to-end and scissile bond distances in **PATH-1** and **PATH-2** confirm the trends seen upon visual inspection of the structures. In the case of **PATH-1**, with increasing applied force, the ends of the polymer increasingly elongate (Compound **1**, Figure 4-14, A). However, the end-to-end distance of transition state **TS-1** remains relatively stationary,

increasing by ~0.1 Å (~1% of length) as the applied force increases (Compound **TS-1**, Figure 4-14, A). In essence, at higher force loadings, the end-to-end bond distance of **1** converges to that of **TS-1**. The starting and transition state structures of **PATH-2** do not exhibit this trend. Rather, both starting structure **2** and transition state structure **TS-2** elongate at a similar rate with increasing applied force (Figure 4-14, B). At comparable forces, the end-to-end bond lengths of **2** are longer than **1**, while the end-to-end bond lengths of **TS-2** eventually converge to similar lengths of **TS-1** at ~4 nN.

A better representation of the divergence of the end-to-end bond lengths is to observe how it changes between the starting structure and transition state at different force values (Figure 4-14, C). With increasing applied force, the end-to-end distance in **PATH-1** decreases at a rate of 0.27 Å per nN of applied force. However, while the end-to-end lengths of **2** and **TS-2** consistently increase with force, in **PATH-2** the end-to-end distance only increases at a rate of 0.02 Å per nN of applied force, essentially keeping the change in polymer length constant between **2** and **TS-2**.

While in **PATH-1** the end-to-end length of **1** converges to that of **TS-1** with increasing force, we see the opposite trend in the change in scissile bond length (Figure 4-15, A). The length of the scissile bond remains relatively unchanged in **1** with increasing force, but decreases substantially with increasing force with **TS-1**. In **PATH-2**, the scissile bond length in **TS-2** decreases at a slower pace compared to **TS-1**, while the bond length in **2** is essentially unchanging (Figure 4-15, B). In both cases, we can interpret this as the transition state of bond scission coming earlier and earlier in the bond scission event, which is consistent with the notion that under force, the structure of transition state converging towards starting structure.

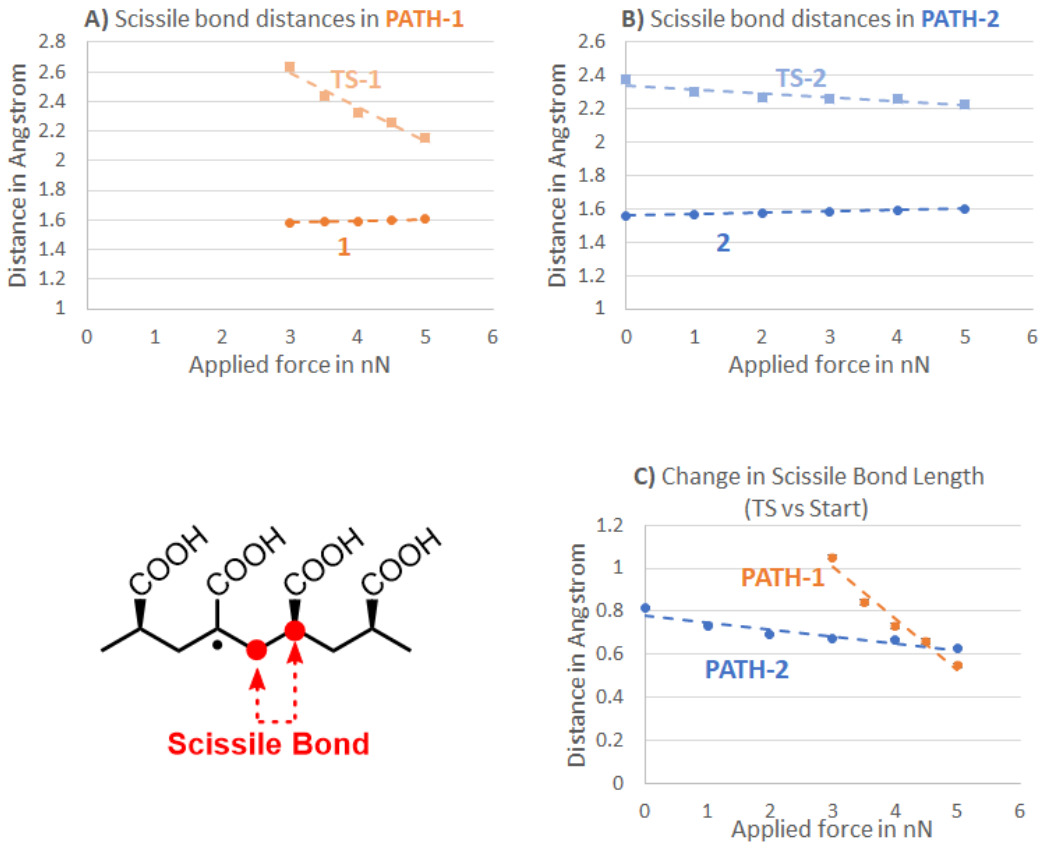

Figure 4-15. The effects of applied force on the scissile bond distances in **PATH-1** and **PATH-2**.

It is noteworthy, however, that if we look at the change in scissile bond length between the transition state and starting structure at different force values (Figure 4-15, C), the change in scissile bond length decreases at a much faster rate in **PATH-1** than **PATH-2**. Just as is seen in the change in end-to-end lengths (Figure 4-15, C), the geometries of structures in **PATH-1** appear to converge together at higher force values, while in **PATH-2**, the geometric differences between **TS-2** and **2** are mostly maintained, even at high levels of force.

Under the assumption that the transition state does not appreciably change with increasing amount of applied force, the change in activation barrier with force for a given reaction is thought to be caused by the energy of applied force (**ΔE_{AF}**, Figure 4-16), which is simply the energetic

contribution stemming from the gradient that force creates.[133] In the transition state searching, force was applied directly to the ends of the polymer, so we measure ***Δx*** as the difference in end-to-end distance between the starting structure and the transition state. Figure 4-16 details the calculated ΔE_{AF} for **PATH-1** and **PATH-2**. In **PATH-2**, we see a linear relationship between applied force and ΔE_{AF}, with a slope of approximately -5.15 kcal/mol per nN. This approximately mimics the decrease of 3.97 kcal/mol per nN we see in $\Delta H^{\ddagger}$ with increasing force (Figure 4-10). However, in the case of **PATH-1**, ΔE_{AF} increases with force, at a rate of about 2.89 kcal/mol per nN. The ability of ΔE_{AF} to predict the change in activation energy in **PATH-2**, and inability to provide the same prediction in **PATH-1**, suggests that the application of external force does not heavily distort **TS-2**, but dramatically distorts **TS-1**. This observation is consistent with what is quantified in Figure 4-14 and Figure 4-15.

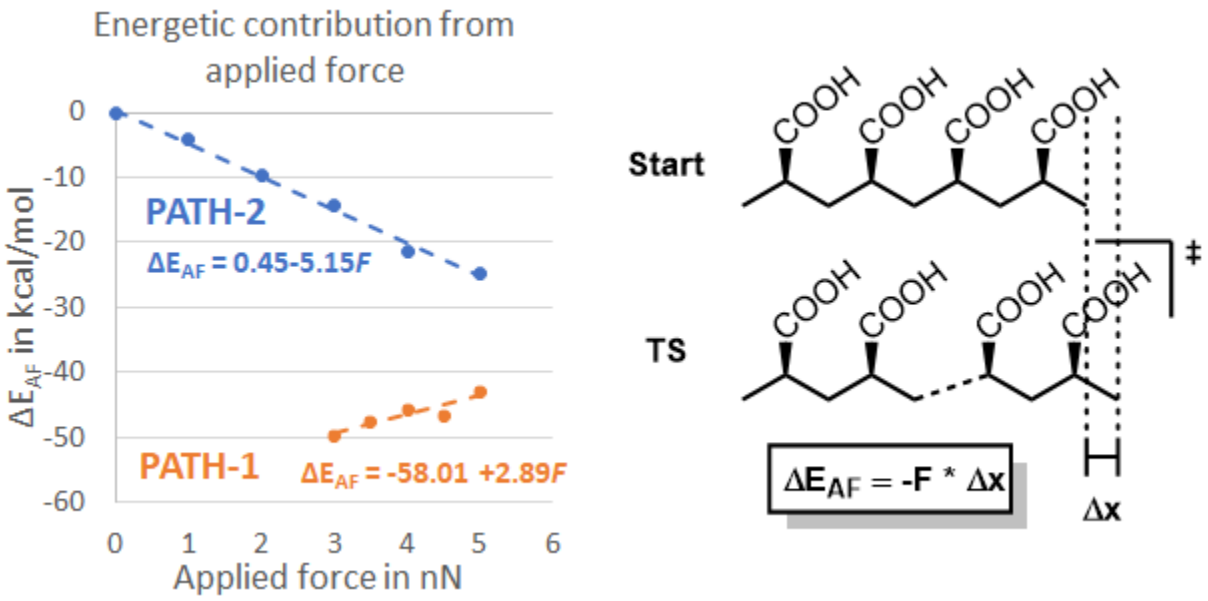

Figure 4-16. *The energetic contribution from applied force (ΔE_{AF}) observed in* ***PATH-1*** *and* ***PATH-2.*** *The decrease in* ***$\Delta H^{\ddagger}$*** *with force in* ***PATH-2*** *can be explained though the steady increase in ΔE_{AF}.*

According to the TPES model, under application of force, the reactant and TS structures are expected to become more geometrically similar.[86,141] Plots A and B in Figure 4-17 detail the

normalized change in scissile bond distance and end-to-end length with force. In both **PATH-1** and **PATH-2**, the scissile bond length of the transition state approaches the scissile bond of the initial structure. However, in **PATH-1**, this trend is much more pronounced, and we also see a similar trend in the end-to-end lengths. The geometric distortion due to force in **PATH-1** is so great that the scissile bond lengths and end-to-end distances appear to be quickly converging to a single point.

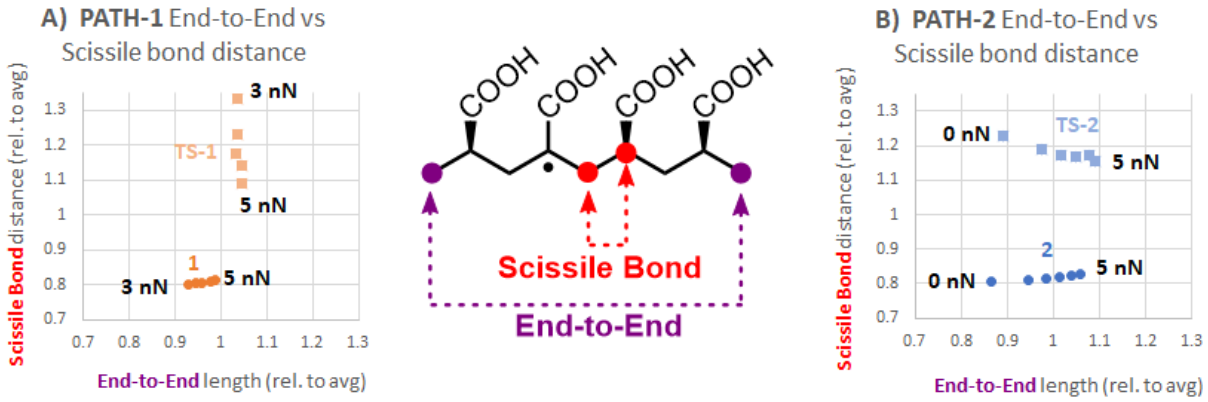

Figure 4-17. *Comparing the (relative) end-to-end and scissile bond distances of the starting and TS structures in* ***PATH-1*** *and* ***PATH-2.*** *The average end-to-end and scissile bond distances were calculated within each reaction path.*

4.7 Rationalizing why PATH-1 is More Responsive to Force Than PATH-2

With the application of force, **PATH-1** changes much more rapidly than **PATH-2**, both in terms of transition state energy, as well as starting and transition state geometry. As "force responsiveness" is a consequence of the inverse of the 2nd derivative of the PES,[142] the large differences in response to applied force suggest that the energy profiles of bond dissociation in **PATH-1** and **PATH-2** have very different curvatures. Indeed, without radical abstraction, bond scission in **PATH-1** follows a dissociative pathway that does not contain a transition state (Figure 4-18). However, upon abstraction of a radical, bond scission in **PATH-2** now follows a pathway with a transition state (Figure 4-18). A simple analytical model of the two reaction pathways can

explain this large difference in force responsiveness. **PATH-1** is modeled as a Morse potential, and **PATH-2**, as a quartic potential. The choice of these functions reflects the presence or absence of a transition state that is expected at no force. Each potential energy surface is then modified by a linear force times distance term, representing the shift of the potential profile with tensile forces. Parametrization of these energy surfaces was performed to fit the zero-force profiles from atomistic simulations, see the appendix for more details.

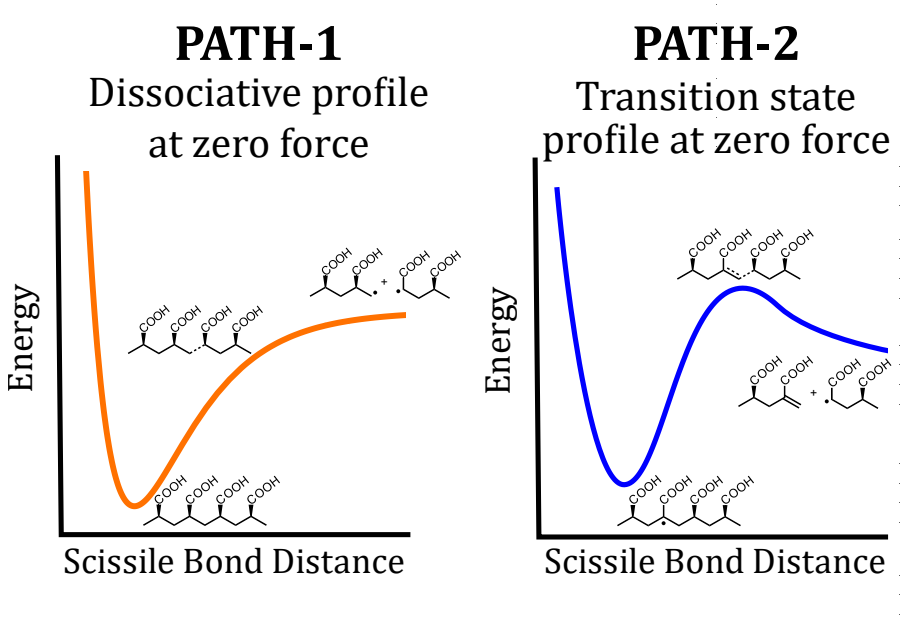

Figure 4-18. *Differences in the PES curvature of* ***PATH-1*** *and* ***PATH-2****.*

The results of the analytical model are shown in Figure 4-19. The bottom right of Figure 4-19 demonstrates that applying tensile forces has a greater effect on the Morse potential than the quartic potential. To understand this, the top of Figure 4-19 shows that **TS-1** is dragged downward by the applied force, while **TS-2** stays roughly constant. At the same time, **1** and **2** increase in energy at about the same rate with applied force. The net effect is that applied force reduces the barriers for **TS-1** as well as **TS-2**, but **TS-2**'s activation barriers move faster. The relative slope ($\frac{ESlope1}{ESlope2}$) of

2.1 for this highly simplified model is similar to that of the full atomistic model, with a slope of 2.0.

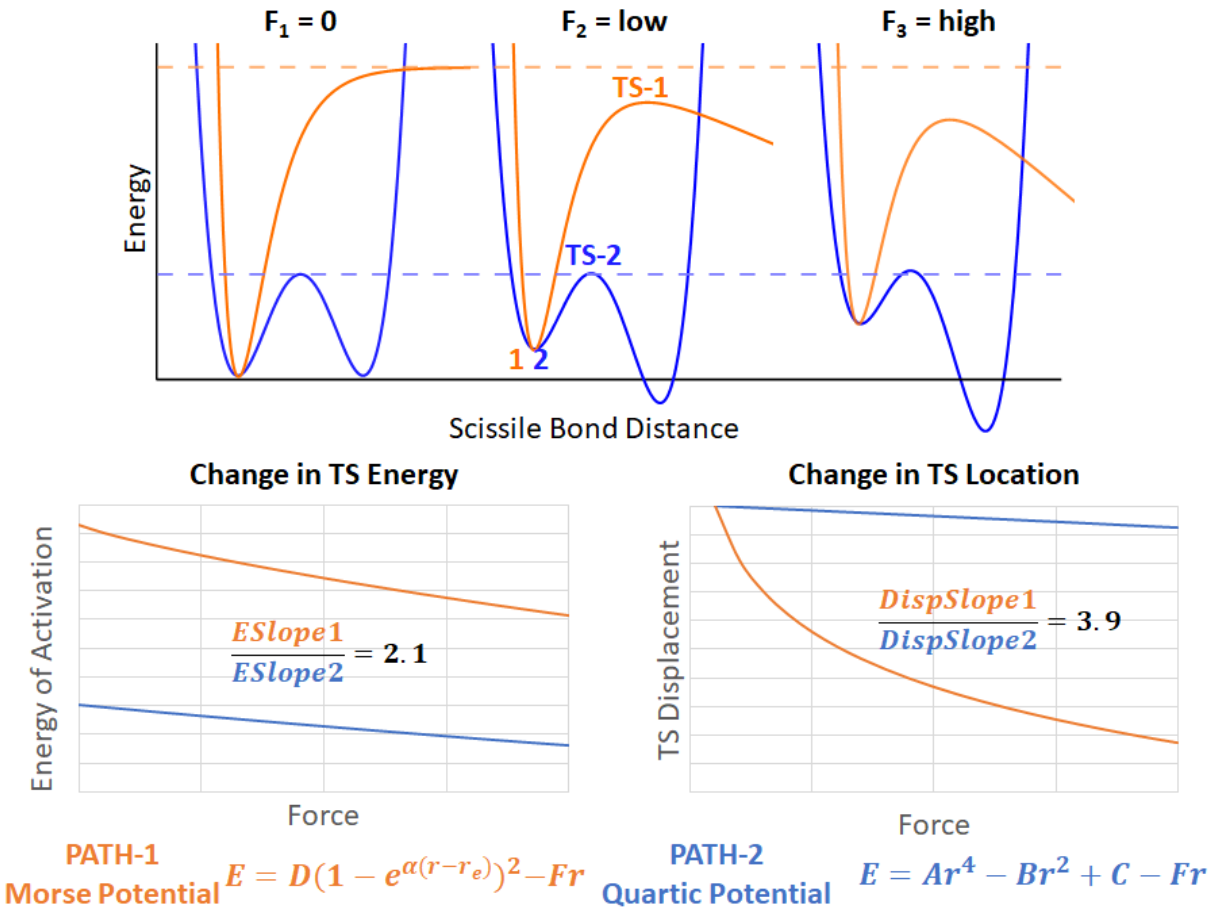

Figure 4-19. *(Top) How the Morse and quartic potentials behave under applied force (Bottom Left) Comparing the predicted TS energies of* ***PATH-1*** *and* ***PATH-2*** *using the example Morse and quartic functions. The ratio of the change in energy with force (ESlope1 vs ESlope2) is very close to the atomistic model. (Bottom Right) Comparing the displacement of the location of the TS using the example Morse and quartic functions. The ratio of the change in displacement with force at the last five data points (DispSlope1 vs DispSlope2) is consistent with the atomistic model.*

The simplified model results are also geometrically consistent with the full atomistic model (Figure 4-19, Bottom Left). As the amount of applied force increases, the scissile bond length of **TS-1** and **TS-2** move closer and closer to the lengths of respective reactant states **1** and **2**. Just as is seen in the atomistic model, **TS-1** changes at a much faster rate compared to **TS-2**. If we take the slope of the last 5 datapoints of the TS displacement/force relationship for both **TS-1** and **TS-2** ($\frac{DispSlope1}{DispSlope2}$),

we find that **TS-1** is displaced at 3.9 times the rate as **TS-2**, comparable to the 8-fold difference that we see in the atomistic model (Figure 4-15, raw numbers are included in the appendix).

4.8 Conclusions

In summary, abstraction of a radical from the polymer backbone is predicted to reduce the tensile strength of the polymer. Abstraction of a radical decreases the enthalpy of scission from 92.7 kcal/mol to 14.2 kcal/mol. Crudely, we can estimate that this 78.5 kcal/mol decrease lowers the tensile strength of the polymer from 6.6 nN to 2.6 nN. More accurately, by determining the transition state of bond scission of **1** and **2**, we can derive a linear relationship between applied force and enthalpy of activation. Using this relationship, we can refine our estimations of the effective tensile force of **1** and **2** to 4.7 nN and 2.5 nN, respectively, depending on assumptions about the timescale of bubble collapse, reaction temperature during bond scission, and ceiling temperature of PAA.

Compounds **1** and **2** are observed to behave quite differently under force. During degradation through **PATH-1**, the relative geometries of **TS-1** and **1** are significantly perturbed, but in **PATH-2**, the corresponding states do not change significantly. This has been measured by observing marked changes in **1** and **TS-1**, juxtaposed against the fairly minor changes seen in **2** and **TS-2**. By comparing the normalized rate of change of the scissile bond and end-to-end distances to the normalized change in TS energy in **PATH-1**, we can assert that the decrease in TS energy is due to the **1** and **TS-1** becoming more geometrically similar with greater force. As the relative geometries of **TS-2** and **2** don't change nearly as much, we find that ΔE_{AF} provides a good explanation for the decrease in TS energy seen in **PATH-2**. The difference in behavior between the two pathways can be explained as a consequence of the differences in the curvature of the PES of **PATH-1** and **PATH-2**.

These finding are relevant, as the limiting length of a polymer is dependent on the polymer's tensile strength.[119] As free radicals are capable of lowering the tensile strength of the polymer, this implies that degradation to shorter chains is possible in the presence of free radicals. The analysis presented here can be offered as an explanation for observations such as those by Koda where suppression of radical formation decreases the limiting length of the polymer,[106] and suggest that new strategies in polymer degradation are possible by leveraging the synergy between mechanochemistry and radical attack.

Chapter 5: Conclusions and Final Thoughts

5.1 Research Summary

Despite the rugged, mottled nature of the potential energy surface, only a handful of chemical states determine the thermodynamics and kinetics of a given chemical reaction. The central promise of computational chemistry is its ability to both identify and evaluate these key chemical states. Some of the chapters in this work have mainly been focused on key state identification (Chapters 2, 3), whereas other chapters have focused on understanding and evaluating key states (Chapter 4). As demonstrated, both processes provide useful insights for further reaction development.

In Chapter 2, the mechanism of a nickel-catalyzed three-component coupling reaction of an aldehyde, alkyne, and enoate is explored. Prior work on the related reductive [3+2] cycloadditions suggested that two distinct reaction mechanisms were possible, either an aldol-first mechanism involving a 7-membered metallacycle,[50] or a ketene-first mechanism involving a ketene intermediate.[51] As both mechanisms had experimental support for related reactions, the actual nature of the studied three-component coupling remained ambiguous. Computational studies provided value, then, because the mechanism of the specific reaction of interest could be directly interrogated. It was found that the aldol-first and ketene-first pathways were both feasible (**Figure 5-1.** A summary of Chapter 2. Two mechanisms for the three-component coupling reaction were found to be plausible. The selectivity for a specific mechanism appears to be affected by the placement of a methyl group at different positions of the enoate.Figure 5-1), but alkoxide elimination in the ketene-first regime is fast enough

to outcompete metallacycle isomerization, meaning that a ketene-first mechanism appears to be more likely. However, the substitution pattern of the enoate appears to play a role in the choice of mechanism, as in α-

substituted enoates, ketene elimination is much more difficult, due to the steric encumbrance provided by a group in the α-position. With α-substituted enoates, metallacycle isomerization is now faster than ketene elimination, which can explain the experimental observation of a linear side product in only α-substituted enoates, that implicates the existence of a 7-membered metallacycle. Overall, while the ketene-first pathway was found to be generally favored in the study, it exists in a precarious balance with an aldol-first mechanism, and as the experience with α-substituted enoates shows, small changes are capable of changing the preferred mechanism of the reaction. This work suggests that a similar balance may exist with other reductive [3+2] cycloaddition reactions, which, as it eventually turned out, includes the activation mechanism of fumarate catalysts detailed in Chapter 3.

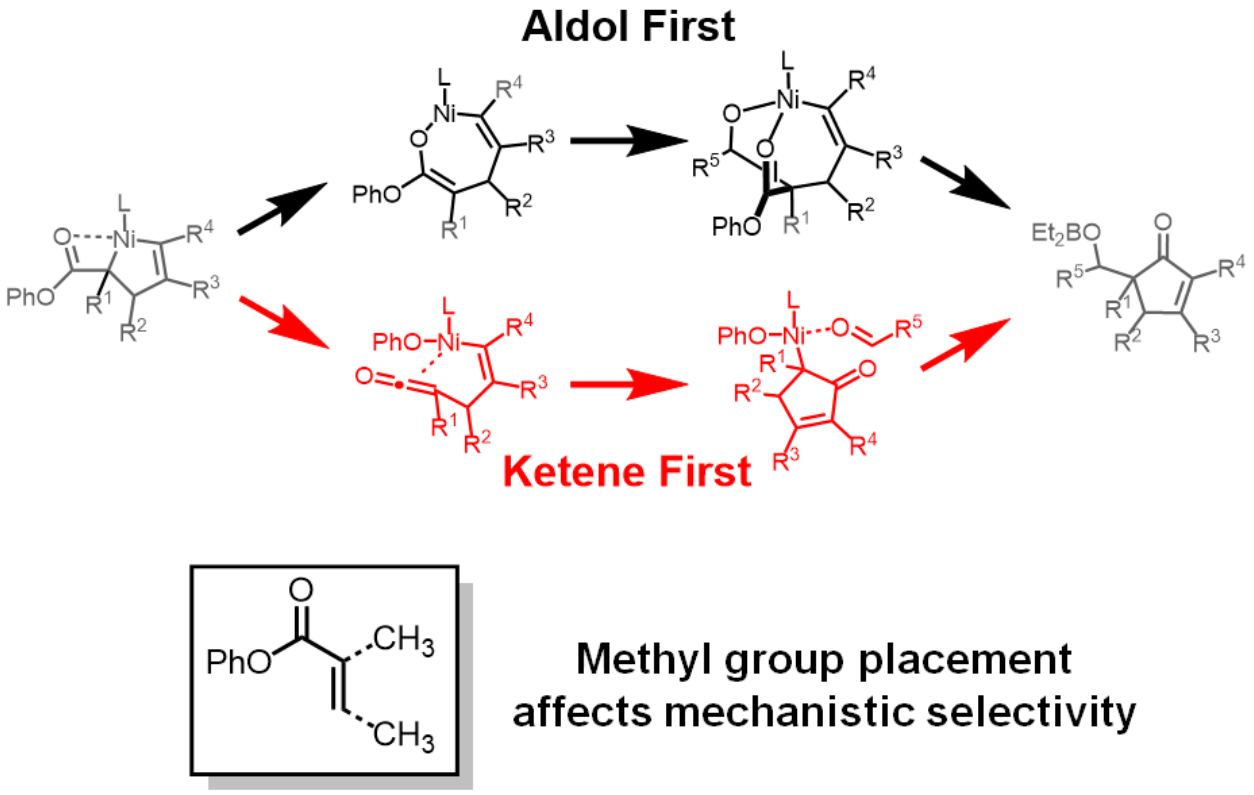

Figure 5-1. *A summary of Chapter 2. Two mechanisms for the three-component coupling reaction were found to be plausible. The selectivity for a specific mechanism appears to be affected by the placement of a methyl group at different positions of the enoate.*

Chapter 3 focused on the development of air-stable nickel(0) NHC (N-heterocyclic carbene) pre-catalysts, and explaining why competent catalysts could be developed with the NHC IMes, but not with the NHC BAC. Fumarates were chosen as a stabilizing ligand, as they were already known to be air-stable,[83] and it was thought that they could be tuned to become more reactive (Figure 5-2, A). A series of air-stable fumarate catalysts were developed that could catalyze the reductive coupling of an alkyne with an aldehyde. While it was originally believed that the activation mechanism of the fumarate catalysts involved the dissociation of both fumarate ligands, computational analysis of the binding energies of those catalysts determined that such an activation mechanism is unlikely (Figure 5-2, B). Even the weakest bound fumarate complex studied had a binding energy of at least 13.8 kcal/mol, indicating that the fumarate catalyst would be expected to be over 10 billion times slower than a catalyst formed *in situ*. The high activity of the fumarate catalysts, coupled with the knowledge that a fumarate could act as a catalyst poison, suggested that an activation mechanism where the fumarate is consumed must be active (Figure 5-2, C).

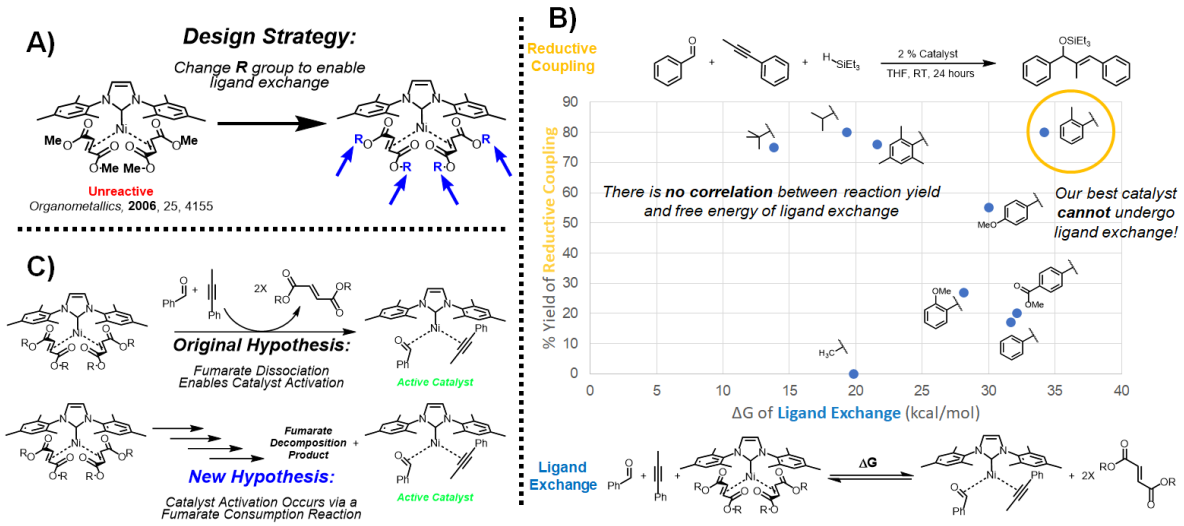

Figure 5-2. *(A) Original design strategy to develop an air-stable Ni(0) pre-catalyst. (B) No Correlation between reaction yield and the free energy of ligand exchange was observed. (C) The absence of such a correlation suggests that a fumarate consumption reaction must be active.*

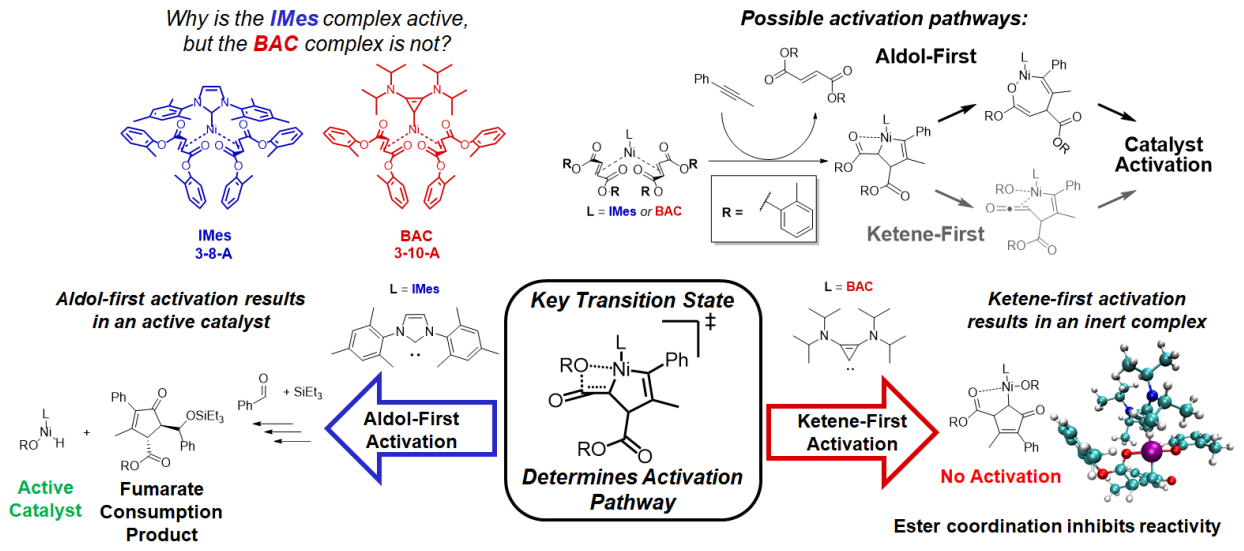

Figure 5-3*. The insights gained from Chapter 2 explain why complex **3-8-A** is active, but complex **3-10-A** is not. The two complexes undergo activation through different mechanisms. **3-8-A** goes through an aldol-first mechanism, allowing for catalyst activation, but **3-10-A** undergoes a ketene-first activation, resulting in a stable ester-ligated complex.*

Leveraging this computational insight, experimentalists were able to isolate the products of the predicted fumarate consumption mechanism. As the fumarate consumption products were similar to the products of the three-component coupling reaction detailed in Chapter 2, both the aldol-first and ketene-first activation mechanisms for IMes and BAC fumarate complexes were investigated. Like the previous case, mechanism selectivity appeared to be driven by barrier for ketene elimination (Figure 5-3). For IMes complex **3-8-A**, the barrier for ketene elimination is large, allowing the catalyst to undergo activation through an aldol-first mechanism. However, ketene elimination is facile for BAC catalyst **3-10-A**, suggesting a ketene-first mechanism. This difference proves to be critical, as the presence of a chelating ester moiety means that the BAC catalyst can form a highly-stable carbocyclic complex, trapping the catalyst. However, the IMes catalyst never gets trapped as a highly stabilized species, allowing for the catalyst to activate. Through the investigating the mechanism of the activation process with computational chemistry, our understanding of the fumarate catalyst was revolutionized. Applying this insight, preliminary

studies in changing the fumarate catalyst to prefer an aldol-first activation path over a ketene-first activation path provide a direction for the future.

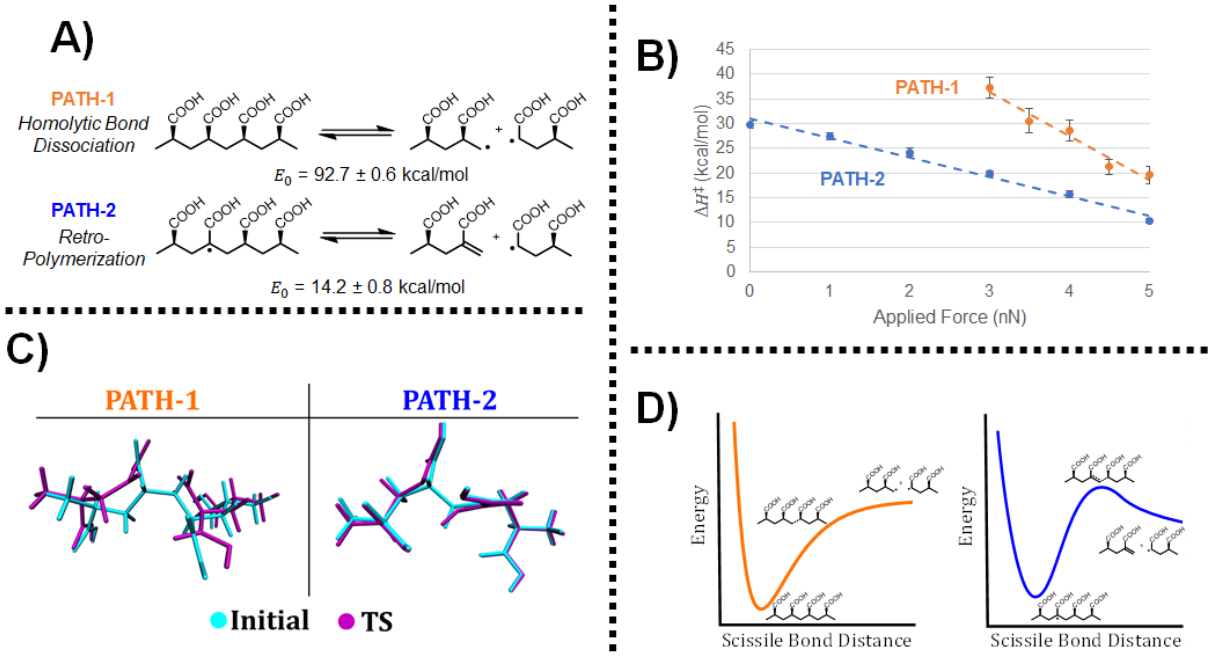

Figure 5-4. *A summary of Chapter 4.* ***(A)*** *Radical abstraction imparts a significant change in the enthalpy of bond scission.* ***(B)*** *The barrier for bond scission in* ***PATH-1*** *and* ***PATH-2.*** ***(C)*** *Differences in the geometries of key states in* ***PATH-1*** *and* ***PATH-2.*** ***(D)*** *We can explain the differences in behavior between* ***PATH-1*** *and* ***PATH-2*** *to be due to the changes in the curvature of the potential energy surfaces of the two processes.*

In Chapter 4, the effect of radical abstraction on the force-enabled bond scission of poly(acrylic acid) was investigated. Radical abstraction was found to reduce the enthalpy of bond scission by 78.5 kcal/mol, from 92.7 kcal/mol (**PATH-1**, no radical abstraction) to 14.2 kcal/mol (**PATH-2**, with radical abstraction) (Figure 5-4, A). By treating the C-C bond as a Morse oscillator, and assuming bond scission occurs when no barrier exists for it on the potential energy surface, a crude estimation of the change in tensile strength suggests that radical attack reduces the tensile strength of PAA from 6.6 nN to 2.6 nN. Using transition state searching methods recently developed in the Zimmerman group,[96] the transition states of bond scission under force were determined for **PATH-1** and **PATH-2**. **PATH-2** was found to generally have a lower barrier for bond scission, the barrier

for bond scission in **PATH-2** decreased with increasing applied force compared to **PATH-1**. Using the linear relationship of bond scission barrier with applied force, effective tensile strengths in **PATH-1** and **PATH-2** were calculated to be 4.7 and 2.5 nN, respectively (Figure 5-4, B). Additionally, the rationale for how force affects the barrier for bond scission was postulated to be different in both **PATH-1** and **PATH-2**. In **PATH-1**, the geometries of the starting structures and transition states of bond scission were found to change substantially upon application of applied force, whereas geometric distortions in **PATH-2** under force are fairly minimal (Figure 5-4, C). The large geometric distortions under force, pushing the starting structure and transition state closer together, can rationalize the decrease in bond dissociation energy in **PATH-1**. The lack of distortion in **PATH-2**, on the other hand, can be explained by the energy of applied force, the energetic benefit of bond lengthening in the transition state under force. The difference in behavior between **PATH-1** and **PATH-2** can also be explained as a consequence of the difference in the curvature of their respective PESs (Figure 5-4, D). The insights discovered in this chapter suggest a mechanism of synergy between radical attack and application of tensile force, and may aid in the development of new depolymerization technology.

5.2 Possible Future Directions for the Material Studied in This Work

Chapters 2 and 3 were mainly focused on the identification of the key states involved in the three-component coupling reaction, or fumarate catalyst activation, rather than understanding their nature. Now that metallacycle isomerization and ketene elimination have been identified as key states, it may be a worthwhile endeavor to try to better understand what factors are capable of stabilizing and destabilizing them. Tools such as energy decomposition analysis,[143] orbital analysis,[144] or distortion-interaction analysis[145,146] are all possible means of calculating the impact of specific features on the selectivity between an aldol-first or a ketene-first reaction. In addition

to directly computing the effects of specific descriptors, selectivity-determining features could also be found through statistical analysis.[147]

While identifying the features that determine mechanism selectivity for the reactions studied in Chapters 2 and 3 would be of academic interest, the practical interest of such an inquiry would be in the development of new pre-catalysts. Smaller NHCs represent an attractive target for pre-catalyst development, as they have been more unreliable in our hands in *in situ* procedures. The preliminary computational work to identify an active BAC fumarate catalyst has already yielded several candidates of interest, and the relatively minor amount of work required to yield those results suggests that future attempts with BAC and other NHCs will prove to be similarly facile.

Additionally, the computational analysis described in this work have provided multiple hypothesis that can be easily proven or disproven through experimental work. For instance, in Chapter 3, the failure of a BAC fumarate catalyst to activate is hypothesized to be due to its proclivity to become trapped as an organometallic carbocyclic compound. In theory, this species, or species derived from it, should be isolable in experiment. The success of such an experiment would provide direct evidence that complexes such as **3-10-A** undergoes a ketene-first activation process, but get trapped in the process. Such a finding would give credence to the approach of developing fumarate catalysts that go through an aldol-first activation pathway.

Chapter 4 provides many hypotheses that need to be tested as well. For instance, AFM experiments to test the effect of radical abstraction on tensile strength would directly confirm the central assertion of Chapter 4. At the time of writing, such an experiment is being actively researched in the McNeil group. Additionally, calculations of the rate of bond scission through **PATH-1** and **PATH-2** give an estimation on the ratio of limiting length expected during the sonication of poly(acrylic acid) in the presence and the absence of free radicals. This should be directly

measurable, either through the use of radical quenching reagents to inhibit the action of any radicals generated in solution,[106] or through the introduction of a radical generating source such as Fenton's reagent.[110] As computation provides a quantitative prediction of the expected ratio of limiting lengths, such an experiment would be a useful barometer for our understanding of the role of radicals in the sonication process.

5.3 On the Frailty of Human Understanding

In a famous philosophy paper, Edmund Gettier attacked the notion that "justified belief", i.e. the existence of supporting evidence for a belief, is sufficient to constitute knowledge.[148] Gettier provides counterexamples, where the justification for an individual's belief is based on a flawed premise that makes a successful prediction by coincidence, creating the illusion that the individual's belief is knowledgeable. While the original "Gettier problem" consisted of a contrived example concerning the prediction of employment based on the applicant's pocket's contents, real-world examples of Gettier problems are not uncommon in the research process.

For instance, the initial stages of catalyst design in Chapter 3 played out exactly like a Gettier problem. The original set of IMes fumarate complexes were designed under the false premise that catalyst activation occurs through a dissociative mechanism. The fumarates were chosen for their perceived lack of binding affinity, due to their enhanced steric bulk as compared to the original methyl substrates used by Cavell.[83] When the synthesized catalysts were found to be productive, the result was originally interpreted as a justification for a dissociative mechanism. But that success was coincidental. The subsequent computational work detailed in this chapter demonstrated that in order for the catalyst to activate, rather than simply dissociate, the fumarate needed to be destroyed. We had originally believed in a wrong mechanism, despite making a successful

prediction that provided justification for our initial beliefs. Our initial success was not due to our knowledge of catalyst activation, but due to random chance.

Even the most carefully justified models can fail to capture the entire picture. In reporting the nickel-catalyzed reductive [3+2] cycloaddition of enoates and alkynes, Montgomery[50] and Ogoshi[51] detail distinctly different mechanisms for the formation of product, and both groups provided solid experimental evidence for their assertions. In the analysis in Chapter 2, both mechanisms prove to be viable, and the selectivity between the two mechanisms is easily shifted by small perturbations. How often does one consider the possibility that two slightly different substrates can react with the same catalyst to make the same corresponding product, but will go through completely different mechanisms? How different would our understanding of [3+2] reductive cycloadditions be, if only one set of mechanistic studies was published, rather than two?

5.4 On the Symbiosis Between Theory and Experiment

What is instructive, then, is how falsely held beliefs can be dispelled with a new perspective. For instance, in Chapter 3, computational analysis was able to propose a different mechanism of catalyst activation through the calculation of binding energies. Computational chemists are well equipped to interrogate specific queries, but are less able to answer more general questions. While analysis of the binding energies of fumarate clearly demonstrated that some activation mechanism occurred, which consumed the fumarate, that analysis did not indicate what kind of reaction was occurring. Despite months of work, computational efforts to identify the mechanism of fumarate consumption were fruitless, and that question was only resolved once some of the products of fumarate consumption were ultimately isolated experimentally. General queries, such as determining the result of a given reaction, are much more easily answered through experiment than through computation.

In short, the strengths and deficiencies of experiment and computation naturally complement each other, and combined together they can enjoy a symbiotic relationship. Such a relationship is displayed throughout Chapter 3, as the chapter consists of a series of iterations where the experimentalists feed insight to theoreticians, and vice versa. It is impossible to talk about the contributions from one side without mentioning the other. The experimentalists would be lost, chasing after the wrong mechanism of catalyst activation, absent a computational investigation. The theoretician would be stuck, unable to process all possible methods of fumarate consumption, without experimental isolation of the products of fumarate consumption. Computational chemistry has always needed the support of experimentalists, as they ultimately need to test in the real world the predictions made in simulation. But, as Chapter 3 demonstrates, the growth of computing power and the development of better tools have made computational chemistry powerful enough that perhaps the experimentalists need the theoreticians as well.

Appendix

A.1 Computational Details for Chapters 2 and 3

Density functional calculations were performed using Q-Chem 3.1.0.0[149] for geometry optimization and frequency calculations, and ORCA 4.0.0.2[150] for single point calculations. All geometries for intermediates and transition states were optimized using the ωB97X density functional[13] and 6-31G(d) basis set.[151,152] Energies were refined by applying the ωB97X-D3 density functional[11] with the cc-pVTZ basis[153,154] and the SMD implicit solvent model[155] with toluene as the solvent ($\epsilon = 2.4$) in Chapter 2, or tetrahydrofuran as the solvent in Chapter 3 ($\epsilon = 7.25$). Transition state geometries and minimum energy reaction paths were found using the single-[26] and double-ended[24,25] growing string methods. Found transition states were subsequently re-optimized after the initial search. All energies listed are Gibbs free energies with enthalpy and entropy corrections at 363 K for Chapter 2, or 298 K for Chapter 3. Entropy corrections were scaled to 50% to account for the difference in entropy between the gas and solvated phases.[156] The effects of low frequency oscillations were reassigned to 50 cm^{-1} to prevent the highly anharmonic vibrations from overly influencing the free energy. All intermediates and transition states were confirmed to have the appropriate number of imaginary frequencies: one for transition states, and none for intermediates. All geometry optimizations, frequency calculations, were performed with an SCF convergence tolerance of 10^{-6}. Single point calculations were performed with an SCF convergence tolerance of 10^{-8}.

A.2 Raw Energies of Structures in Chapter 3

The values used to calculate the relative energies reported for the activation IMes complex **3-8-A** are reported in Table A-1. The values used to calculate the relative energies reported for the activation BAC complex **3-10-A** are reported in Table A-2. The values for the small molecules used for energy balance in to investigate the pathways of both complexes are given in Table A-3. The values used to calculate the relative energies of ketene elimination and metallacycle isomerization for various BAC complexes are given in Table A-4.

	Electronic Energy	Zero-Point Correction	Entropy
Complex	In hartrees	In kcal/mol	In cal/mol
IMes-I	-3777.07273088773	573.922	280.182
IMes-II	-3777.06117723177	573.143	283.499
IMes-TS-II-A	-3777.04514633182	572.894	288.034
IMes-III-A	-3777.05906179391	574.141	279.708
IMes-TS-III-A	-3777.04332245166	570.850	290.026
IMes-TS-II-B	-3777.03518980009	572.965	284.492
IMes-III-B	-3777.04967194343	571.860	288.283
IMes-IV-A	-3777.05529741875	572.734	291.940
IMes-V-A	-4221.92540429087	643.799	322.100
IMes-TS-V-A	-4221.91122019430	645.019	315.399
IMes-VI-A	-4221.93699056449	646.246	318.960
IMes-VI-A-THF	-4454.43215241548	725.763	344.347
IMes-TS-VI-A	-4631.81573109319	729.845	340.705
IMes-VII-A	-4631.84843879111	728.486	353.729
IMes-VIII-A	-4631.86712697850	727.700	354.000
IMes-TS-VIII-Z	-4631.81904752115	725.879	360.842
IMes-IX-Z	-4631.88041138076	731.512	346.623
IMes-TS-VIII-A	-4631.83086136393	727.761	348.589
IMes-IX-A	-4631.88910809406	728.400	354.700

Table A-1. *Energetic values used to calculate relative energies in the activation pathway of IMes catalyst* ***3-8-A****.*

	Electronic Energy	Zero-Point Correction	Entropy
Complex	In hartrees	In kcal/mol	In cal/mol
BAC-I	-3550.76343327492	578.960	279.691
BAC-II	-3550.75674927357	577.728	280.608
BAC-TS-II-A	-3550.74925510619	578.010	280.754
BAC-III-A	-3550.75561877717	578.742	281.754
BAC-TS-III-A	-3550.72892166746	577.582	*284.884*
BAC-IV-A	-3550.74538535549	579.194	280.742
BAC-TS-II-B	-3550.73607756652	576.436	287.907
BAC-III-B	-3550.75087524428	576.949	286.110
BAC-TS-III-B	-3550.74774549022	576.884	284.392
BAC-IV-B	-3550.79413870639	579.320	274.808
BAC-TS-IV-B	-3960.65643023093	660.998	314.962
BAC-V-B	-3205.14638400882	500.812	246.156
BAC-TS-V-B	-3205.09188866902	500.374	249.289
BAC-VI-B	-3205.15075011543	501.862	248.227

Table A-2. *Energetic values used to calculate relative energies in the activation pathway of BAC catalyst* ***3-10-A****.*

	Electronic Energy	Zero-Point Correction	Entropy
Structure	In hartrees	In kcal/mol	In cal/mol
4-Fluorobenzaldehyde	-444.849789364677	69.976	87.066
Tetrahydrofuran	-232.476787942352	78.456	73.154
Trimethylsilane	-409.886233904854	81.594	81.022
Trimethyl(*o*-tolyloxy)silane	-755.554325411818	159.348	120.207

Table A-3. *Energetic values of small molecules used in the calculations of the activation pathways of both* ***3-8-A*** *and* ***3-10-A****.*

Step	Fumarate	Electronic Energy In hartrees	Zero-Point Correction In kcal/mol	Entropy In cal/mol
Reference Structure **(BAC-I)**	B	-3245.91786662683	545.782	262.207
	C	-3708.05413664578	653.753	307.495
	D	-3786.65666774105	691.481	310.894
	E	-3701.18954413056	584.265	291.184
	F	-3701.18423696250	584.668	291.281
	G	-3927.93003945740	600.994	302.797
	H	-3472.12061691597	541.119	266.985
	I	-3088.62438412179	470.217	241.505
	J	-3550.75595586925	577.783	283.021
	K	-4012.88691971857	689.340	318.855
	L	-4146.30809886054	551.998	295.784
	M	-3786.65666774105	691.481	310.894
Ketene Elimination **(BAC-TS-II-B)**	B	-3245.8741121607	543.421	266.582
	C	-3708.0161805980	652.128	307.922
	D	-3786.6275131312	690.863	313.821
	E	-3701.1698962121	584.891	293.175
	F	-3701.1673810115	584.509	289.833
	G	-3927.9066423323	600.542	312.494
	H	-3472.0938845943	539.281	274.493
	I	-3088.5819107818	468.205	246.462
	J	-3550.7159490670	577.768	286.908
	K	-4012.8532280731	687.520	321.935
	L	-4146.2850054481	550.963	303.283
	M	-3786.6275131312	690.863	313.821
Metallacycle Isomerization **(BAC-TS-III-A)**	B	-3245.8774350755	544.866	269.403
	C	-3708.0145582864	652.361	315.516
	D	-3786.6276568147	691.517	313.872
	E	-3701.1539418405	585.213	296.583
	F	-3701.1496653065	584.945	295.110
	G	-3927.8960549849	601.138	312.019
	H	-3472.0850514741	540.094	274.022
	I	-3088.5839657167	469.529	248.021
	J	-3550.7187597531	579.036	289.319
	K	-4012.8534021955	688.316	323.586
	L	-4146.2741266509	550.520	308.544
	M	-3786.6276568147	691.517	313.872

Table A-4. *Energetic values used in the comparison of ketene elimination with metallacycle isomerization of BAC complexes using different fumarates.*

A.3 Methodology Used in Chapter 4

To capture the behavior of PAA, an isotactic tetramer was used as a model system (**1**) (Figure A-1). The effects of radical abstraction were modeled using the same tetramer, minus an α-hydrogen next to a central carboxyl group (**2**) (Figure A-1). Conformers for **1** were generated using the Confab tool[130] in Open Babel.[131] 8 unique conformers were identified. Conformers for **2** were generated by abstracting the α-hydrogen from each of the conformers of **1**.

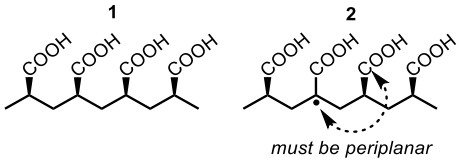

Figure A-1. *Model PAA systems used in this study.*

As hydrogen bonding is known to affect the heat of polymerization of protic polymers such as PAA,[132] and to ensure that the conformers used in this study are consistent with aqueous solvation, explicit water solvation was used. For each conformer of **1** and **2**, the system was surrounded by a 6 Å water shell containing 260 water molecules. Molecular dynamics (MD) simulations were used to create a series of snapshots of the tetramer in an aqueous environment. These simulations were carried out using the TINKER package, version 8.2.[157] 10 ns of NVT molecular dynamics was simulated with a 1 fs timestep using the CHARMM 22[17,18] forcefield with an Andersen thermostat and a modified Beeman integrator. Custom parameters were created to model the α-radical in **2** (see Section A.4). Water was treated using the TIP3P model. Electrostatic interactions were treated using Ewald summation, with a cutoff value of 7 Å. All other nonbonded interactions were treated using a cutoff of 8 Å. The entire system was simulated in a 23.418 Å by 19.166 Å by 18.613 Å rectangular cuboid box with periodic boundary conditions. After 2 ns of equilibration, snapshots were taken every 100 fs. For both model systems (**1** and **2**), the snapshots from each conformer

was combined into a single pool of 640 snapshots. The conformers were then relaxed using the OPTIMIZE function in TINKER.

The geometry of selected snapshots was then re-optimized using a quantum mechanical/molecular mechanical method (QM/MM). For the QM/MM optimizations, the QM region was treated using the B3LYP functional[12] with the 6-31G(d)[151] basis. Edge water molecules were fixed in place. The MM region was treated using the same CHARMM 22[17,18] forcefield also used in the MD simulations. The Janus model was used for electronic embedding.[16,19] Optimizations were performed with an SCF convergence tolerance 10^{-6}.

Not all of the collected snapshots from the MD simulations were used. For the QM/MM re-optimization of **1**, 200 of the 640 snapshots were used, taken at regular intervals. For **2**, snapshots were screened for those that had a proper alignment of the middle carboxylic acid with the α-radical. For a β-scission event to occur, the radical must overlap with the scissile bond to accommodate formation of a new pi bond.[158] This was defined as being within 20° of being anti-periplanar, or 30° of being syn-periplanar with the middle carboxylic acid (see Figure A-1). After screening all 640 snapshots of **2**, 121 were used for QM/MM optimizations. A flowchart for the entire process is shown in Figure A-2.

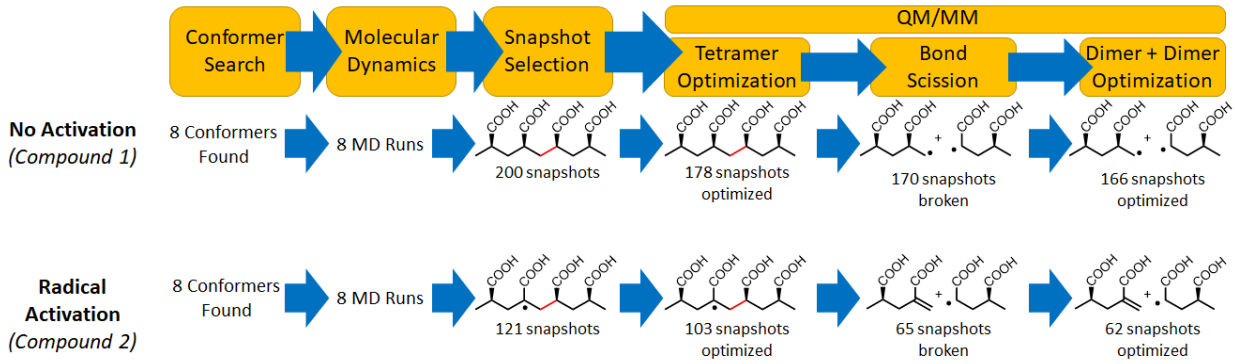

Figure A-2. *Flowchart for QM/MM optimization and bond scission.*

After optimizing the geometry of the snapshots, the scissile bond (shown in red, Figure A-2) was cleaved by applying a stretching force of 10 nN between the two atoms of the scissile bond using the EFEI (external force explicitly included) method.[133] After bond scission, subsequent re-optimization yielded two PAA dimers (referred to as dimer+dimer snapshots).

As Figure A-2 details, in the case of no radical activation (**1**), of the 200 snapshots used, 178 were successfully optimized using the QM/MM method, 170 were then successfully broken, and 166 snapshots were successfully re-optimized as dimer+dimer snapshots. For the no activation case, dimer+dimer optimization was performed on the triplet surface to prevent recombination, and then singlepoint energies on the singlet surface were then calculated. In the case of radical activation (**2**), of the 121 snapshots used, 103 were successfully optimized using the QM/MM method, 65 were successfully broken, and 62 of the dimer+dimer snapshots were successfully reoptimized.

The enthalpy of bond scission was determined by comparing the total energy of each dimer+dimer snapshots to the tetramer snapshot it came from. By averaging the difference in energy for each set of snapshots, a value for the enthalpy of bond scission could be obtained. In the no activation case (**1**), the 166 dimer+dimer snapshots were compared to their original tetramer snapshot. The same analysis was made for the 62 dimer+dimer snapshots in the radical activation case. For all optimized tetramers in the no activation and radical activation regimes, partial hessian vibrational analysis[134] was performed on the structures absent any explicit water. These values were averaged to yield the force constant of the scissile bond (shown in red, Figure A-2).

Using the reactant geometry and a C-C scission bond-dissociation coordinate, the single-ended growing string method allows for the identification of the transition state (TS) of a reaction, without prior guessing of the structure of the TS.[24] Roessler and Zimmerman described a such a method that includes force biasing (F-GSM).[96] Herein, double-ended F-GSM is used to identify

the structure of the TS of bond scission of **1**, and single-ended F-GSM is used to identify the structure of the TS of bond scission of **2**. A double-ended method was necessary to investigate **1** to calculate a driving coordinate that was sufficient to overcome the large bond dissociation energy of the reaction. Force was applied at the ends of the tetramer unit, shown in Figure A-3. Due to the complexity of the system, a tetrameric system was the largest polymer analogue that could be produce useful data in a reasonable timeframe. Boulatov has previously shown that any effects of the length of the model system would have a maximum error of ~4 kcal/mol, but that decreases sharply with increasing system size.[159]

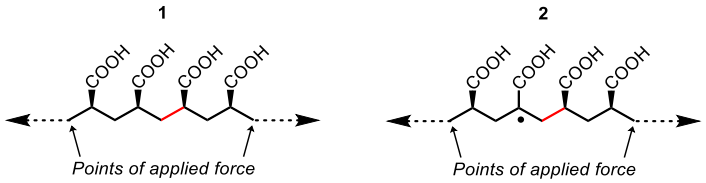

Figure A-3. *Points where force is applied on compounds **1** and **2**. The scissile bonds are shown in red.*

During ultrasonic depolymerization, the polymer strand will undergo a coil-stretch transition prior to scission.[91] This transition was found to have a confounding effect on the transition state energies obtained. To resolve this hysteresis problem, structures were optimized at a high level of force, and then relaxed to their optimized geometries at the desired force level.[96]

To optimize structures prior to the transition state searching, snapshots were re-optimized with force applied using the EFEI method.[133] For the scission of **1**, 129 snapshots of **1** were optimized at 6 nN, and then re-optimized at forces ranging from 3 to 5 nN. At these force ranges, the bond scission is sufficiently exothermic for the strings to have an energy profile consistent with having a transition state. Their corresponding dimer+dimer snapshots were similarly optimized, except that the procedure was performed on the triplet surface with the scissile atoms frozen. The tetramer/dimer+dimer pairs were then used as start and end structures to find the transition state

of bond scission using double-ended F-GSM. The resulting transition state energies relative to the starting structure was then averaged to yield a transition state energy at a given force value. A flowchart from this process is given in Figure A-4.

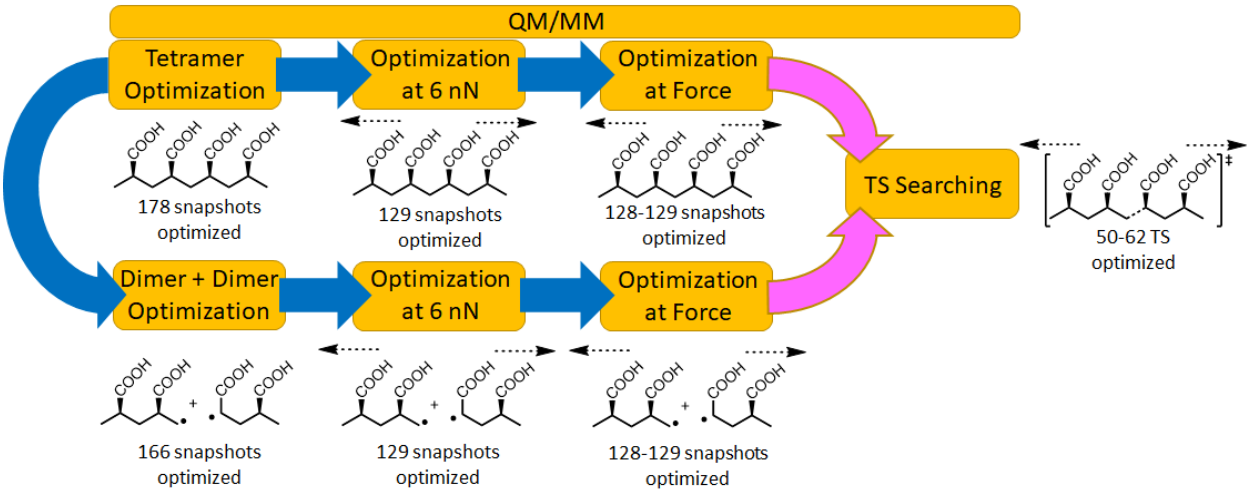

Figure A-4. *Flowchart for identifying the transition state of bond scission for compound* ***1****.*

For the scission of **2**, tetramers were extended using a force of 6 nN, and then relaxed to their optimized geometries at the desired levels of force. This ensured that the polymer strand remained straight, and avoided including the energy of polymer uncoiling in the transition state energy. The optimized structures were then used as starting points using single-ended F-GSM. The resulting transition state energies relative to the starting structure was then averaged to yield a transition state energy at a given force value. A flowchart from this process is given in Figure A-5.

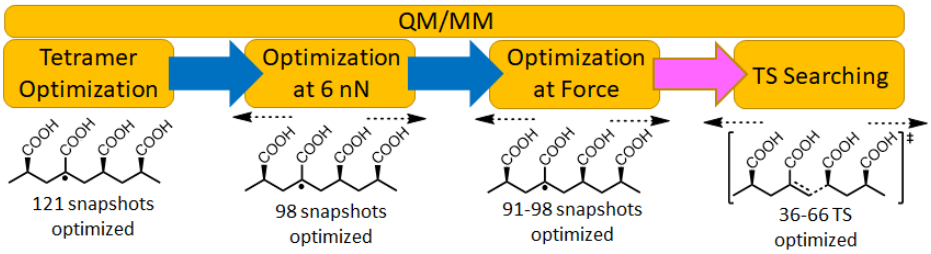

Figure A-5. *Flowchart for identifying the transition state of bond scission for compound* ***2****.*

In order to effectively interrogate the depolymerization of PAA under aqueous conditions, it is necessary to find a model that yields suitably accurate energetic information. The polymerization of acrylic acid under aqueous conditions is known to have an enthalpy of polymerization of 18.5 kcal/mol.[139] Given that the heat of polymerization of protic monomers is known to be affected by the hydrogen-bonding ability of the environment, we explored the use of a QM/MM system with explicit water molecules that were simulated using molecular mechanics. Using a QM/MM method with explicit water atoms, the value for the enthalpy of polymerization was found to be 15.9 kcal/mol.

A.4 Radical Parameters Used in the Molecular Dynamics Simulations in Chapter 4

The following molecular mechanics parameters were used to simulate the radical carbon in compound **2** for dynamics simulations performed in Chapter 4. They are designed to be used in conjunction with the CHARMM 22 parameter file ("charmm22.prm") included in TINKER, version 8.2.[157]

```
atom 999 99 RAD "Radical" 6 12.011 3
vdw 99 2.0900 -0.0680
charge 999 -0.0900
bond 99 42 300.00 1.4800
bond 99 13 365.00 1.5020
bond 99 14 365.00 1.5020
bond 99 1 36.50 1.1000
bond 99 12 440.00 1.4890
angle 42 99 14 65.00 123.50
angle 99 14 13 32.00 112.20
angle 99 14 1 45.00 111.50
angle 14 99 1 40.00 116.00
angle 99 42 52 75.00 126.00
angle 99 42 35 55.00 110.50
angle 42 99 1 32.00 122.00
angle 12 99 14 65.00 123.50
angle 1 99 12 52.00 119.50
angle 14 99 14 27.00 114.00
torsion 14 99 42 52 1.4000 180.00 2
torsion 14 99 42 35 1.4000 180.00 2
torsion 42 99 14 13 0.3000 0.00 3
torsion 42 99 14 1 0.0000 0.00 3
torsion 99 42 35 3 2.0500 180.000 2
torsion 42 13 14 99 0.2000 0.00 3
torsion 15 13 14 99 0.2000 0.00 3
torsion 14 13 14 99 0.2000 0.00 3
torsion 1 13 14 99 0.2000 0.00 3
torsion 42 99 52 35 53.0000 0.00 0
torsion 14 13 14 99 0.2000 0.00 3
torsion 13 14 99 1 0.0000 0.00 3
torsion 1 99 14 1 0.0000 0.00 3
torsion 1 99 42 52 0.0000 180.00 2
torsion 1 99 42 35 0.0000 180.00 2
torsion 13 14 99 12 0.2000 0.00 3
torsion 12 13 14 99 0.2000 0.00 3
torsion 12 99 14 1 0.0000 180.00 3
torsion 14 99 14 1 0.0000 0.00 3
torsion 13 14 99 14 8.5000 180.0
```

A.5 Data Used to Calculate the Tensile Strength and Rates of Bond Scission in Chapter 4

To calculate the tensile strength using the Morse method, the force constant of the scissile bond, κ, as well as the energy of bond dissociation, E_0 need to be calculated. Averages of those values are listed in Table A-5 and Table A-6.

	Avg. E_0 (kcal/mol)	Std. Err.	Std. Dev.	N
PATH-1	92.722	0.6126	7.8925	166
PATH-2	14.199	0.7763	6.1126	62

Table A-5. *Average calculated bond dissociation energy values in* ***PATH-1*** *and* ***PATH-2****.*

	Avg. κ (nN/Å)	Std. Err.	Std. Dev.	N
PATH-1	54.0700	0.076961	1.032538	180
PATH-2	54.0471	0.096577	0.970591	101

Table A-6. *Average calculated force constants in PATH-1 and PATH-2.*

Table A-7 tabulates the average barriers for bond scission in **PATH-1** and **PATH-2**.

	Force in nN	Avg. $\Delta H^{\ddagger}$ in kcal/mol	Std. Err.	Std. Dev.	N
PATH-1	3	37.212	2.109	15.644	55
	3.5	30.568	2.547	18.013	50
	4	28.551	2.101	16.546	62
	4.5	21.221	1.476	10.440	50
	5	19.629	1.805	13.388	55
PATH-2	0	30.236	0.637	3.824	36
	1	27.377	0.676	4.585	46
	2	24.200	0.767	5.426	50
	3	19.959	0.528	4.288	66
	4	15.708	0.699	5.326	58
	5	10.301	0.473	3.728	62

Table A-7. *The average barriers for bond scission in* ***PATH-1*** *and* ***PATH-2****.*

A.6 Tabulation of the Raw Geometric Data in Chapter 4

The average end-to-end and scissile bond distances of **1**, **2**, **TS-1**, and **TS-2** are given in Table A-8. All other geometric analyses performed in Chapter 4 can be derived from these values.

		Distances in Å				
		End-to-End		Scissile Bond		
	Force in nN	Mean	Std. Dev.	Mean	Std. Dev.	N
1	3	9.7764	0.0342	1.5809	0.0023	50
	3.5	9.9637	0.0266	1.5918	0.0025	55
	4	10.0942	0.0232	1.5934	0.0023	50
	4.5	10.2883	0.0239	1.5977	0.0024	62
	5	10.4158	0.0234	1.6079	0.0025	55
TS-1	3	10.9265	0.0625	2.6332	0.0644	50
	3.5	10.9073	0.0622	2.4355	0.0654	55
	4	10.8884	0.0526	2.3239	0.0609	50
	4.5	11.0082	0.0543	2.2566	0.0625	62
	5	11.0116	0.0476	2.1550	0.0591	55
2	0	8.7612	0.1050	1.5608	0.0013	36
	1	9.5658	0.0532	1.5675	0.0014	46
	2	9.9411	0.0407	1.5748	0.0014	50
	3	10.2539	0.0263	1.5828	0.0013	66
	4	10.5073	0.0211	1.5918	0.0014	58
	5	10.6916	0.0220	1.6018	0.0014	62
TS-2	0	8.9982	0.1097	2.3756	0.0167	36
	1	9.8525	0.0584	2.3008	0.0132	46
	2	10.2824	0.0499	2.2657	0.0192	50
	3	10.5872	0.0314	2.2585	0.0108	66
	4	10.8804	0.0283	2.2614	0.0133	58
	5	11.0357	0.0287	2.2306	0.0120	62

Table A-8. *The average end-to-end and scissile bond distances in* ***1****,* ***2****,* ***TS-1****, and* ***TS-2****.*

A.7 Raw Data and Parameters Used in the Mathematical Model in Chapter 4

The parameters used in the mathematical modelling of **PATH-1** and **PATH-2** in Chapter 4 are detailed in Table A-9.

PATH-1: $E = D(1 - e^{\alpha(r-r_e)})^2 - Fr$		**PATH-2:** $E = Ar^4 - Br^2 + C - Fr$	
Parameter	Value	Parameter	Value
D	93	A	71
α	2.63	B	93
r_e	0.8	C	30.8

Table A-9. *Parameters used for mathematical modeling in Chapter 4.*

The datapoints for the change in transition state energy for the mathematical models of **PATH-1** and **PATH-2** are shown in Table A-10.

	Value for $\Delta H^{\ddagger}$	
Force	**PATH-1** (Morse)	**PATH-2** (Quartic)
0	93.000	30.454
1	90.266	29.649
2	88.061	28.852
3	86.056	28.063
4	84.182	27.282
5	82.405	26.509
6	80.707	25.745
7	79.074	24.989
8	77.497	24.241
9	75.969	23.501
10	74.486	22.770
11	73.042	22.047
12	71.634	21.333
13	70.260	20.628
14	68.917	19.931
15	67.603	19.242
16	66.315	18.563
17	65.054	17.892
18	63.816	17.230
19	62.601	16.577
20	61.408	15.933

Table A-10.*The change in the transition state energy of the mathematical models of* ***PATH-1*** *and* ***PATH-2****.*

The datapoints for the displacement of the location of the transition state are shown in Table A-11.

	Displacement of Transition State From F=1	
Force	**PATH-1** (Morse)	**PATH-2** (Quartic)
1	0.0000	0.0000
2	-0.2643	-0.0054
3	-0.4193	-0.0108
4	-0.5295	-0.0161
5	-0.6151	-0.0215
6	-0.6852	-0.0269
7	-0.7447	-0.0323
8	-0.7963	-0.0378
9	-0.8419	-0.0432
10	-0.8828	-0.0486
11	-0.9198	-0.0541
12	-0.9537	-0.0596
13	-0.9850	-0.0650
14	-1.0140	-0.0706
15	-1.0411	-0.0761
16	-1.0665	-0.0817
17	-1.0904	-0.0872
18	-1.1131	-0.0928
19	-1.1345	-0.0985
20	-1.1549	-0.1042

Table A-11. *Displacement of the position of the transition state in the mathematical models of* ***PATH-1*** *and* ***PATH-2****.*

Bibliography

(1) Becke, A. D. Perspective: Fifty Years of Density-Functional Theory in Chemical Physics. *J. Chem. Phys.* **2014**, *140* (18), 18A301. https://doi.org/10.1063/1.4869598.

(2) Dewyer, A. L.; Argüelles, A. J.; Zimmerman, P. M. Methods for Exploring Reaction Space in Molecular Systems. *Wiley Interdiscip. Rev. Comput. Mol. Sci.* **2018**, *8* (2), e1354. https://doi.org/10.1002/wcms.1354.

(3) Murdoch, J. R. What Is the Rate-Limiting Step of a Multistep Reaction? *J. Chem. Educ.* **1981**, *58* (1), 32–36. https://doi.org/10.1021/ed058p32.

(4) Kozuch, S.; Shaik, S. How to Conceptualize Catalytic Cycles? The Energetic Span Model. *Acc. Chem. Res.* **2011**, *44* (2), 101–110. https://doi.org/10.1021/ar1000956.

(5) Amatore, C.; Jutand, A. Mechanistic and Kinetic Studies of Palladium Catalytic Systems. *J. Organomet. Chem.* **1999**, *576* (1–2), 254–278. https://doi.org/10.1016/S0022-328X(98)01063-8.

(6) Kozuch, S.; Shaik, S. A Combined Kinetic-Quantum Mechanical Model for Assessment of Catalytic Cycles: Application to Cross-Coupling and Heck Reactions. *J. Am. Chem. Soc.* **2006**, *128* (10), 3355–3365. https://doi.org/10.1021/ja0559146.

(7) Hohenberg, P.; Kohn, W. Inhomogeneous Electron Gas. *Phys. Rev.* **1964**, *136* (3B), B864. https://doi.org/10.1103/PhysRev.136.B864.

(8) Kohn, W.; Sham, L. J. Self-Consistent Equations Including Exchange and Correlation Effects. *Phys. Rev.* **1965**, *140* (4A), A1133. https://doi.org/10.1103/PhysRev.140.A1133.

(9) Sousa, S. F.; Fernandes, P. A.; Ramos, M. J. General Performance of Density Functionals. *J. Phys. Chem. A* **2007**, *111* (42), 10439–10452. https://doi.org/10.1021/jp0734474.

(10) Goerigk, L.; Hansen, A.; Bauer, C.; Ehrlich, S.; Najibi, A.; Grimme, S. A Look at the Density Functional Theory Zoo with the Advanced GMTKN55 Database for General Main Group Thermochemistry, Kinetics and Noncovalent Interactions. *Phys. Chem. Chem. Phys.* **2017**, *19* (48), 32184–32215. https://doi.org/10.1039/c7cp04913g.

(11) Lin, Y. S.; Li, G. De; Mao, S. P.; Chai, J. Da. Long-Range Corrected Hybrid Density Functionals with Improved Dispersion Corrections. *J. Chem. Theory Comput.* **2013**, *9* (1), 263–272. https://doi.org/10.1021/ct300715s.

(12) Stephens, P. J.; Devlin, F. J.; Chabalowski, C. F.; Frisch, M. J. Ab Initio Calculation of Vibrational Absorption and Circular Dichroism Spectra Using Density Functional Force Fields. *J. Phys. Chem.* **1994**, *98* (45), 11623–11627.

(13) Chai, J.-D.; Head-Gordon, M. Systematic Optimization of Long-Range Corrected Hybrid Density Functionals. *J. Chem. Phys.* **2008**, *128* (8), 084106. https://doi.org/10.1063/1.2834918.

(14) Jensen, F. Atomic Orbital Basis Sets. *Wiley Interdiscip. Rev. Comput. Mol. Sci.* **2013**, *3* (3), 273–295. https://doi.org/10.1002/wcms.1123.

(15) Vanommeslaeghe, K.; Guvench, O.; D. MacKerell Jr., A. Molecular Mechanics. *Curr. Pharm. Des.* **2014**, *20* (20), 3281–3292.

(16) Senn, H. M.; Thiel, W. QM/MM Methods for Biomolecular Systems. *Angew. Chemie Int. Ed.* **2009**, *48* (7), 1198–1229. https://doi.org/10.1002/anie.200802019.

(17) MacKerell, A. D., J.; Bashford, D.; Bellott, M.; Dunbrack, R. L., J.; Evanseck, J.; Field, M. J.; Fischer, S.; Gao, J.; Guo, H.; Ha, S.; Joseph, D.; Kuchnir, L.; Kuczera, K.; Lau, F. T. K.; Mattos, C.; Michnick, S.; Ngo, T.; Nguyen, D. T.; Prodhom, B.; Reiher, W. E., I.; Roux, B.; Schlenkrich, M.; Smith, J.; Stote, R.; Straub, J.; Watanabe, M.; Wiorkiewicz-Kuczera, J.; Yin, D.; Karplus, M. All-Atom Empirical Potential for Molecular Modeling and Dynamics Studies of Proteins. *J. Phys. Chem. B* **1998**, *102*, 3586–3616.

(18) Foloppe, N.; Alexander D. MacKerell, J. All-atom Empirical Force Field for Nucleic Acids: I. Parameter Optimization Based on Small Molecule and Condensed Phase Macromolecular Target Data. *J. Comput. Chem.* **2000**, *21* (2), 86–104. https://doi.org/10.1002/(SICI)1096-987X(20000130)21:2<86::AID-JCC2>3.0.CO;2-G.

(19) Shao, Y.; Kong, J. YinYang Atom: A Simple Combined Ab Initio Quantum Mechanical Molecular Mechanical Model. *J. Phys. Chem. A* **2007**, *111* (18), 3661–3671. https://doi.org/10.1021/jp067307q.

(20) Cramer, C. J. *Essentials of Computational Chemistry : Theories and Models*, 2nd ed.; John Wiley & Sons, West Sussex, England, 2004.

(21) Halgren, T. A.; Lipscomb, W. N. The Synchronous-Transit Method for Determining Reaction Pathways and Locating Molecular Transition States. *Chem. Phys. Lett.* **1977**, *49* (2), 225–232. https://doi.org/10.1016/0009-2614(77)80574-5.

(22) Mills, G.; Jónsson, H.; Schenter, G. K. Reversible Work Transition State Theory: Application to Dissociative Adsorption of Hydrogen. *Surf. Sci.* **1995**, *324* (2–3), 305–337. https://doi.org/10.1016/0039-6028(94)00731-4.

(23) Mills, G.; Jónsson, H. Quantum and Thermal Effects in H2 Dissociative Adsorption: Evaluation of Free Energy Barriers in Multidimensional Quantum Systems. *Phys. Rev. Lett.* **1994**, *72* (7), 1124–1127. https://doi.org/10.1103/PhysRevLett.72.1124.

(24) Zimmerman, P. M. Growing String Method with Interpolation and Optimization in Internal Coordinates: Method and Examples. *J. Chem. Phys.* **2013**, *138* (18), 184102. https://doi.org/10.1063/1.4804162.

(25) Zimmerman, P. Reliable Transition State Searches Integrated with the Growing String Method. *J. Chem. Theory Comput.* **2013**, *9* (7), 3043–3050.

https://doi.org/10.1021/ct400319w.

(26) Zimmerman, P. M. Single-Ended Transition State Finding with the Growing String Method. *J. Comput. Chem.* **2015**, *36* (9), 601–611. https://doi.org/10.1002/jcc.23833.

(27) Jenkins, A. D.; Robo, M. T.; Zimmerman, P. M.; Montgomery, J. Nickel-Catalyzed Three-Component Cycloadditions of Enoates, Alkynes, and Aldehydes. *J. Org. Chem.* **2020**, *85* (5), 2956–2965. https://doi.org/10.1021/acs.joc.9b02446.

(28) Trost, B. M. [3+2] Cycloaddition Approaches to Five-Membered Rings via Trimethylenemethane and Its Equivalents [New Synthetic Methods (55)]. *Angew. Chemie Int. Ed. English* **1986**, *25* (1), 1–20. https://doi.org/10.1002/anie.198600013.

(29) Burstein, S. H. The Chemistry, Biology and Pharmacology of the Cyclopentenone Prostaglandins. *Prostaglandins Other Lipid Mediat.* **2020**, *148*, 106408. https://doi.org/10.1016/j.prostaglandins.2020.106408.

(30) Cao, H.; Chen, F.; Su, C.; Yu, L. Construction of Carbocycles from Methylenecyclopropanes. *Adv. Synth. Catal.* **2020**, *362* (3), 438–461. https://doi.org/10.1002/adsc.201900615.

(31) Pattenden, G.; Lee, T. V. Saturated Carbocyclic Ring Synthesis. In *General and Synthetic Methods: Volume 11*; Royal Society of Chemistry (RSC), 1989; pp 518–546. https://doi.org/10.1039/9781847556233-00518.

(32) Pellissier, H. Recent Developments in the Nazarov Process. *Tetrahedron* **2005**, *61* (27), 6479–6517. https://doi.org/10.1016/j.tet.2005.04.014.

(33) Hartley, R. C.; Caldwell, S. T. Novel Methods for the Synthesis of Three-, Four-, Five-, Six- and Seven-Membered, Saturated and Partially Unsaturated Carbocycles. *J. Chem. Soc. Perkin Trans. 1* **2000**, No. 4, 477–501. https://doi.org/10.1039/a804421j.

(34) Namyslo, J. C.; Kaufmann, D. E. The Application of Cyclobutane Derivatives in Organic Synthesis. *Chem. Rev.* **2003**, *103* (4), 1485–1537. https://doi.org/10.1021/cr010010y.

(35) Monfette, S.; Fogg, D. E. Equilibrium Ring-Closing Metathesis. *Chem. Rev.* **2009**, *109* (8), 3783–3816. https://doi.org/10.1021/cr800541y.

(36) Iqbal, J.; Bhatia, B.; Nayyar, N. K. Transition Metal-Promoted Free-Radical Reactions in Organic Synthesis: The Formation of Carbon-Carbon Bonds. *Chem. Rev.* **1994**, *94* (2), 519–564. https://doi.org/10.1021/cr00026a008.

(37) Gibson (née Thomas), S. E.; Middleton, R. J. The Intramolecular Heck Reaction. *Contemp. Org. Synth.* **1996**, *3* (6), 447–471. https://doi.org/10.1039/co9960300447.

(38) Reissig, H. U.; Zimmer, R. Donor - Acceptor-Substituted Cyclopropane Derivatives and Their Application in Organic Synthesis. *Chem. Rev.* **2003**, *103* (4), 1151–1196. https://doi.org/10.1021/cr010016n.

(39) Masse, C. E.; Panek, J. S. Diastereoselective Reactions of Chiral Allyl- and Allenylsilanes with Activated C=X π-Bonds. *Chem. Rev.* **1995**, *95* (5), 1293–1316. https://doi.org/10.1021/cr00037a008.

(40) Methot, J. L.; Roush, W. R. Nucleophilic Phosphine Organocatalysis. *Adv. Synth. Catal.* **2004**, *346* (910), 1035–1050. https://doi.org/10.1002/adsc.200404087.

(41) Montgomery, J. Nickel-Catalyzed Reductive Cyclizations and Couplings. *Angew. Chemie Int. Ed.* **2004**, *43* (30), 3890–3908. https://doi.org/10.1002/anie.200300634.

(42) Suzuki, K.; Urabe, H.; Sato, F. A Novel Tandem Cyclization of 2,7- or 2,8-Bis-Unsaturated Esters Mediated by (H2-Propene)TiX2 (X = Cl or O-i-Pr). A Facile Construction of Bicyclo[3.3.0]Octane, -[4.3.0]Nonane, and -[3.1.0]Hexane Skeletons. *J. Am. Chem. Soc.* **1996**, *118* (36), 8729–8730. https://doi.org/10.1021/ja961928n.

(43) Urabe, H.; Suzuki, K.; Sato, F. Intramolecular Cyclization of 2,7- or 2,8-Bis-Unsaturated Esters Mediated by (H2-Propene)Ti(O-i-Pr)2. Facile Construction of Mono- and Bicyclic Skeletons with Stereoselective Introduction of a Side Chain. A Synthesis of d-Sabinene. *J. Am. Chem. Soc.* **1997**, *119* (42), 10014–10027. https://doi.org/10.1021/ja9716160.

(44) Hata, T.; Hirone, N.; Sujaku, S.; Nakano, K.; Urabe, H. Iron-Mediated Intramolecular Metalative Cyclization of α,β- Unsaturated Esters and Amides. Versatile One-Pot Preparation of Bicyclic Ketoesters. *Org. Lett.* **2008**, *10* (21), 5031–5033. https://doi.org/10.1021/ol802170z.

(45) Hata, T.; Sujaku, S.; Hirone, N.; Nakano, K.; Imoto, J.; Imade, H.; Urabe, H. Iron-Mediated and -Catalyzed Metalative Cyclization of Electron-Withdrawing-Group-Substituted Alkynes and Alkenes with Grignard Reagents. *Chem. - A Eur. J.* **2011**, *17* (51), 14593–14602. https://doi.org/10.1002/chem.201101273.

(46) Wei, C.-H.; Mannathan, S.; Cheng, C.-H. Regio- and Enantioselective Cobalt-Catalyzed Reductive [3+2] Cycloaddition Reaction of Alkynes with Cyclic Enones: A Route to Bicyclic Tertiary Alcohols. *Angew. Chemie Int. Ed.* **2012**, *51* (42), 10592–10595. https://doi.org/10.1002/anie.201205115.

(47) Montgomery, J. Nickel-Catalyzed Cyclizations, Couplings, and Cycloadditions Involving Three Reactive Components. *Acc. Chem. Res.* **2000**, *33* (7), 467–473. https://doi.org/10.1021/ar990095d.

(48) Chowdhury, S. K.; Amarasinghe, K. K. D.; Heeg, M. J.; Montgomery, J. Diverse Reactivity Manifolds of Alkynyl Enone- and Alkynyl Enal-Derived Nickelacycles Discovery of Nickel-Promoted [3+2] and [2+1] Cycloadditions [6]. *J. Am. Chem. Soc.* **2000**, *122* (28), 6775–6776. https://doi.org/10.1021/ja0012624.

(49) Amarasinghe, K. K. D.; Chowdhury, S. K.; Heeg, M. J.; Montgomery, J. Structure of an H1 Nickel O-Enolate: Mechanistic Implications in Catalytic Enyne Cyclizations. *Organometallics* **2001**, *20* (3), 370–372. https://doi.org/10.1021/om0010013.

(50) Jenkins, A. D.; Herath, A.; Song, M.; Montgomery, J. Synthesis of Cyclopentenols and Cyclopentenones via Nickel-Catalyzed Reductive Cycloaddition. *J. Am. Chem. Soc.* **2011**, *133* (36), 14460–14466. https://doi.org/10.1021/ja206722t.

(51) Ohashi, M.; Taniguchi, T.; Ogoshi, S. Nickel-Catalyzed Formation of Cyclopentenone Derivatives via the Unique Cycloaddition of α,β-Unsaturated Phenyl Esters with Alkynes. *J. Am. Chem. Soc.* **2011**, *133* (38), 14900–14903. https://doi.org/10.1021/ja2059999.

(52) Li, W.; Herath, A.; Montgomery, J. Evolution of Efficient Strategies for Enone-Alkyne and Enal-Alkyne Reductive Couplings. *J. Am. Chem. Soc.* **2009**, *131* (46), 17024–17029. https://doi.org/10.1021/ja9083607.

(53) Herath, A.; Thompson, B. B.; Montgomery, J. Catalytic Intermolecular Reductive Coupling of Enones and Alkynes. *J. Am. Chem. Soc.* **2007**, *129* (28), 8712–8713. https://doi.org/10.1021/ja073300q.

(54) Jackson, E. P.; Malik, H. A.; Sormunen, G. J.; Baxter, R. D.; Liu, P.; Wang, H.; Shareef, A. R.; Montgomery, J. Mechanistic Basis for Regioselection and Regiodivergence in Nickel-Catalyzed Reductive Couplings. *Acc. Chem. Res.* **2015**, *48* (6), 1736–1745. https://doi.org/10.1021/acs.accounts.5b00096.

(55) Jenkins, A. D. Optimization and Development of Nickel-Catalyzed [3+2]-Reductive and Alkylative Cycloadditions, Univeristy of Michigan: Ann Arbor, MI, 2013.

(56) Nett, A. J.; Canellas, S.; Higuchi, Y.; Robo, M. T.; Kochkodan, J. M.; Haynes, M. T.; Kampf, J. W.; Montgomery, J. Stable, Well-Defined Nickel(0) Catalysts for Catalytic C-C and C-N Bond Formation. *ACS Catal.* **2018**, *8* (7), 6606–6611. https://doi.org/10.1021/acscatal.8b02187.

(57) Tasker, S. Z.; Standley, E. A.; Jamison, T. F. Recent Advances in Homogeneous Nickel Catalysis. *Nature* **2014**, *509* (7500), 299–309. https://doi.org/10.1038/nature13274.

(58) Prakasham, A. P.; Ghosh, P. Nickel N-Heterocyclic Carbene Complexes and Their Utility in Homogeneous Catalysis. *Inorganica Chim. Acta* **2015**, *431*, 61–100. https://doi.org/10.1016/j.ica.2014.11.005.

(59) Arévalo, A.; García, J. J. Bond Activation with Low-Valent Nickel in Homogeneous Systems. *Eur. J. Inorg. Chem.* **2010**, *2010* (26), 4063–4074. https://doi.org/10.1002/ejic.201000621.

(60) Iwasaki, T.; Kambe, N. Ni-Catalyzed C-C Couplings Using Alkyl Electrophiles. *Top. Curr. Chem.* **2016**, *374*, 66. https://doi.org/10.1007/s41061-016-0067-6.

(61) Mesganaw, T.; Garg, N. K. Ni- and Fe-Catalyzed Cross-Coupling Reactions of Phenol Derivatives. *Organic Process Research and Development*. American Chemical Society January 18, 2013, pp 29–39. https://doi.org/10.1021/op300236f.

(62) Tollefson, E. J.; Hanna, L. E.; Jarvo, E. R. Stereospecific Nickel-Catalyzed Cross-Coupling Reactions of Benzylic Ethers and Esters. **2015**. https://doi.org/10.1021/acs.accounts.5b00223.

(63) Jana, R.; Pathak, T. P.; Sigman, M. S. Advances in Transition Metal (Pd,Ni,Fe)-Catalyzed Cross-Coupling Reactions Using Alkyl-Organometallics as Reaction Partners. *Chem. Rev.* **2011**, *111* (3), 1417–1492. https://doi.org/10.1021/cr100327p.

(64) Lavoie, C. M.; Stradiotto, M. Bisphosphines: A Prominent Ancillary Ligand Class for Application in Nickel-Catalyzed C-N Cross-Coupling. *ACS Catalysis*. American Chemical Society August 3, 2018, pp 7228–7250. https://doi.org/10.1021/acscatal.8b01879.

(65) Ritleng, V.; Henrion, M.; Chetcuti, M. J. Nickel N-Heterocyclic Carbene-Catalyzed C-

Heteroatom Bond Formation, Reduction, and Oxidation: Reactions and Mechanistic Aspects. *ACS Catal.* **2016**, *6* (2), 890–906. https://doi.org/10.1021/acscatal.5b02021.

(66) Tobisu, M.; Chatani, N. Cross-Couplings Using Aryl Ethers via C-O Bond Activation Enabled by Nickel Catalysts. *Acc. Chem. Res.* **2015**, *48* (6), 1717–1726. https://doi.org/10.1021/acs.accounts.5b00051.

(67) Gooßen, L. J.; Gooßen, K.; Stanciu, C. C(Aryl)□O Activation of Aryl Carboxylates in Nickel-Catalyzed Biaryl Syntheses. *Angew. Chemie Int. Ed.* **2009**, *48* (20), 3569–3571. https://doi.org/10.1002/anie.200900329.

(68) Tollefson, E. J.; Hanna, L. E.; Jarvo, E. R. Stereospecific Nickel-Catalyzed Cross-Coupling Reactions of Benzylic Ethers and Esters. *Acc. Chem. Res.* **2015**, *48* (8), 2344–2353. https://doi.org/10.1021/acs.accounts.5b00223.

(69) Harry, N. A.; Saranya, S.; Ujwaldev, S. M.; Anilkumar, G. Recent Advances and Prospects in Nickel-Catalyzed C-H Activation. *Catal. Sci. Technol.* **2019**, *9* (8), 1726–1743. https://doi.org/10.1039/c9cy00009g.

(70) Pototschnig, G.; Maulide, N.; Schnürch, M. Direct Functionalization of C−H Bonds by Iron, Nickel, and Cobalt Catalysis. *Chem. - A Eur. J.* **2017**, *23* (39), 9206–9232. https://doi.org/10.1002/chem.201605657.

(71) Yamaguchi, J.; Muto, K.; Itami, K. Nickel-Catalyzed Aromatic C–H Functionalization. *Top. Curr. Chem.* **2016**, *374*, 4. https://doi.org/10.1007/s41061-016-0053-z.

(72) Guo, L.; Rueping, M. Decarbonylative Cross-Couplings: Nickel Catalyzed Functional Group Interconversion Strategies for the Construction of Complex Organic Molecules. *Acc. Chem. Res.* **2018**, *51* (5), 1185–1195. https://doi.org/10.1021/acs.accounts.8b00023.

(73) Standley, E. A.; Tasker, S. Z.; Jensen, K. L.; Jamison, T. F. Nickel Catalysis: Synergy between Method Development and Total Synthesis. *Acc. Chem. Res.* **2015**, *48* (5), 1503–1514. https://doi.org/10.1021/acs.accounts.5b00064.

(74) Xu, S.; Kim, E. H.; Wei, A.; Negishi, E. Pd- and Ni-Catalyzed Cross-Coupling Reactions in the Synthesis of Organic Electronic Materials. *Sci. Technol. Adv. Mater.* **2014**, *15* (4), 44201. https://doi.org/10.1088/1468-6996/15/4/044201.

(75) Johansson Seechurn, C. C. C.; Kitching, M. O.; Colacot, T. J.; Snieckus, V. Palladium-Catalyzed Cross-Coupling: A Historical Contextual Perspective to the 2010 Nobel Prize. *Angew. Chemie Int. Ed.* **2012**, *51* (21), 5062–5085. https://doi.org/10.1002/anie.201107017.

(76) *CRC Handbook of Chemistry and Physics, 100th Edition (Internet Version 2019)*, 100th Edit.; Rumble, J. R., Ed.; CRC Press/Taylor & Francis: Boca Raton, FL, 2019.

(77) Hazari, N.; Melvin, P. R.; Beromi, M. M. Well-Defined Nickel and Palladium Precatalysts for Cross-Coupling. *Nat. Rev. Chem.* **2017**, *1* (3), 0025. https://doi.org/10.1038/s41570-017-0025.

(78) Todd, D. P.; Thompson, B. B.; Nett, A. J.; Montgomery, J. Deoxygenative C-C Bond-Forming Processes via a Net Four-Electron Reductive Coupling. *J. Am. Chem. Soc.* **2015**,

137 (40), 12788–12791. https://doi.org/10.1021/jacs.5b08448.

(79) Macklin, T. K.; Snieckus, V. Directed Ortho Metalation Methodology. The N,N-Dialkyl Aryl O-Sulfamate as a New Directed Metalation Group and Cross-Coupling Partner for Grignard Reagents. *Org. Lett.* **2005**, *7* (13), 2519–2522. https://doi.org/10.1021/ol050393c.

(80) Martin, A. R.; Nelson, D. J.; Meiries, S.; Slawin, A. M. Z.; Nolan, S. P. Efficient C-N and C-S Bond Formation Using the Highly Active [Ni(Allyl)Cl(IPr* ^{OMe})] Precatalyst. *European J. Org. Chem.* **2014**, *2014* (15), 3127–3131. https://doi.org/10.1002/ejoc.201402022.

(81) Wu, J.; Faller, J. W.; Hazari, N.; Schmeier, T. J. Stoichiometric and Catalytic Reactions of Thermally Stable Nickel(0) NHC Complexes. *Organometallics* **2012**, *31* (3), 806–809. https://doi.org/10.1021/om300045t.

(82) Iglesias, M. J.; Blandez, J. F.; Fructos, M. R.; Prieto, A.; Álvarez, E.; Belderrain, T. R.; Nicasio, M. C. Synthesis, Structural Characterization, and Catalytic Activity of IPrNi(Styrene) 2 in the Amination of Aryl Tosylates. *Organometallics* **2012**, *31* (17), 6312–6316. https://doi.org/10.1021/om300566m.

(83) Clement, N. D.; Cavell, K. J.; Ooi, L. L. Zerovalent N-Heterocyclic Carbene Complexes of Palladium and Nickel Dimethyl Fumarate: Synthesis, Structure, and Dynamic Behavior. *Organometallics* **2006**, *25* (17), 4155–4165. https://doi.org/10.1021/om0602759.

(84) Ho, C.-Y.; Chan, C.-W.; He, L. Catalytic Asymmetric Hydroalkenylation of Vinylarenes: Electronic Effects of Substrates and Chiral N-Heterocyclic Carbene Ligands. *Angew. Chemie Int. Ed.* **2015**, *54* (15), 4512–4516. https://doi.org/10.1002/anie.201411882.

(85) Kuchenbeiser, G.; Donnadieu, B.; Bertrand, G. Stable Bis(Diisopropylamino)Cyclopropenylidene (BAC) as Ligand for Transition Metal Complexes. *J. Organomet. Chem.* **2008**, *693* (5), 899–904. https://doi.org/10.1016/j.jorganchem.2007.11.056.

(86) Ribas-Arino, J.; Marx, D. Covalent Mechanochemistry: Theoretical Concepts and Computational Tools with Applications to Molecular Nanomechanics. *Chem. Rev.* **2012**, *114*, 5558–5564. https://doi.org/10.1021/cr200399q.

(87) Blanksby, S. J.; Ellison, G. B. Bond Dissociation Energies of Organic Molecules. *Acc. Chem. Res.* **2003**, *36* (4), 255–263. https://doi.org/10.1021/ar020230d.

(88) Basedow, A. M.; Ebert, K. H. Ultrasonic Degradation of Polymers in Solution. In *Physical Chemistry*; Springer Berlin Heidelberg: Berlin, Heidelberg, 1977; pp 83–148.

(89) Zhurkov, S. N.; Korsukov, V. E. Atomic Mechanism of Fracture of Solid Polymers. *J. Polym. Sci. Polym. Phys. Ed.* **1974**, *12* (2), 385–398. https://doi.org/10.1002/pol.1974.180120211.

(90) Mar, B. D.; Qi, H. W.; Liu, F.; Kulik, H. J. Ab Initio Screening Approach for the Discovery of Lignin Polymer Breaking Pathways. *J. Phys. Chem. A* **2015**, *119* (24), 6551–6562. https://doi.org/10.1021/acs.jpca.5b03503.

(91) Caruso, M. M.; Davis, D. A.; Shen, Q.; Odom, S. A.; Sottos, N. R.; White, S. R.; Moore, J. S. Mechanically-Induced Chemical Changes in Polymeric Materials. *Chem. Rev.* **2009**, *109* (11), 5733–5798. https://doi.org/10.1021/cr9001353.

(92) Beyer, M. K. The Mechanical Strength of a Covalent Bond Calculated by Density Functional Theory. *J. Chem. Phys.* **2000**, *112* (17), 7307–7312. https://doi.org/10.1063/1.481330.

(93) Beyer, M. K. Coupling of Mechanical and Chemical Energy: Proton Affinity as a Function of External Force. *Angew. Chemie Int. Ed.* **2003**, *42* (40), 4913–4915. https://doi.org/10.1002/anie.200351748.

(94) Aktah, D.; Frank, I. Breaking Bonds by Mechanical Stress: When Do Electrons Decide for the Other Side? *J. Am. Chem. Soc.* **2002**, *124* (13), 3402–3406. https://doi.org/10.1021/ja004010b.

(95) Diesendruck, C. E.; Peterson, G. I.; Kulik, H. J.; Kaitz, J. A.; Mar, B. D.; May, P. A.; White, S. R.; Martínez, T. J.; Boydston, A. J.; Moore, J. S. Mechanically Triggered Heterolytic Unzipping of a Low-Ceiling-Temperature Polymer. *Nat. Chem.* **2014**, *6* (7), 623–628. https://doi.org/10.1038/nchem.1938.

(96) Roessler, A. G.; Zimmerman, P. M. Examining the Ways To Bend and Break Reaction Pathways Using Mechanochemistry. *J. Phys. Chem. C* **2018**, *122*, 31. https://doi.org/10.1021/acs.jpcc.8b00467.

(97) Ellen Macarthur Foundation. The New Plastics Economy. Thinking the Future of Plastics & Catalysing Action, 2017.

(98) U.S. Environmental Protection Agency, Office of Land and Emergency Management. *Advancing Sustainable Materials Management: 2015 Fact Sheet Assessing Trends in Material Generation, Recycling, Composting, Combustion with Energy Recovery and Landfilling in the United States*; 2018.

(99) Rahimi, A.; García, J. M. Chemical Recycling of Waste Plastics for New Materials Production. *Nat. Rev. Chem.* **2017**, *1* (6), 0046. https://doi.org/10.1038/s41570-017-0046.

(100) Flosdorf, E. W.; Chambers, L. A. The Chemical Action of Audible Sound. *J. Am. Chem. Soc.* **1933**, *55* (7), 3051–3052. https://doi.org/10.1021/ja01334a509.

(101) Gogate, P. R.; Prajapat, A. L. Depolymerization Using Sonochemical Reactors: A Critical Review. *Ultrason. Sonochem.* **2015**, *27*, 480–494. https://doi.org/10.1016/j.ultsonch.2015.06.019.

(102) Kulik, H. J. MODELING MECHANOCHEMISTRY FROM FIRST PRINCIPLES. In *Reviews in Computational Chemistry, First Edition.*; Parrill, A. L., Lipkowitz, K. B., Eds.; John Wiley & Sons, Inc.: Hoboken, New Jersey, 2018; pp 265–311. https://doi.org/10.1002/9781119518068.ch6.

(103) Henglein, A. Sonochemistry: Historical Developments and Modern Aspects. *Ultrasonics* **1987**, *25* (1), 6–16. https://doi.org/10.1016/0041-624X(87)90003-5.

(104) Review, T.; Jérôme, F.; Chatel, G.; De Oliveira Vigier, K. Depolymerization of Cellulose

to Processable Glucans by Non-Thermal Technologies. *Green Chem* **2016**, *18*, 3903. https://doi.org/10.1039/c6gc00814c.

(105) Holkar, C. R.; Jadhav, A. J.; Pinjari, D. V.; Pandit, A. B. Cavitationally Driven Transformations: A Technique of Process Intensification. *Ind. Eng. Chem. Res.* **2019**, *58* (15), 5797–5819. https://doi.org/10.1021/acs.iecr.8b04524.

(106) Koda, S.; Taguchi, K.; Futamura, K. Effects of Frequency and a Radical Scavenger on Ultrasonic Degradation of Water-Soluble Polymers. *Ultrason. Sonochem.* **2011**, *18* (1), 276–281. https://doi.org/10.1016/J.ULTSONCH.2010.06.007.

(107) Petit, A. C.; Noiret, N.; Guezennec, J.; Gondrexon, N.; Colliec-Jouault, S. Ultrasonic Depolymerization of an Exopolysaccharide Produced by a Bacterium Isolated from a Deep-Sea Hydrothermal Vent Polychaete Annelid. *Ultrason. Sonochem.* **2007**, *14* (2), 107–112. https://doi.org/10.1016/j.ultsonch.2006.03.010.

(108) Zhi, Z.; Chen, J.; Li, S.; Wang, W.; Huang, R.; Liu, D.; Ding, T.; Linhardt, R. J.; Chen, S.; Ye, X. Fast Preparation of RG-I Enriched Ultra-Low Molecular Weight Pectin by an Ultrasound Accelerated Fenton Process. *Sci. Rep.* **2017**, *7* (1), 541. https://doi.org/10.1038/s41598-017-00572-3.

(109) Li, J.; Li, S.; Zheng, Y.; Zhang, H.; Chen, J.; Yan, L.; Ding, T.; Linhardt, R. J.; Orfila, C.; Liu, D.; Ye, X.; Chen, S. Fast Preparation of Rhamnogalacturonan I Enriched Low Molecular Weight Pectic Polysaccharide by Ultrasonically Accelerated Metal-Free Fenton Reaction. *Food Hydrocoll.* **2018**, *95*, 551–561. https://doi.org/10.1016/j.foodhyd.2018.05.025.

(110) Zhi, Z.; Li, J.; Chen, J.; Li, S.; Cheng, H.; Liu, D.; Ye, X.; Linhardt, R. J.; Chen, S. Preparation of Low Molecular Weight Heparin Using an Ultrasound-Assisted Fenton-System. *Ultrason. Sonochem.* **2019**, *52*, 184–192. https://doi.org/10.1016/J.ULTSONCH.2018.11.016.

(111) Li, J.; Li, S.; Wu, L.; Yang, H.; Wei, C.; Ding, T.; Linhardt, R. J.; Zheng, X.; Ye, X.; Chen, S. Ultrasound-Assisted Fast Preparation of Low Molecular Weight Fucosylated Chondroitin Sulfate with Antitumor Activity. *Carbohydr. Polym.* **2019**, *209*, 82–91. https://doi.org/10.1016/J.CARBPOL.2018.12.061.

(112) Prajapat, A. L.; Gogate, P. R. Intensification of Depolymerization of Aqueous Guar Gum Using Hydrodynamic Cavitation. *Chem. Eng. Process. Process Intensif.* **2015**, *93*, 1–9. https://doi.org/10.1016/J.CEP.2015.04.002.

(113) Yue, W.; Yao, P.; Wei, Y.; Mo, H. Synergetic Effect of Ozone and Ultrasonic Radiation on Degradation of Chitosan. *Polym. Degrad. Stab.* **2008**, *93* (10), 1814–1821. https://doi.org/10.1016/J.POLYMDEGRADSTAB.2008.07.010.

(114) Prajapat, A. L.; Gogate, P. R. Intensification of Depolymerization of Polyacrylic Acid Solution Using Different Approaches Based on Ultrasound and Solar Irradiation with Intensification Studies. *Ultrason. Sonochem.* **2016**, *32*, 290–299. https://doi.org/10.1016/J.ULTSONCH.2016.03.022.

(115) Weissler, A. Depolymerization by Ultrasonic Irradiation: The Role of Cavitation. *J. Appl.*

Phys. **1950**, *21* (2), 171–173. https://doi.org/10.1063/1.1699618.

(116) Van der hoff, B. M. E.; Gall, C. E. A Method for Following Changes in Molecular Weight Distributions of Polymers on Degradation: Development and Comparison with Ultrasonic Degradation Experiments. *J. Macromol. Sci. Part A - Chem.* **1977**, *11* (9), 1739–1758. https://doi.org/10.1080/00222337708063088.

(117) Henglein, V. A. Die Reaktion Des α, α-Diphenyl-β-Pikryl-Hydrazyls Mit Langkettigen Freien Radikalen, Die Beim Ultraschallabbau von Polymethacrylsäuremethylester Gebildet Werden. *Die Makromol. Chemie* **1955**, *15* (1), 188–210. https://doi.org/10.1002/macp.1955.020150115.

(118) Tabata, M.; Miyazawa, T.; Kobayashi, O.; Sohma, J. Direct Evidence of Main-Chain Scissions Induced by Ultrasonic Irradiation of Benzene Solutions of Polymers. *Chem. Phys. Lett.* **1980**, *73* (1), 178–180. https://doi.org/10.1016/0009-2614(80)85230-4.

(119) Okkuama, M.; Hirose, T. Mechanics of Ultrasonic Degradation of Linear High Polymer and Ultrasonic Cavitation. *J. Appl. Polym. Sci.* **1963**, *7* (2), 591–602. https://doi.org/10.1002/app.1963.070070216.

(120) Schaefer, M.; Icli, B.; Weder, C.; Lattuada, M.; M Kilbinger, A. F.; Simon, Y. C. The Role of Mass and Length in the Sonochemistry of Polymers. **2016**. https://doi.org/10.1021/acs.macromol.5b02362.

(121) Okitsu, K.; Cavalieri, F. Chemical and Physical Effects of Acoustic Bubbles. In *Sonochemical Production of Nanomaterials*; Springer International Publishing: Cham, 2018; pp 1–17. https://doi.org/10.1007/978-3-319-96734-9_1.

(122) Riesz, P.; Kondo, T.; Krishna, C. M. Sonochemistry of Volatile and Non-Volatile Solutes in Aqueous Solutions: E.p.r. and Spin Trapping Studies. *Ultrasonics* **1990**, *28* (5), 295–303. https://doi.org/10.1016/0041-624X(90)90035-M.

(123) Nam, S. N.; Han, S. K.; Kang, J. W.; Choi, H. Kinetics and Mechanisms of the Sonolytic Destruction of Non-Volatile Organic Compounds: Investigation of the Sonochemical Reaction Zone Using Several OH · Monitoring Techniques. *Ultrason. Sonochem.* **2003**, *10* (3), 139–147. https://doi.org/10.1016/S1350-4177(03)00085-3.

(124) Makino, K.; Mossoba, M. M.; Riesz, P. Chemical Effects of Ultrasound on Aqueous Solutions. Formation of Hydroxyl Radicals and Hydrogen Atoms. *J. Phys. Chem.* **1983**, *87* (8), 1369–1377. https://doi.org/10.1021/j100231a020.

(125) Koda, S.; Kimura, T.; Kondo, T.; Mitome, H. A Standard Method to Calibrate Sonochemical Efficiency of an Individual Reaction System. *Ultrason. Sonochem.* **2003**, *10* (3), 149–156. https://doi.org/10.1016/S1350-4177(03)00084-1.

(126) Kruus, P.; Lawrie, J. A. G.; O'Neill, M. L. Polymerization and Depolymerization by Ultrasound. *Ultrasonics* **1988**, *26* (6), 352–355. https://doi.org/10.1016/0041-624X(88)90035-2.

(127) Encina, M. V.; Lissi, E.; Sarasúa, M.; Gargallo, L.; Radic, D. Ultrasonic Degradation of Polyvinylpyrrolidone: Effect of Peroxide Linkages. *J. Polym. Sci. Polym. Lett. Ed.* **1980**, *18* (12), 757–760. https://doi.org/10.1002/pol.1980.130181201.

(128) Berkowski, K. L.; Potisek, S. L.; Hickenboth, C. R.; Moore, J. S. Ultrasound-Induced Site-Specific Cleavage of Azo-Functionalized Poly(Ethylene Glycol). *Macromolecules* **2005**, *38* (22), 8975–8978. https://doi.org/10.1021/ma051394n.

(129) Busfield, W. K. Heats and Entropies of Polymerization, Ceiling Temperatures, Equilibrium Monomer Concentrations, and Polymerizability of Heterocyclic Compounds. In *Polymer Handbook*; Branrup, J., Immergut, E. H., Eds.; John Wiley & Sons, Inc.: New York, New York, 1989; p II/295-II/334.

(130) O'Boyle, N. M.; Vandermeersch, T.; Flynn, C. J.; Maguire, A. R.; Hutchison, G. R. Confab - Systematic Generation of Diverse Low-Energy Conformers. *J. Cheminform.* **2011**, *3* (1), 8. https://doi.org/10.1186/1758-2946-3-8.

(131) O'Boyle, N. M.; Banck, M.; James, C. A.; Morley, C.; Vandermeersch, T.; Hutchison, G. R. Open Babel: An Open Chemical Toolbox. *J. Cheminform.* **2011**, *3* (10), 33. https://doi.org/10.1186/1758-2946-3-33.

(132) Sawada, H. Chapter 2. Heat of Polymerization. *J. Macromol. Sci. Part C* **1969**, *3* (2), 339–356. https://doi.org/10.1080/15583726908545927.

(133) Ribas-Arino, J.; Shiga, M.; Marx, D. Understanding Covalent Mechanochemistry. *Angew. Chemie Int. Ed.* **2009**, *48* (23), 4190–4193. https://doi.org/10.1002/anie.200900673.

(134) Besley, N. A.; Metcalf, K. A. Computation of the Amide i Band of Polypeptides and Proteins Using a Partial Hessian Approach. *J. Chem. Phys.* **2007**, *126* (3), 035101. https://doi.org/10.1063/1.2426344.

(135) Nguyen, T. Q.; Liang, Q. Z.; Kausch, H. H. Kinetics of Ultrasonic and Transient Elongational Flow Degradation: A Comparative Study. *Polymer (Guildf).* **1997**, *38*, 3783–3793. https://doi.org/10.1016/S0032-3861(96)00950-0.

(136) Moc, J.; Simmie, J. M. Hydrogen Abstraction from N-Butanol by the Hydroxyl Radical: High Level Ab Initio Study of the Relative Significance of Various Abstraction Channels and the Role of Weakly Bound Intermediates. *J. Phys. Chem. A* **2010**, *114* (17), 5558–5564. https://doi.org/10.1021/jp1009065.

(137) Authier, O.; Ouhabaz, H.; Bedogni, S. Modeling of Sonochemistry in Water in the Presence of Dissolved Carbon Dioxide. *Ultrason. Sonochem.* **2018**, *45*, 17–28. https://doi.org/10.1016/j.ultsonch.2018.02.044.

(138) Suslick, K. S.; Hammerton, D. A.; Cline, R. E. The Sonochemical Hot Spot. *J. Am. Chem. Soc.* **1986**, *108* (18), 5641–5642. https://doi.org/10.1021/ja00278a055.

(139) Buchholz, F. L. Preparation Methods of Superabsorbent Polyacrylates. In *Superabsorbent Polymers*; Buchholz, F. L., Peppas, N. A., Eds.; 1994; pp 27–38. https://doi.org/10.1021/bk-1994-0573.ch002.

(140) Kinoshita, K.; Takano, Y.; Ohkouchi, N.; Deguchi, S. Free-Radical Polymerization of Acrylic Acid under Extreme Reaction Conditions Mimicking Deep-Sea Hydrothermal Vents. *ACS Omega* **2017**, *2*, 2765–2769. https://doi.org/10.1021/acsomega.7b00293.

(141) Bell, G. I. Models for the Specific Adhesion of Cells to Cells. *Science (80-.).* **1978**, *200*

(4342), 618–627. https://doi.org/10.1126/science.347575.

(142) Konda, S. S. M.; Brantley, J. N.; Bielawski, C. W.; Makarov, D. E. Chemical Reactions Modulated by Mechanical Stress: Extended Bell Theory. *J. Chem. Phys.* **2011**, *135* (16), 164103. https://doi.org/10.1063/1.3656367.

(143) Hopffgarten, M. von; Frenking, G. Energy Decomposition Analysis. *WIREs Comput. Mol. Sci.* **2012**, *2* (1), 43–62. https://doi.org/10.1002/wcms.71.

(144) Knizia, G. Intrinsic Atomic Orbitals: An Unbiased Bridge between Quantum Theory and Chemical Concepts. *J. Chem. Theory Comput.* **2013**, *9* (11), 4834–4843. https://doi.org/10.1021/ct400687b.

(145) Ess, D. H.; Houk, K. N. Distortion/Interaction Energy Control of 1,3-Dipolar Cycloaddition Reactivity. *J. Am. Chem. Soc.* **2007**, *129* (35), 10646–10647. https://doi.org/10.1021/ja0734086.

(146) Chen, S.; Huang, X.; Meggers, E.; Houk, K. N. Origins of Enantioselectivity in Asymmetric Radical Additions to Octahedral Chiral-at-Rhodium Enolates: A Computational Study. *J. Am. Chem. Soc.* **2017**, *139* (49), 17902–17907. https://doi.org/10.1021/jacs.7b08650.

(147) Sigman, M. S.; Harper, K. C.; Bess, E. N.; Milo, A. The Development of Multidimensional Analysis Tools for Asymmetric Catalysis and Beyond. *Acc. Chem. Res.* **2016**, *49* (6), 1292–1301. https://doi.org/10.1021/acs.accounts.6b00194.

(148) Gettier, E. L. Is Justified True Belief Knowledge? *Analysis* **1963**, *23* (6), 121–123. https://doi.org/10.1093/analys/23.6.121.

(149) Shao, Y.; Gan, Z.; Epifanovsky, E.; Gilbert, A. T. B.; Wormit, M.; Kussmann, J.; Lange, A. W.; Behn, A.; Deng, J.; Feng, X.; Ghosh, D.; Goldey, M.; Horn, P. R.; Jacobson, L. D.; Kaliman, I.; Khaliullin, R. Z.; Kuś, T.; Landau, A.; Liu, J.; Proynov, E. I.; Rhee, Y. M.; Richard, R. M.; Rohrdanz, M. A.; Steele, R. P.; Sundstrom, E. J.; Woodcock, H. L.; Zimmerman, P. M.; Zuev, D.; Albrecht, B.; Alguire, E.; Austin, B.; Beran, G. J. O.; Bernard, Y. A.; Berquist, E.; Brandhorst, K.; Bravaya, K. B.; Brown, S. T.; Casanova, D.; Chang, C.-M.; Chen, Y.; Chien, S. H.; Closser, K. D.; Crittenden, D. L.; Diedenhofen, M.; DiStasio, R. A.; Do, H.; Dutoi, A. D.; Edgar, R. G.; Fatehi, S.; Fusti-Molnar, L.; Ghysels, A.; Golubeva-Zadorozhnaya, A.; Gomes, J.; Hanson-Heine, M. W. D.; Harbach, P. H. P.; Hauser, A. W.; Hohenstein, E. G.; Holden, Z. C.; Jagau, T.-C.; Ji, H.; Kaduk, B.; Khistyaev, K.; Kim, J.; Kim, J.; King, R. A.; Klunzinger, P.; Kosenkov, D.; Kowalczyk, T.; Krauter, C. M.; Lao, K. U.; Laurent, A. D.; Lawler, K. V.; Levchenko, S. V.; Lin, C. Y.; Liu, F.; Livshits, E.; Lochan, R. C.; Luenser, A.; Manohar, P.; Manzer, S. F.; Mao, S.-P.; Mardirossian, N.; Marenich, A. V.; Maurer, S. A.; Mayhall, N. J.; Neuscamman, E.; Oana, C. M.; Olivares-Amaya, R.; O'Neill, D. P.; Parkhill, J. A.; Perrine, T. M.; Peverati, R.; Prociuk, A.; Rehn, D. R.; Rosta, E.; Russ, N. J.; Sharada, S. M.; Sharma, S.; Small, D. W.; Sodt, A.; Stein, T.; Stück, D.; Su, Y.-C.; Thom, A. J. W.; Tsuchimochi, T.; Vanovschi, V.; Vogt, L.; Vydrov, O.; Wang, T.; Watson, M. A.; Wenzel, J.; White, A.; Williams, C. F.; Yang, J.; Yeganeh, S.; Yost, S. R.; You, Z.-Q.; Zhang, I. Y.; Zhang, X.; Zhao, Y.; Brooks, B. R.; Chan, G. K. L.; Chipman, D. M.; Cramer, C. J.; Goddard, W. A.; Gordon, M. S.; Hehre, W. J.; Klamt, A.; Schaefer, H. F.; Schmidt, M. W.; Sherrill, C. D.;

Truhlar, D. G.; Warshel, A.; Xu, X.; Aspuru-Guzik, A.; Baer, R.; Bell, A. T.; Besley, N. A.; Chai, J.-D.; Dreuw, A.; Dunietz, B. D.; Furlani, T. R.; Gwaltney, S. R.; Hsu, C.-P.; Jung, Y.; Kong, J.; Lambrecht, D. S.; Liang, W.; Ochsenfeld, C.; Rassolov, V. A.; Slipchenko, L. V.; Subotnik, J. E.; Van Voorhis, T.; Herbert, J. M.; Krylov, A. I.; Gill, P. M. W.; Head-Gordon, M. Advances in Molecular Quantum Chemistry Contained in the Q-Chem 4 Program Package. *Mol. Phys.* **2015**, *113* (2), 184–215. https://doi.org/10.1080/00268976.2014.952696.

(150) Neese, F. Software Update: The ORCA Program System, Version 4.0. *WIREs Comput. Mol. Sci.* **2018**, *8* (1). https://doi.org/10.1002/wcms.1327.

(151) Hariharan, P. C.; Pople, J. A. The Influence of Polarization Functions on Molecular Orbital Hydrogenation Energies. *Theor. Chim. Acta* **1973**, *28* (3), 213–222. https://doi.org/10.1007/BF00533485.

(152) Rassolov, V. A.; Pople, J. A.; Ratner, M. A.; Windus, T. L. 6-31G* Basis Set for Atoms K through Zn. *J. Chem. Phys.* **1998**, *109* (4), 1223–1229. https://doi.org/10.1063/1.476673.

(153) Dunning, T. H. Gaussian Basis Sets for Use in Correlated Molecular Calculations. I. The Atoms Boron through Neon and Hydrogen. *J. Chem. Phys.* **1989**, *90* (2), 1007–1023. https://doi.org/10.1063/1.456153.

(154) Balabanov, N. B.; Peterson, K. A. Basis Set Limit Electronic Excitation Energies, Ionization Potentials, and Electron Affinities for the 3d Transition Metal Atoms: Coupled Cluster and Multireference Methods. *J. Chem. Phys.* **2006**, *125* (7), 074110. https://doi.org/10.1063/1.2335444.

(155) Marenich, A. V.; Cramer, C. J.; Truhlar, D. G. Universal Solvation Model Based on Solute Electron Density and on a Continuum Model of the Solvent Defined by the Bulk Dielectric Constant and Atomic Surface Tensions. *J. Phys. Chem. B* **2009**, *113* (18), 6378–6396. https://doi.org/10.1021/jp810292n.

(156) Wertz, D. H. Relationship between the Gas-Phase Entropies of Molecules and Their Entropies of Solvation in Water and 1-Octanol. *J. Am. Chem. Soc.* **1980**, *102* (16), 5316–5322. https://doi.org/10.1021/ja00536a033.

(157) Rackers, J. A.; Wang, Z.; Lu, C.; Laury, M. L.; Lagardère, L.; Schnieders, M. J.; Piquemal, J. P.; Ren, P.; Ponder, J. W. Tinker 8: Software Tools for Molecular Design. *J. Chem. Theory Comput.* **2018**, *14* (10), 5273–5289. https://doi.org/10.1021/acs.jctc.8b00529.

(158) Carey, F. A.; Sundberg, R. J. Polar Addition and Elimination Reactions. In *Advanced Organic Chemistry: Part A: Structure and Mechanisms*; Springer US: Boston, MA, 2007; pp 473–577. https://doi.org/10.1007/978-0-387-44899-2_5.

(159) Tian, Y.; Boulatov, R. Comparison of the Predictive Performance of the Bell–Evans, Taylor-Expansion and Statistical-Mechanics Models of Mechanochemistry. *Chem. Commun.* **2013**, *49* (39), 4187–4189. https://doi.org/10.1039/C2CC37095F.